Biophysical foundation and function of depolarizing afterpotentials in principal cells of the medial entorhinal cortex

Caroline Fischer

Graduate School of Systemic Neurosciences

LMU Munich

Dissertation at the

Graduate School of Systemic Neurosciences

Ludwig-Maximilians-Universität München

February, 2019

Manchmal hat man eine sehr lange Straße vor sich. Man denkt, die ist so schrecklich lang; das kann man niemals schaffen, denkt man. Und dann fängt man an, sich zu eilen. Und man eilt sich immer mehr. Jedes Mal, wenn man aufblickt, sieht man, dass es gar nicht weniger wird, was noch vor einem liegt.

Und man strengt sich noch mehr an, man kriegt es mit der Angst zu tun und zum Schluss ist man ganz außer Puste und kann nicht mehr. Und die Straße liegt immer noch vor einem. So darf man es nicht machen. Man darf nie an die ganze Straße auf einmal denken, verstehst du? Man muss immer nur an den nächsten Schritt denken, an den nächsten Atemzug, an den nächsten Besenstrich. Dann macht es Freude; das ist wichtig, dann macht man seine Sache gut. Und so soll es sein.

Auf einmal merkt man, dass man Schritt für Schritt die ganze Straße gemacht hat. Man hat gar nicht gemerkt wie, und man ist nicht außer Puste. Das ist wichtig.

— **Michael Ende**

Abstract

Neurons in layer II of the rodent medial entorhinal cortex (MEC) encode spatial information. One particular type, grid cells, tends to fire at specific spatial locations that form hexagonal lattices covering the explored environment. Within these firing fields grid cells frequently show short high-frequency spike sequences. Such bursts have received little attention but may contribute substantially to encoding spatial information. On the other hand, *in vitro* recordings of MEC principal cells have revealed that action potentials are followed by prominent depolarizing afterpotentials (DAP). Their biophysical foundation and function, however, are poorly understood.

The objective of this study is to understand the mechanism behind the DAP by creating a biophysical realistic model of a stellate cell and to draw a connection between DAPs and burst firing *in vivo*.

The developed single-compartment model reproduced the main electrophysiological characteristics of stellate cells in the MEC layer II, that are a DAP, sag, tonic firing in response to positive step currents and resonance. Using virtual blocking experiments, it was found that for the generation of the DAP only a Na_P, K_{DR} and leak current were necessary whereby the Na_P current also exhibited a resurgent component. This suggests that for the generation of the DAP a balance between several currents is needed. In addition, the persistent and resurgent sodium current might play an important role.

We analyzed the relevance of DAPs *in vivo* using whole-cell recordings of grid cells from Domnisoru et al. (2013). We found that around 20% of the cells exhibited a DAP. However, the percentage of cells was much lower than estimates from *in vitro* recordings. We showed that this is partly due to the quality of the recording as selecting APs from presumably good parts of the recording improved the visibility of DAPs. To investigate the relationship between DAPs and burst firing all cells were classified into bursty and non-bursty based on the spike-time autocorrelation. All cells with a DAP were bursty except the cell with the smallest DAP. Moreover, taking the mean of the spike-triggered average of the membrane potential for all bursty and non-bursty cells respectively showed a clear DAP for bursty but not for non-bursty cells.

In summary, we found that the DAP can be realized in a single-compartment model by a Na_P, K_{DR} and leak current and provided evidence for the relevance of DAPs for burst firing *in vivo*.

List of Abbreviations

AEA	Anandamide
AP	Action potential
Ca_{LVA}	Low-voltage activated calcium channel
DAP	Depolarizing afterpotential
EC	Entorhinal cortex
EPSP	Excitatory postsynaptic potential
fAHP	Fast afterhyperpolarization
HCN	Hyperpolarization-activated cation channel
HDR	High density region (definition in Sec. 4.4.2)
ISI	Interspike interval
K_A	A-type potassium channel
K_{DR}	Delayed-rectifier potassium channel
K_M	M-type potassium channel
L-BFGS-B	Limited memory BFGS (Broyden-Fletcher-Goldfarb-Shanno) algorithm for bound constrained optimization
LEC	Lateral entorhinal cortex
LTP	Long term potentiation
mAHP	Medium afterhyperpolarization
MEC	Medial entorhinal cortex
$MECII_{DAP}$	Cells of the medial entorhinal cortex layer II with a depolarizing afterpotential (definition in Sec. 4.4.1)
Na_T	Transient sodium channel
Na_P	Persistent sodium channel
Na_R	Resurgent sodium channel
PCA	Principal component analysis
PC	Principal component
PDF	Probability density function
RMSE	Root mean square error
SEM	Standard error of the mean
STA_V	Spike-triggered average of the membrane potential
TTX	Tetrodotoxin

Contents

Introduction

<div style="text-align: right">1</div>

You arrived for a trip in a new city and need to find the way to your accommodation. You take out your smartphone, open the navigation app of your choice and it shows you a map with the shortest route from your current location to your accommodation. After several days of running around in the city you will not need your smartphone anymore for finding the accommodation. Your brain will have built up a map itself. But how is this map realized and represented in the brain?

1.1 Coding of space in the brain

1.1.1 Place cells

First indications of how space is coded in the brain came from O'Keefe and Dostrovsky (1971). They found cells in the hippocampus that had an increased firing rate when the animal was at a certain position of the environment (Fig. 1.1) (for a review see E. I. Moser, Kropff, et al., 2008; Best et al., 2001). These so-called place cells were hypothesized to form a map of a given environment whereby each cell represents a specific part (O'Keefe, 1976).
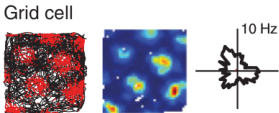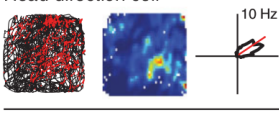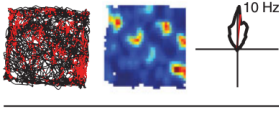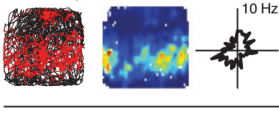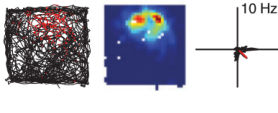
	Pre-Parasubiculum	MEC II	MEC III	MEC V-VI	Hippocampus
Grid cell	✓	✓	✓	✓	NO
Head direction cell	✓	NO	✓	✓	NO
Conjunctive cell	✓	NO	✓	✓	NO
Boundary vector cell	✓	✓	✓	✓	NO
Place cell	NO	NO	NO	NO	✓

Fig. 1.1: Examples of different types of spatially modulated cells and their occurrence. Adopted from M. Brandon et al. (2014). In the left column for each cell type is shown: i) The running trajectory (black) of the animal in a square-shaped environment with the spikes (red) superimposed. ii) The color-coded firing rate map (red: high firing rate, blue: low firing rate). iii) A polar plot of the firing rate as function of the head direction of the animal. The right columns indicate the brain areas where each cell type was found.

1.1.2 Grid cells

Already Ramon y Cajal noted in his studies of the nervous system that the entorhinal cortex (EC) is strongly connected to the hippocampus and suggested that their functions are related (Ramon y Cajal, 1902). Indeed, Fyhn et al. (2004) discovered that cells in the medial entorhinal cortex (MEC) are spatially modulated. These cells fire when the animal's position coincides with any vertex of a hexagonal lattice spanning the ground of the environment (Fig. 1.1) (Hafting et al., 2005; for a review see E. I. Moser, Kropff, et al., 2008).

Grid cells are hypothesized to play a role in mammalian path integration (Hafting et al., 2005; McNaughton et al., 2006; E. I. Moser and M.-B. Moser, 2008). This is the ability of an animal to keep track of its location relative to an initial reference point using self-motion information and to determine a direct return path. Behavioral experiments on path integration have been carried out on many species, most notably on desert ants (Fig. 1.2).

In mammals, a connection between grid cell activity and path integration was established by two studies. Parron and Save (2004) showed that finding the return path is impaired when the EC is lesioned. More specifically, Gil et al. (2018) demonstrated that removing NMDA glutamate receptors leads to disrupted grid cell activity and path integration that correlates in degree.
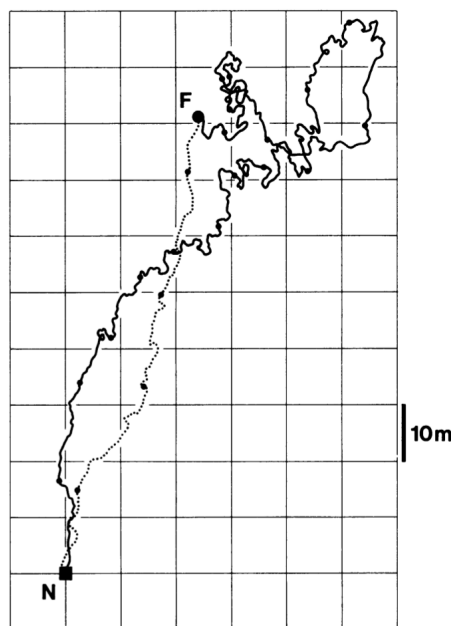
Fig. 1.2: Path integration in the desert ant. Adopted from Müller and Wehner (1988). Outbound (solid line) and inbound (stippled line) path of an individual desert ant between the nest (N) and a food location (F) with time marks (small circles) every 60 s. Note that the desert ant is able to find a direct return path from the food location to the nest.

1.1.3 Other spatially modulated cells

To complete the list, a few other spatially modulated cells have to be mentioned (Fig. 1.1). Head direction cells increase their firing rate when the animal's head points into the preferred direction of the cell (Taube et al., 1990; Taube, 1998). The borders of an environment are represented by border cells (Solstad et al., 2008; Lever et al., 2009). Another type are conjunctive cells. These cells combine a hexagonal grid firing pattern with head-direction preference (Sargolini et al., 2006). Object-vector cells, recently discovered by Hoydal et al. (2018), fire when the animal is at a specific distance and direction from an object.

In addition, there are also cells that are modulated by the animal's running speed (Kropff, Carmichael, et al., 2015) as well as neurons that encode the elapsed time (MacDonald et al., 2011; Kraus, Robinson II, et al., 2013; Kraus, M. P. Brandon, et al., 2015; Tsao, Sugar, et al., 2018).

1.2 Connectivity of the entorhinal cortex

Spatially modulated cells are found in the hippocampal formation and parahippocampal region (Fig. 1.3). The hippocampal formation comprises the dentate gyrus (DG), the areas CA3, CA2, CA1 and the subiculum (Sub). The parahippocampal region consists of the pre- and parasubiculum, the entorhinal, perirhinal and postrhinal cortex. This distinction is based on the laminar organization whereby the hippocampal formation is three-layered and the parahippocampal region six-layered (Witter et al., 2000).

The EC connects to the hippocampal formation through the perforant path. The perforant path is constituted by two pathways (see inset of Fig. 1.3). One pathway projects from layer II of the EC to the dentate gyrus and CA3 that, in turn, has forward connections to CA1 (Andersen et al., 1971; Steward and Scoville, 1976; Yeckel and Berger, 1990). The other pathway begins in layer

Fig. 1.3: Illustration of a horizontal section of the hippocampal formation (Dentate gyrus (DG), CA1, CA3 and Subiculum (Sub)) by Ramon y Cajal (1909). The inset shows major pathways between different layers of the entorhinal cortex (EC) and the hippocampal formation.

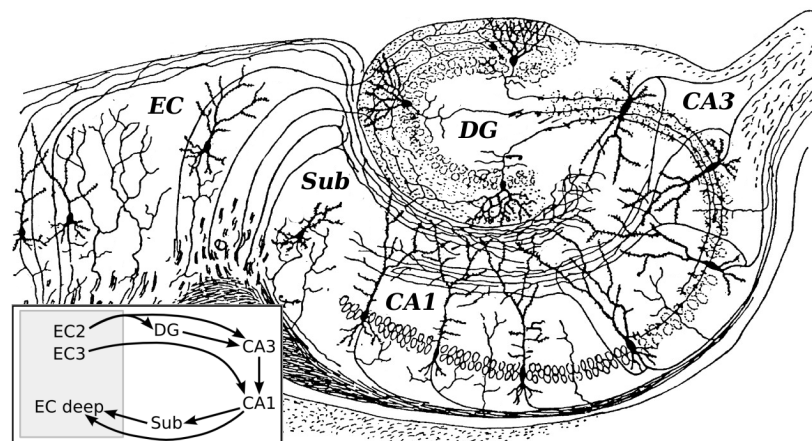III of the EC and connects directly to CA1 (Steward and Scoville, 1976; Yeckel and Berger, 1990; Brun et al., 2008). The output of CA1 is relayed back to the deep layers of the EC partially mediated by the subiculum (Tamamaki and Nojyo, 1995; Amaral et al., 1991). Naturally, many more connections exist (Witter et al., 2000; Van Strien et al., 2009).

The medial and lateral region of the EC are usually considered separately as they do have different connectivity and functionality (Canto, Wouterlood, et al., 2008; Knierim et al., 2014). A major difference in connectivity is that the MEC receives input from the postrhinal cortex and the pre- and parasubiculum whereas the lateral entorhinal cortex (LEC) receives input from the perirhinal cortex (Suzuki and Amaral, 1994; Burwell, 2000; Groen and Wyss, 1990; Canto, Wouterlood, et al., 2008).

This stands in connection with their different functional roles. In the pre- and parasubiculum spatially modulated cells were found (Fig. 1.1) that could forward spatial information to the MEC (M. Brandon et al., 2014; Boccara et al., 2010). In fact, cells in the MEC are strongly spatially modulated in contrast to cells in the LEC (Hargreaves et al., 2005). As the MEC is strongly involved in processing spatial information (Fyhn et al., 2004; Hafting et al., 2005; Sargolini et al., 2006) it is seen as part of the where pathway (Ungerleider and Haxby, 1994) or as providing the hippocampus with spatial context information (Knierim et al., 2014, Norman and Eacott, 2005).

The LEC, on the other hand, is modulated by the perirhinal region that is involved in object recognition (Murray, T. Bussey, et al., 2000; Murray and Mishkin, 1998; Murray, Baxter, et al., 1998, Norman and Eacott, 2005; Winters et al., 2006) and perceptual processing of complex stimuli (T. J. Bussey et al., 2002; Buckley et al., 2001; Eacott et al., 2001). The LEC is associated with processing object-related information (Tsao, M.-B. Moser, et al., 2013; Deshmukh and Knierim, 2011) and is thus considered part of the what pathway (Ungerleider and Haxby, 1994) or as providing the hippocampus with content information (Knierim et al., 2014).

The extrinsic connectivity of the EC includes connections to olfactory-related structures (Kosel et al., 1981; Krettek and Price, 1977). Furthermore, there is cortical connectivity with multimodal association areas as the parietal, temporal and prefrontal cortex (Swanson and Kohler, 1986; Burwell, 2000; Canto, Wouterlood, et al., 2008) and subcortical connectivity with the basal forebrain, claustrum, amygdala, basal ganglia, thalamus, hypothalamus and brainstem (Beckstead, 1978; Insausti et al., 1987; Canto, Wouterlood, et al., 2008).

1.3 Morphology, electrophysiology and immunohistochemistry of principal cells in MEC layer II

We concentrated our investigations on layer II of the MEC as it constitutes a major input source of the hippocampal formation and contains grid cells.

The MEC contains two principal cell types: Stellate cells, making up about 70% and pyramidal cells, making up about 20% of the whole cell population whereby the remainder is comprised of horizontal and small round cells (Klink and Alonso, 1997; Gatome et al., 2010). Morphologically, stellate cells can be recognized by: i) their multiple, thick primary dendrites, ii) a widely spreading dendritic tree close to the pial surface and iii) a thick axon emerging from a primary dendrite. Pyramidal cells on the other hand have: i) usually only one principal apical dendrite, ii) more confined dendritic trees and iii) a thin axon emerging from the base of the soma (Fig. 1.4) (Klink and Alonso, 1997; Canto and Witter, 2012).

Electrophysiologically the two cell types differ, too. Subthreshold behavior can be tested by inserting a long step current of small amplitude (Fig. 1.5 B, F). Stellate cells respond with a sag, i.e. shortly after current onset the membrane potential attains a peak and then settles at a lower voltage deflection (Alonso and Klink, 1993; Alessi et al., 2016; Dickson et al., 2000). In pyramidal cells only weak sags are visible (Alonso and Klink, 1993; Alessi et al., 2016). The sag was shown to be mediated by HCN channels as it can be abolished by blocking HCN channels with Cs^+ or $ZD7288$ and reduced by deletion of HCN1 channels (Dickson et al., 2000; Jones, 1994; Nolan et al., 2007).

By testing increasingly positive amplitudes of the step current, one can investigate the superthreshold behavior (Fig. 1.5 C, G). Stellate cells often show a doublet shortly after current injection followed by moderately adapting tonic firing whereas pyramidal cells can have a long latency till the first single spike
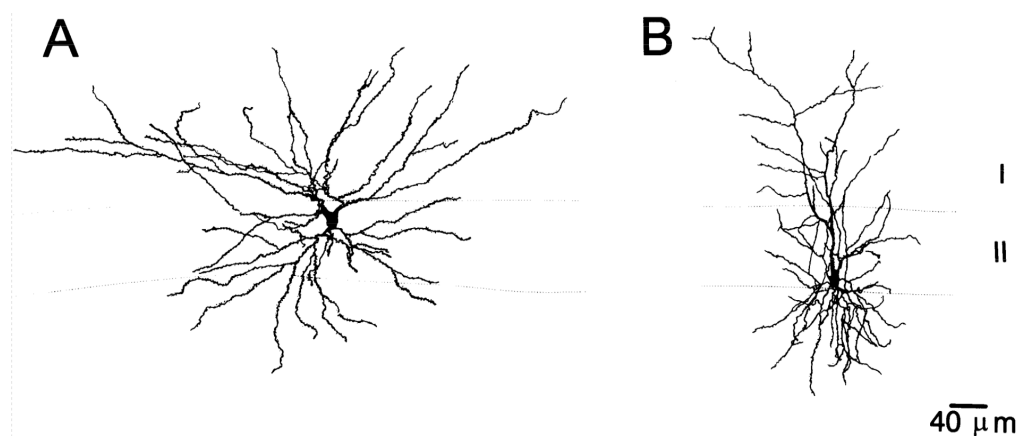
Fig. 1.4: Morphology of a stellate (A) and pyramidal (B) cell by Alonso and Klink (1993).

that is followed by adapting tonic firing (Alonso and Klink, 1993; Alessi et al., 2016).

Another defining characteristic of stellate cells is resonance. When given a ZAP current, an oscillatory input whose frequency increases over time, the membrane potential has the highest impedance for frequencies in the theta range (5-11 Hz) (Fig. 1.5 D, H) (Canto and Witter, 2012; Erchova et al., 2004; Haas and White, 2002). Pyramidal cells, on the other hand, show no or weak resonance (Canto and Witter, 2012; Erchova et al., 2004; Haas and White, 2002). Resonance in stellate cells is also dependent on HCN channels as blocking HCN or deleting HCN1 channels led to a decrease of the resonance frequency (Nolan et al., 2007; Heys et al., 2010).

Another resonance phenomenon becomes apparent when stellate cells are depolarized close to the spike threshold by constant current injection. Subthreshold oscillations in the theta range emerge that are interrupted by spike clusters with a firing frequency in the high theta range (Nolan et al., 2007; Engel et al., 2008). In contrast to resonance in response to a ZAP current these oscillations are hypothesized to be caused by stochastic ion channel gating (Dorval and White, 2005; Dudman and Nolan, 2009; Engel et al., 2008).
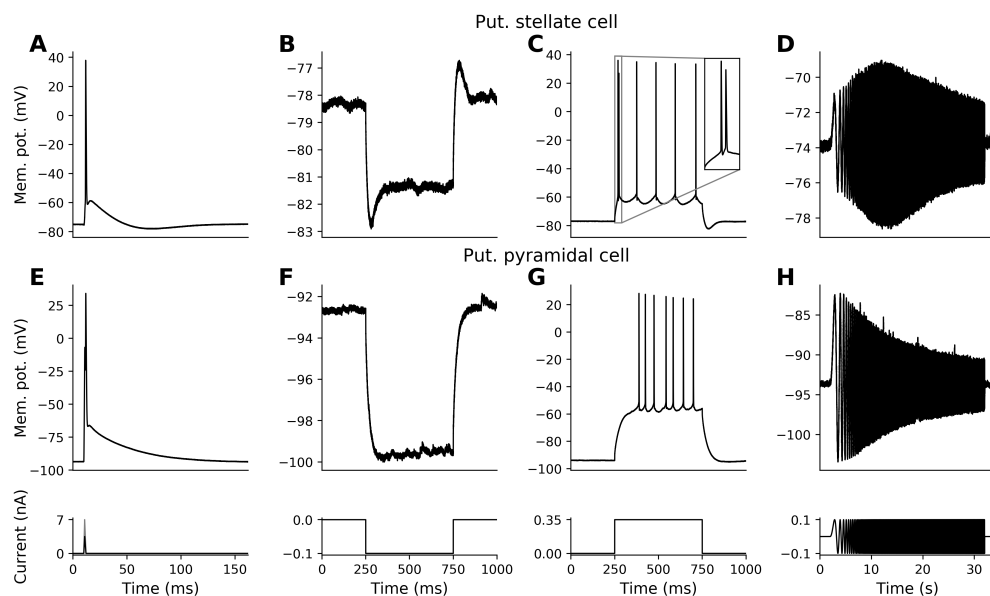
Fig. 1.5: Comparison of stellate cell (first row) and pyramidal cell (second row) electrophysiology. A, E: Stimulation with a triangular pulse elicits an AP at 3.5 nA in the putative stellate and at 7 nA in the putative pyramidal cell. The DAP is more pronounced in the putative stellate cell. B, F: The putative stellate cell shows a sag in response to a negative step current (and likewise an overshoot at the end of the stimulus) whereas the putative pyramidal cell shows no sag. C, G: A superthreshold step current elicits an initial doublet (shown in the inset) followed by regular spiking in the putative stellate cell. The putative pyramidal cell shows tonic firing after a long initial latency. D, H: The putative stellate cell exhibits resonance at a stimulation frequency of 7 Hz in response to a ZAP current in contrast to the putative pyramidal cell, which acts as a low-pass filter. The data for these figures were recorded by Kümpfbeck (2019).

The action potential (AP) of layer II MEC cells has a special shape as the spike is often followed by a depolarizing afterpotential (DAP), a depolarization in the membrane potential with a clearly visible maximum around 4 ms after the AP and an amplitude of about 14.5 mV (Fig. 1.5 A, E). The DAP is more pronounced in stellate than in pyramidal cells (Alonso and Klink, 1993; Alessi et al., 2016; Canto and Witter, 2012).

Besides these two principal cell types, there are also intermediate cell types with morphologies close to pyramidal or between stellate and pyramidal cells. These intermediate cell types have electrophysiological characteristics similar to stellate or pyramidal cells (Canto and Witter, 2012; Fuchs et al., 2016).

Another means to distinguish between stellate and pyramidal cells is immuno-histochemistry. It was proposed that cells that express reelin are stellate cells and that cells that express calbindin are pyramidal cells (Kitamura et al., 2014; Ray et al., 2014; Fuchs et al., 2016; Winterer et al., 2017).

Although these characterizations provide a nice picture of what a typical stellate and pyramidal cell is, the boundaries are not that clear. For instance, when looking at the relation between electrophysiology and morphology, it appears that, firstly, electrophysiological characteristics do not fall into two or more classes but are distributed continuously (see e.g. Fig. 2.4 D, Fig. 2.6 D) and, secondly, that only a majority but not all cells show the typical characteristics so that there is considerable overlap between cell types (Alonso and Klink, 1993; Canto and Witter, 2012). For example, 80% of all stellate cells and 41% of all pyramidal cells have a prominent sag ratio (the ratio of the maximal voltage deflection and the mean steady state membrane potential in response to a subthreshold step current) (Canto and Witter, 2012). Comparing immunohistochemistry with electrophysiology leads to inconsistencies, too. For example, a majority of calbindin$^+$, putative pyramidal, cells had a resonance frequency higher than 2 Hz and a pronounced sag - electrophysiological characteristics typical for stellate cells (Kümpfbeck, 2019). The problem of clear-cut classification of stellate and pyramidal cells is also reflected in the fact that each paper introduces its own classification method instead of using a single generally accepted method (Couey et al., 2013; Alessi et al., 2016; Fuchs et al., 2016; Winterer et al., 2017; Justus et al., 2017).

1.4 Local connectivity in the MEC layer II

The function of stellate cells depends strongly on the local connectivity. For instance, continuous attractor networks, a current model to explain grid cell firing, often require inhibitory connections (Burak and Fiete, 2009; Couey et al., 2013; Pastoll et al., 2013).

In the MEC layer II stellate cells have many connections with inhibitory in-terneurons (Couey et al., 2013; Fuchs et al., 2016). They connect to fast-spiking interneurons, however, receive few inputs from low-threshold spiking or 5-HT3A+

interneurons (Couey et al., 2013; Fuchs et al., 2016). Pyramidal cells, on the other hand, are not connected to fast-spiking and low-threshold spiking interneurons but get innervated by 5-HT3A+ interneurons (Fuchs et al., 2016).

Excitatory connections inside MEC layer II are very sparse. This includes recurrent connections of stellate and pyramidal cells and connections between stellate and pyramidal cells (Dhillon and Jones, 2000; Couey et al., 2013; Fuchs et al., 2016; Winterer et al., 2017). Furthermore, the number of excitatory connections between MEC layer II and layer III is low (Winterer et al., 2017).

In summary, local connectivity in the MEC layer II is dominated by inhibition.

1.5 The biophysical foundation and function of the DAP

In this study we focused on the phenomenon of the DAP because *in vitro* it is seen in the majority, approximately 85% of stellate cells in the MEC (Canto and Witter, 2012; Alonso and Klink, 1993) and is highly likely to have an impact on the firing behavior and hence function of the cell (Alessi et al., 2016; Kümpfbeck, 2019; Navratilova et al., 2012; Mishra et al., 2016).

Biophysical foundation

At least five mechanism are conceivable to form the biophysical foundation of the DAP (later referred to as hypothesis 1-5):

1. Hypothesis: A back-propagating AP eliciting a dendritic spike that re-depolarizes the soma (Turner et al., 2002; Izhikevich, 2007)

2. Hypothesis: A slow inward current caused by low-voltage activated calcium channels (Ca_{LVA}) or persistent sodium channels (Na_P) (Azouz et al., 1996; L. Zhang et al., 1993)

3. Hypothesis: A resurgent sodium channel (Na_R) that is open after the spike due to the inability of persistent inactivation (Castelli et al., 2007)

4. Hypothesis: The window current of a transient sodium channel (Na_T) (Magistretti and Alonso, 1999; Alessi et al., 2016)

5. Hypothesis: The interplay of several currents as shown, for instance, for the AP in the squid axon by Hodgkin and Huxley (1952)

The first mechanism is different from the rest as it involves the morphology of the cell. By means of simultaneous recordings from the soma and dendrite it was shown that the AP elicited in the soma propagates into the dendrite potentially eliciting a dendritic spike that in turn re-depolarizes the soma (Stuart and Häusser, 2001; Häusser et al., 2000). It was furthermore shown that the dendritic spike can result in a DAP in the soma (Turner et al., 2002; Izhikevich, 2007). Stellate

cells in the MEC layer II can generate dendritic spikes that depend on voltage-gated sodium and NMDA receptor channels (Schmidt-Hieber, Toleikyte, et al., 2017). But it seems unlikely that the returning dendritic spikes result in a DAP as stellate cells have multiple primary dendrites so that timing differences between the different back-propagating APs could easily lead to a rather blurred DAP, when measured at the soma. In addition, it was shown that the DAP in CA1 cells does not depend on the back-propagating AP as the DAP remained after truncating the apical dendrite (Yue et al., 2005).

The other mechanisms are all possible as the required ion channels are known to be present in stellate cells (Ca$_{LVA}$: Bruehl and Wadman, 1999; Na$_P$: Magistretti and Alonso, 1999; Na$_R$: Castelli et al., 2007; Na$_T$: Magistretti and Alonso, 1999).

We do not assume that the DAP could be caused by network mechanisms because *in vitro* long-range connections are severed by the slicing procedure but local connections are mostly inhibitory (Sec. 1.4) so that network interactions would lead to inhibition rather than excitation.

Function

Because the DAP is a depolarization of the membrane potential close to spike threshold, it was hypothesized to facilitate burst firing. Indeed, Alessi et al. (2016) showed that the current threshold needed to elicit an AP was on average 42% smaller during the DAP compared to the resting potential. In a parallel dissertation project, Franziska Kümpfbeck corroborated this finding and additionally showed that the current threshold at different time points during the DAP reflects the DAP shape and that the current threshold is influenced by previous hyper-/depolarization (Fig. 1.6) (Kümpfbeck, 2019). On the other hand, Canto and Witter (2012) found that neurons without a prominent DAP do not burst at the onset of a step current whereas most principal cells do.

Bursting could support neural processing, for instance, by inducing long term potentiation (LTP) (Pike et al., 1999), more reliable transmission at synapses (Lisman, 1997) or the selective excitement of connected cells due to high-, low- or bandpass filtering properties of synapses or the post-synaptic neuron (Izhikevich et al., 2003). This could play a role in learning spatial representations of the environment or navigational planning as implemented by replay events (Skaggs and McNaughton, 1996; Wilson and McNaughton, 1994; Ólafsdóttir et al., 2018) that are associated with increased burst firing (Skaggs, McNaughton, et al., 2007; Staba et al., 2002).

The DAP could also directly influence spatial coding. In the model by Navratilova et al. (2012) grid field size and the spatial period of the grid depended on the time between the AP peak and the DAP maximum, however, this time was an order of magnitude longer than observed *in vitro*. Furthermore, learning could be influenced directly because the DAP, traveling into the dendrites, can potentiate the effect of excitatory postsynaptic potentials (EPSP) and thereby induce LTP (Mishra et al., 2016).
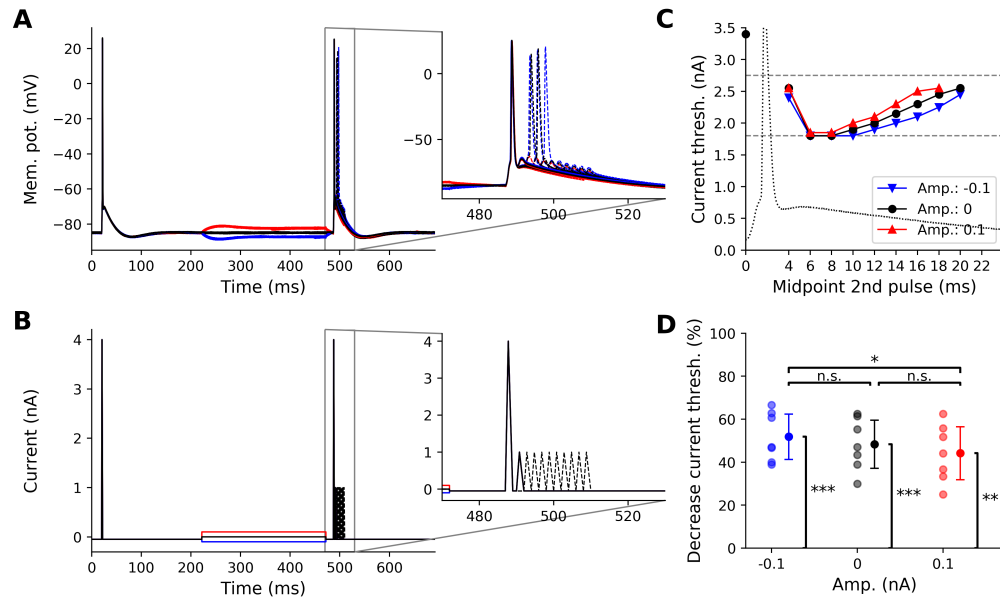
Fig. 1.6: Reduction of the current threshold during the DAP. A: Membrane potential of a MEC layer II cell in response to the injected current shown in B. As control an AP is elicited in the beginning. The baseline is set to -0.05 nA to keep the effect of the baseline and the hyperpolarization (blue), no polarization (black) and depolarization (red) apart. In the inset the experiment's main part is shown. The 1st triangular pulse is used to elicit an AP. The 2nd triangular pulse is used to test how much current is needed to elicit an AP at different time points during the DAP. C: Current threshold, i.e. the least amount of current needed to elicit an AP, for previous hyper-, no- and depolarization. The data point at 0 ms shows the current threshold at rest. The dashed lines indicate the range of amplitudes tested for this cell. The dotted line depicts the shape of the AP and DAP. D: Percentage of the decrease in current threshold from rest compared to the lowest threshold during the DAP for all cells plotted for previous hyper-, no- and depolarization. Next to it, the mean and standard deviation over cells is shown respectively. The decrease in current threshold was significantly different from zero in all three cases (t-test: * $p < 0.01$, ** $p < 0.001$, *** $p < 0.0001$). It was also significantly different between hyperpolarization and depolarization (paired t-test with Bonferroni-correction: * $p < 0.01$, ** $p < 0.001$, *** $p < 0.0001$). However, compared to no polarization significance was not reached. This is likely because not always the lowest possible current amplitude was tested so that at the minimum the points overlap as seen in C. The data for these figures were recorded by Kümpfbeck (2019).

1.6 Outlook

Grid cells in the MEC layer II encode spatial information. However, the code they are using, especially the role of frequently occurring bursts, is not understood. *In vitro* recordings of principal cells in MEC layer II have revealed that the AP is followed by a prominent DAP that could be the cause of such bursts, but its biophysical foundation and relation to burst firing *in vivo* has not been investigated yet.

The objective of this study is to understand the mechanism behind the DAP by creating a biophysical realistic model of a typical stellate cell in the MEC layer II and to draw a connection between DAPs and burst firing *in vivo*.

Firstly, it was investigated if the developed single-compartment model reproduced the main electrophysiological characteristics of stellate cells (Sec. 2.1.1).

In the model we studied which ion channels are necessary for the generation of the DAP by means of virtual blocking experiments (Sec. 2.1.2). Furthermore, a sensitivity analysis was conducted to find out which parameters in the model influence DAP characteristics (Sec. 2.1.3).

In vitro experiments showed that the DAP can facilitate burst firing by lowering the current threshold. We investigated whether DAPs occur *in vivo* (Sec. 2.2.1) and if there is a relationship between having a DAP and being classified as a bursty cell (Sec. 2.2.2).

Results 2

2.1 Biophysical foundation: Single-compartment model of the DAP

To investigate the biophysical foundation of the DAP, we created a single-compartment model of a typical MEC layer II stellate cell. We analyzed the mechanism behind the DAP by determining which ion channels are necessary for the generation of the DAP using virtual blocking experiments. Furthermore, a sensitivity analysis was conducted to investigate the influence of the model parameters on the DAP shape.

In the future, the model could be used to investigate the firing behavior of stellate cells under conditions closer to *in vivo*, for instance, by inserting synaptic input. Furthermore, the model could be easily included into network models of grid formation as continuous attractor networks (Burak and Fiete, 2009; Fuhs and Touretzky, 2006; McNaughton et al., 2006) or feed-forward models (Kropff and Treves, 2008; D'Albis and Kempter, 2017; Monsalve-Mercado and Leibold, 2017). This would allow to test whether network models still function with a biophysically realistic cell model and which effect electrophysiological characteristics as the DAP have on burst firing, phase precession, grid scaling etc.

2.1.1 Reproduction of the DAP and other stellate cell characteristics

The single-compartment model shown here includes four ion channels modeled according to the Hodgkin-Huxley formalism: a Na_T, Na_P, K_{DR} and HCN channel (model description in Sec. 4.1). The only correspondence between modeled and real ion channels before parameter fitting is the number of activation and inactivation gates and the equilibrium potential. The parameters of the model were iteratively fit using the L-BFGS-B algorithm with the root mean squared error (RMSE) between the membrane potential of the real and simulated cell as error function. For the training the triangular pulse experiment (Sec. 4.3.1) was applied as it displays the AP and DAP most clearly. The double triangular pulse, step current and ZAP protocol were used as validation set. The models that generalized the best on these protocols were used to narrow down the parameter range for the next optimization. This was repeated until a satisfactory model was obtained. The double-sine protocol was not included in the optimization procedure and could therefore be used for testing the model (see Sec. 4.2 for the optimization procedure).

In the following, we will show how well the model reproduces the stellate cell characteristics introduced in Sec. 1.3. The model shown is the same for all plots

and analyses, however, variations of the model can be found in the Suppl. Sec. 5.1.

The experimental data of the MEC layer II cells, that were used to test the model, were provided by Franziska Kümpfbeck (Kümpfbeck, 2019). The real cell used for the fit and the comparison had a drift in the resting potential over the whole recording, therefore all voltage traces are shown with the resting potential subtracted. For Fig. 2.3 and Fig. 2.7 a different cell is shown as not all protocols were conducted for this cell.

To quantify how well the model accords to the distribution of MEC layer II cells that have a DAP (MECII$_{DAP}$) (definition in Sec. 4.4.1), we estimated highest density regions (HDR) with respect to the main stellate cell characteristics (details in Sec. 4.4.2) (Hyndman, 1996). A HDR measures how many percent of the sample space have a higher or equal probability density than a specific value. This means, if a model characteristic has a 75% HDR with respect to the MECII$_{DAP}$ distribution, on average 25% of newly recorded MECII$_{DAP}$ cells will have lower probability density of that characteristic than the model. HDRs have an advantage over standard deviations, as they can be used for any, also multimodal and asymmetric distributions.

Reproduction of the DAP

To investigate AP and DAP generation a triangular pulse was injected into the cell to elicit a spike (Fig. 2.1). The simulated cell qualitatively reproduced the afterspike dynamics of the real cell as it showed a distinctive fast afterhyperpolarization (fAHP), DAP and medium afterhyperpolarization (mAHP). The RMSE between the voltage trace of the real and simulated cell in Fig. 2.1 was 3.5 mV, mainly because the model had a higher AP amplitude than the real cell. The DAP also deviated in amplitude, but the RMSE starting after the fAHP amounted only to 0.8 mV.
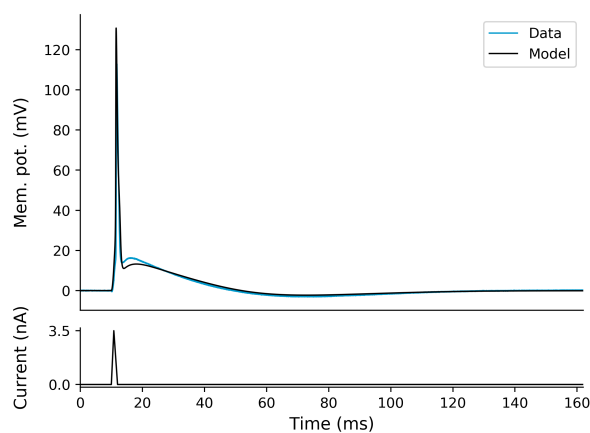
Fig. 2.1: Reproduction of the DAP. Membrane potential of the real (blue) and simulated cell (black) in response to a short triangular pulse (bottom plot).
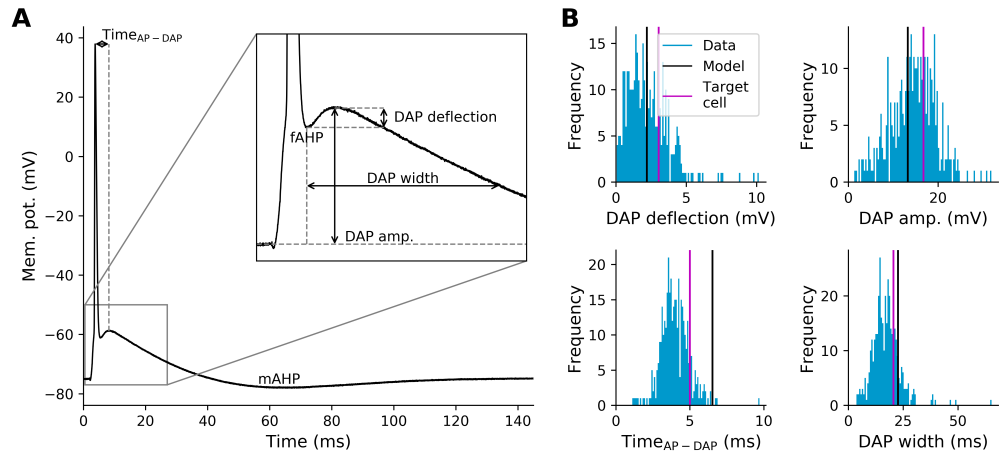
Fig. 2.2: DAP characteristics of the model in comparison to the MECII$_{DAP}$ population. A: Illustration of the different DAP characteristics. B: Distribution of the DAP characteristics for MECII$_{DAP}$ cells (blue), the values for the model (black) and the target cell (magenta) to which the model was fit.

When comparing different characteristics of the DAP (Fig. 2.2 A, definitions in Sec. 4.4.3) between the model and MECII$_{DAP}$ cells, the model lay within the MECII$_{DAP}$ distribution for DAP deflection (34% HDR), DAP amplitude (29% HDR) and DAP width (72% HDR), but lay at the outer range for Time$_{AP-DAP}$ (98% HDR) (Fig. 2.2 B). Looking at the distributions in 2D scatter plots, that visualize the interdependence of the characteristics, the model was also within the MECII$_{DAP}$ population but on the edge if plotted against Time$_{AP-DAP}$ (Suppl. Fig. 5.1).

One of the putative functions of the DAP is the reduction of the current threshold needed to elicit an AP during the DAP as demonstrated by the double tri-
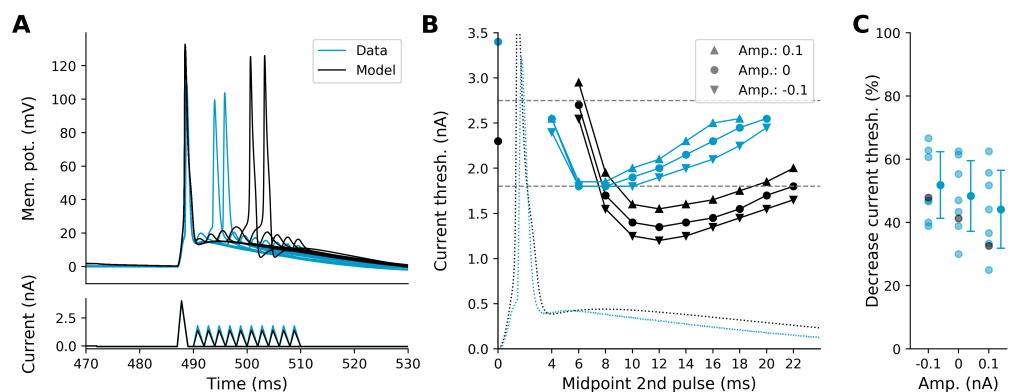
Fig. 2.3: Reproduction of the reduction in current threshold during the DAP. The model is compared to the recorded cell using the same protocol as in Fig. 1.6. A: Membrane potential of the real (blue) and simulated cell (black) in response to the double triangular pulse (bottom plot) with no step current applied (compared to the -0.05 nA baseline current) from 222 to 472 ms. B: Current threshold at rest (black and blue dot at 0 ms) and during the DAP for different amplitudes of the preceding step current (▲: 0.1 nA, ●: 0 nA, ▼: -0.1 nA). Dotted lines indicate the shape of the AP and DAP for the real and simulated cell, respectively. Dashed lines indicate the range of amplitudes tested in case of the experimental data. C: Percentage of the decrease in current threshold from rest compared to the lowest threshold during the DAP of real cells (blue) and the model (black). Next to it, the mean and standard deviation over real cells.

angular pulse experiment (Fig. 1.6). The model, tested on the same protocol (Fig. 2.3), also showed a reduction in the current threshold. However, the current threshold curve was shifted to the right, probably because the time span between the AP and the DAP maximum was higher in the model. Overall, the current threshold was lower in the simulated compared to the real cell but within the normal range of $MECII_{DAP}$ cells. In the model it can be seen that the current threshold was above the resting level when stimulating closer to the AP. The same could occur in real cells if stimulation would be done closer to the AP as expected from extrapolating the recorded data. Note also that a different cell is shown here than the one the model was fit to as the double ramp protocol was not conducted on that cell. The percentage of the decrease in current threshold (Fig. 2.3 C) in the model was similar to real cells for different amplitudes of the preceding step current.

Reproduction of the sag
In Fig. 2.4 A the real and simulated cell in response to a negative step current are shown. Both exhibited a sag, i.e. after attaining a peak at step current onset the membrane potential settles at a lower voltage deflection.

Looking at the sag over different amplitudes of the step current (Fig. 2.4 B), it can be seen that the model reproduced the under- and overshoot of the membrane potential at the sag for negative and positive step currents, respectively.

To quantify the sag, two measures were used: The steady state amplitude, defined as the difference between the voltage at steady state and the resting potential, and the sag deflection, that is the difference between the minimum of the sag and the voltage at steady state. The model had a similar steady state amplitude as the $MECII_{DAP}$ population (13% HDR). The sag deflection was at the lower range of the distribution (88% HDR).
Blocking the HCN channel by Cs^+ or ZD7288 in MEC layer II cells strongly reduced the sag (Dickson et al., 2000, Jones, 1994, Nolan et al., 2007). Replicating the effect of Cs^+ and ZD7288 by setting the conductance of the HCN channel in the model to zero also caused a strong decrease of the sag (Fig. 2.4 C).

Reproduction of the firing behavior
The firing behavior of the model was examined by inserting positive step currents of increasing amplitude. In response to a step current with an amplitude of 0.4 nA (Fig. 2.5 A) the simulated and real cell both showed tonic spiking. However, the model did not have a doublet at current onset as would be typical for stellate cells.

The spiking behavior was quantified by $ISI_{1/2}$ and the latency of the first spike. $ISI_{1/2}$ is the ratio between the 1st and 2nd ISI computed from the trace with the lowest step amplitude having at least four APs. (Three APs would be enough in principle, however, voltage traces with four APs exhibited more representative firing patterns.) The latency of the first spike is the time between the onset of

Fig. 2.4: Reproduction of the sag. A: Membrane potential of the recorded (blue) and simulated cell (black) in response to a negative step current. For the recorded cell, the sag deflection and steady state amplitude are indicated. The dashed lines mark from top to bottom the resting potential, the voltage at steady state and the sag peak, respectively. B: Comparison of the voltage at steady state versus the sag peak for the experimental data (blue) and the model (black). C: Membrane potential of the model without (black) and with 100% block (yellow) of the HCN channel. D: Sag deflection (difference between the sag peak and the voltage at steady state) and steady state amplitude (difference between the voltage at steady state and the resting potential) of the MECII$_{DAP}$ population (blue), the model (black) and the target cell (magenta).

the stimulus and the peak of the first spike. It was determined from the trace with the lowest step amplitude that had at least one AP. Fig. 2.5 B shows that the model lay within the MECII$_{DAP}$ population for ISI$_{1/2}$ (9% HDR) and the latency of the first spike (1% HDR).

The F-I curve (Fig. 2.5 C) shows the firing rate as function of the current amplitude. In the simulated cell the slope of the F-I curve was higher than for the real cell. Furthermore, the simulated cell showed a kink at the start of the F-I curve, which is an indicator of class 2 behavior (Izhikevich, 2007). This is consistent with the hypothesis that stellate cells in the MEC layer II undergo a subcritical Andronov-Hopf bifurcation (Izhikevich, 2007). In this bifurcation a transition from a stable resting state equilibrium to a stable limit cycle takes place whereby the period of the limit cycle determines the firing frequency causing a jump in the F-I curve. The kink could be smaller or not visible in real cells due to ion channel noise.
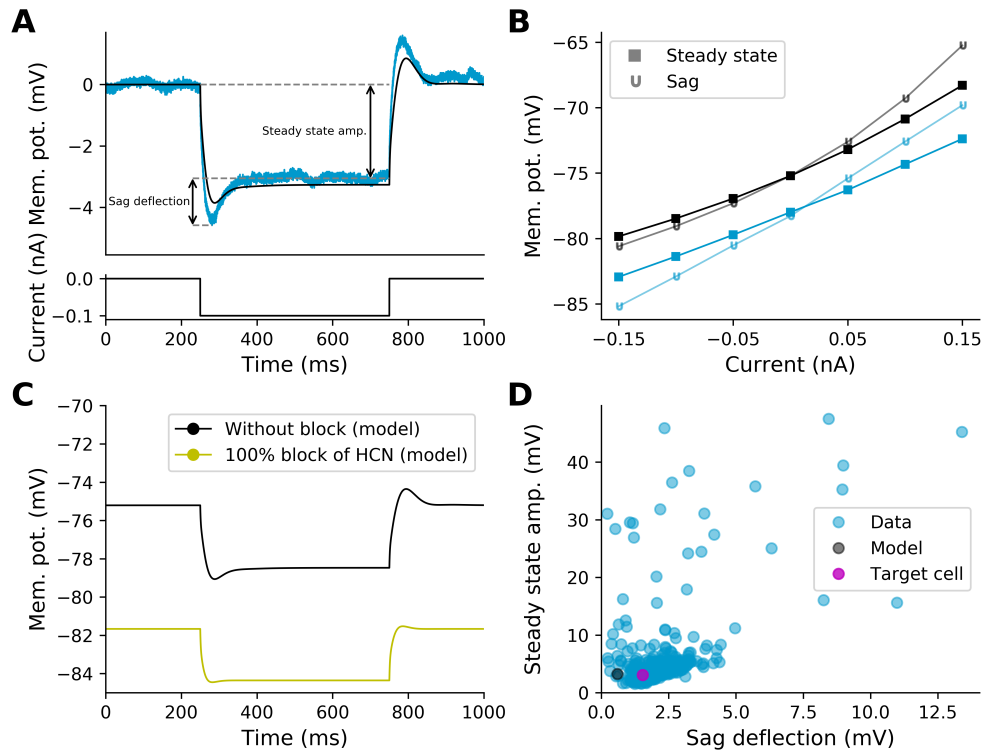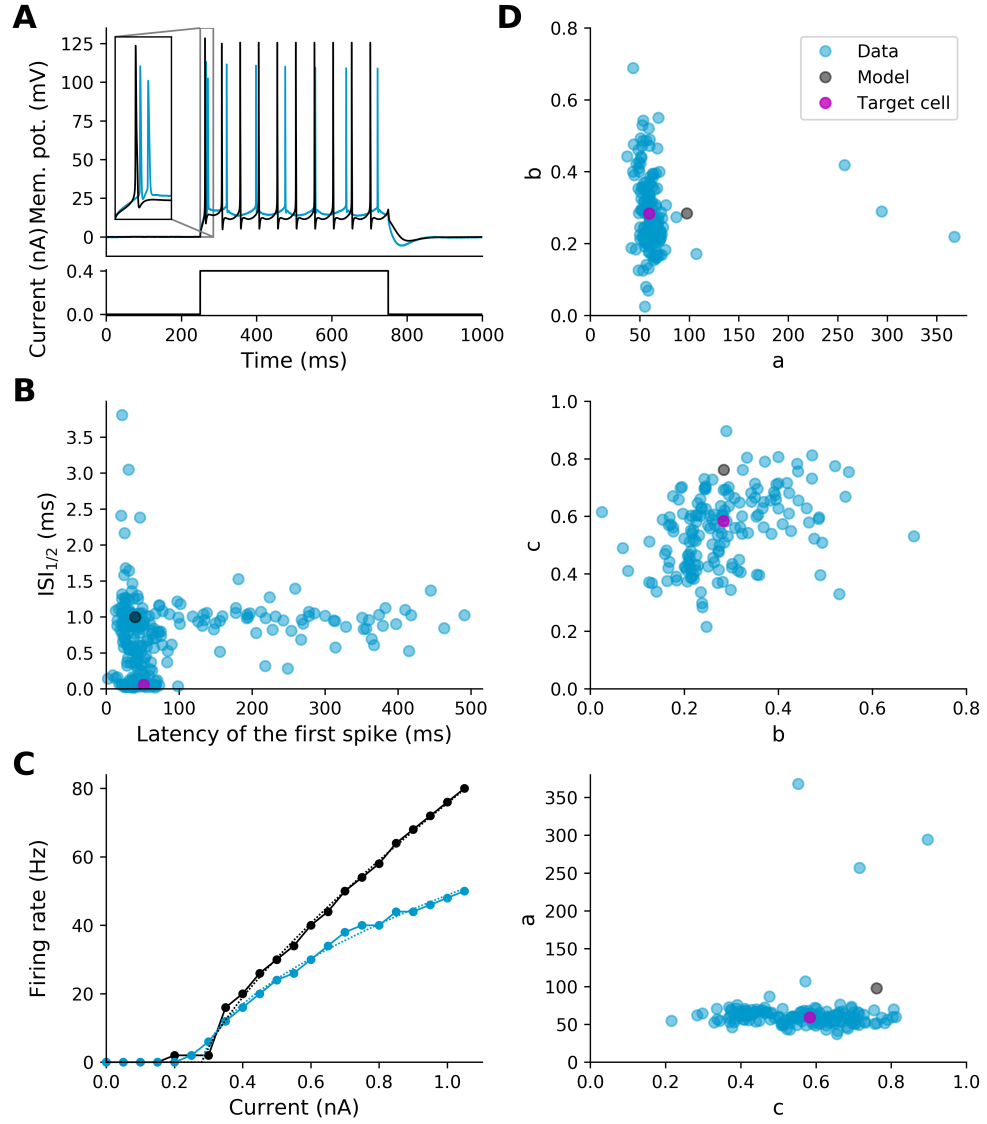
Fig. 2.5: Reproduction of the firing behavior. A: Membrane potential of the recorded (blue) and simulated cell (black) in response to a positive step current (bottom plot). The inset shows spiking at step onset. B: Latency of the first spike (when at least 1 spike was present) and $ISI_{1/2}$ (ratio between the first and second ISI when at least 4 spikes were present) in the $MECII_{DAP}$ population (blue), the model (black) and the target cell (magenta). C: F-I curve of the recorded (blue) and simulated cell (black). In dotted lines the fit of the F-I curve to Eq. 2.1 is shown. D: 2D plots for a (scaling), b (shift) and c (exponent) obtained by fitting the F-I curve to Eq. 2.1 for the $MECII_{DAP}$ population (blue) (where RMSE$\leq$20 Hz), the model (black) and the target cell (magenta).

The F-I curve was quantified by fitting the following function to it:

$$f(x) = \begin{cases} a \cdot (x - b)^c & \text{if } x \geq b \\ 0 & \text{else} \end{cases} \tag{2.1}$$

whereby f(x) was given in Hz and x in nA. As already assumed, the scaling parameter (a) lay outside the $MECII_{DAP}$ population (97% HDR) as the F-I curve of the model had a higher slope than most real cells (Fig. 2.5 D). The shift (b) was well within the $MECII_{DAP}$ population (35% HDR) indicating that the firing

threshold was similar to real cells. The exponent (c) was at the higher end of the MECII$_{\text{DAP}}$ population (89% HDR) because the F-I curve of the model was rather straight. All MECII$_{\text{DAP}}$ cells had an exponent smaller than one. This is an indication for class 2 behavior as a jump in the F-I curve leads to a high slope at the onset of firing followed by a slow rise in the F-I curve, which is better fit by exponents less than one. In the figure only cells with RMSE $\leq$ 20 Hz are shown so that the distribution was not dictated by bad fits.

Reproduction of the resonance

Fig 2.6 A shows the simulated and real cell in response to a ZAP current, a sinusoid increasing in frequency, commonly used to examine resonance behavior (Eq. 4.10). The simulated and real cell resonated with the stimulus for certain frequencies which is reflected in the increased amplitude of the membrane potential oscillations.

The impedance curve (Eq. 4.16) was used to compute the resonance frequency determined as the frequency where the impedance is maximal and the Q-value, the ratio between the maximal impedance and the impedance at frequency zero (Fig. 2.6 B). The resonance frequency was 6 Hz for the model. This is in accordance with MEC layer II stellate cells that are known to resonate in the
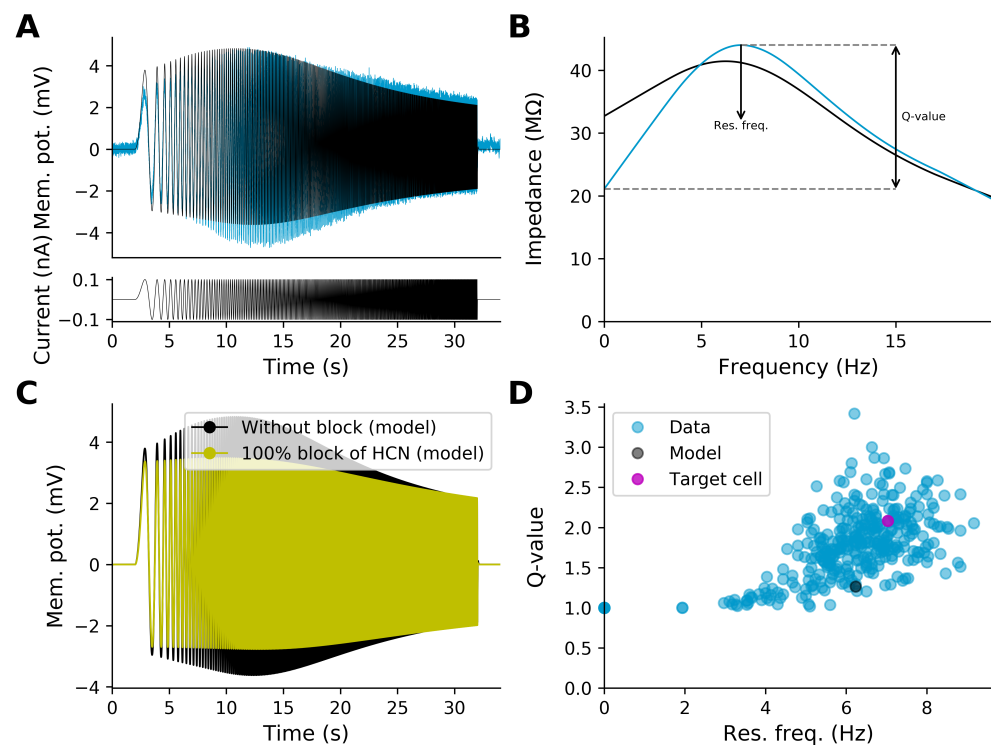
Fig. 2.6: Reproduction of the resonance. A: Membrane potential of the recorded (blue) and simulate (black) cell in response to a ZAP current (bottom plot). B: Impedance computed from the traces shown in A. C: Membrane potential of the model without (black) and with 100% block (yellow) of the HCN channel. D: Resonance frequency and Q-value of the MECII$_{\text{DAP}}$ population (blue), the model (black) and the target cell (magenta).

theta range (5-11 Hz) (Canto and Witter, 2012; Erchova et al., 2004; Haas and White, 2002). The Q-value was 1.3 in the model. Both values were within the distribution of MECII$_{DAP}$ cells (Res. freq.: 21% HDR; Q-value: 79% HDR) (Fig. 2.6 D).

Setting the conductance of the HCN channel to zero reduces the resonance in the model (Fig. 2.6 C). This is similar to the response of MEC layer II stellate cells in HCN1 knock-out mice or when HCN channels are blocked (Nolan et al., 2007; Heys et al., 2010).

Testing the model on a new stimulus

The double-sine experiment was designed to emulate the input to a grid cell when the animal traverses a firing field. It was based on the observation of Schmidt-Hieber and Häusser (2013) and Domnisoru et al. (2013) that during a firing field crossing the membrane potential slowly ramps up and down and is superimposed by theta oscillations. We imitated this activity pattern by injecting a ramp plus theta oscillation as input stimulus. The ramp was modeled as the upper half of a sine with a frequency of 0.1 Hz. The theta oscillation was realized by a sine with a frequency of 5 Hz (Fig. 2.7 A).
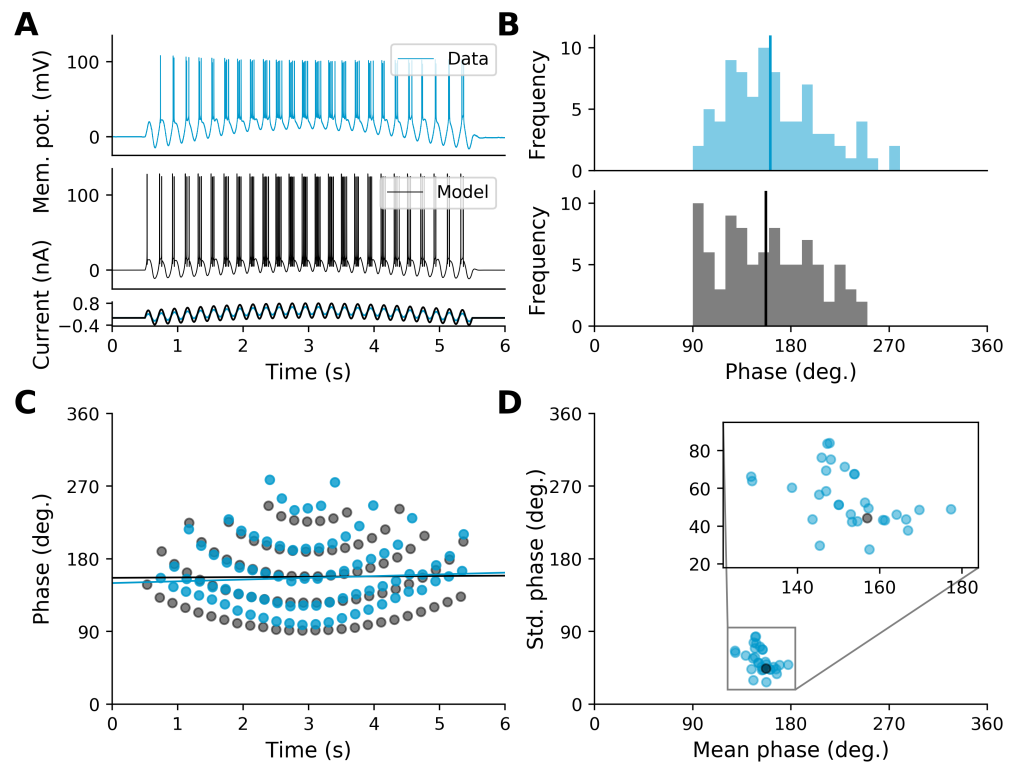
Fig. 2.7: Testing the model on a new stimulus. A: Membrane potential of the recorded (blue) and simulated cell (black) in response to the double-sine stimulus (bottom plot). B: Phase histogram of the APs with respect to the theta oscillation for the traces shown in A. C: Phases of the AP peaks with respect to the theta oscillation as a function of time and the linear regression lines fit to them. D: Mean and standard deviation of the phase histogram for the MECII$_{DAP}$ population (blue) and the model (black).

The firing behavior encountered *in vitro* was different to what was found *in vivo* as, for instance, fewer bursts were present *in vitro*. Those differences are likely to be caused by the lack of synaptic inputs. Nevertheless, the experiment is a good test set for the model as it was not used for the optimization.

To evaluate the model performance the distribution of the phases of the AP peak with respect to the theta oscillation was examined (Fig. 2.7 B). APs of the simulated and real cell preferably occurred during the up-phase of the sine whereby the circular mean phase was slightly before the peak of the sine. The circular mean phase differed only by 4 deg. between the simulated and real cell. The peaks in the distribution arise from the fact that towards the middle of the ramp several spikes are fired at a certain interval. In the model, the position of the first spike varied less than in the data (mean $\pm$ std., model: 108 ± 15 deg.; data: 126 ± 20 deg.), so that the first peak in the distribution was higher. Comparing the performance of the model with an inhomogeneous Poisson process (see Sec. 4.4.5 for details), where the input stimulus scaled to the average firing rate of the data was used as firing rate, showed that the RMSE between the phase distribution of the model and the data was significantly lower (p-val.<0.001). The model deviated on average 1 AP/bin less from the data than the inhomogeneous Poisson process.

Looking at the distribution of the mean and standard deviation of AP phases (Fig. 2.7 D), the model exhibited similar values as $MECII_{DAP}$ cells (Mean phase: 43% HDR; Std. phase: 17% HDR). Note that in this plot the amplitude of the two sines varies since each cell was tested on a different set of amplitudes.

Fig. 2.7 C depicts the AP phase in dependence of the time of occurrence. It shows that with increasing ramp more APs were fired within one theta oscillation and APs occurred progressively earlier. The reverse happened for decreasing ramp so that on average no phase precession occurred with respect to the intrinsic theta oscillation. Phase precession was quantified by linear regression on the AP phases. The slope of the linear regression line was 0.4 deg./s in the model and 2.1 deg./s in the data. As the emulated firing field in this experiment had a duration of 5 s, these values correspond to a change of 2.0 deg. per field in the model and 10.5 deg. per field in the data. In Schmidt-Hieber and Häusser (2013) the slope was 4 deg. per field with respect to the intrinsic and -137 deg. per field with respect to the extracellularly measured theta oscillation. Domnisoru et al. (2013) reported that the phase difference between the first and last eighth of a field amounted to -1.1 ± 43.2 deg. with respect to the intrinsic and 76.2 ± 50.5 deg. with respect to the extracellularly measured theta oscillation (note that with this measure the sign is reversed). The slope of the AP phases with respect to the intrinsic theta oscillation found in the model and the data in this study are thus within the variance found *in vivo* consistent with an absence of phase precession. However, the distribution of phases is much more structured *in vitro* due to the absence of synaptic noise and the regularity of the theta oscillation.

2.1.2 The mechanism behind the DAP

Having confirmed that the model reproduces the DAP and the main stellate cell characteristics, the mechanism behind the DAP could be investigated. Firstly, the relationship between the ion channels in the model and real ion channels was explored. Secondly, we investigated which ion channels are necessary for the generation of the DAP by virtual blocking experiments. Finally, the influence of the model parameters on DAP characteristics was examined using a sensitivity analysis.

Identifying ion channels in the model

The parameters of the ion channels in the model were completely determined by the optimization algorithm (only the number of activation and inactivation gates and the equilibrium potential had been set beforehand). As the parameter ranges (shown in Tab. 4.4) were not tailored to specific ion channels but only required to agree with the orders of magnitude of physiological data, fitting the parameters does not necessarily generate known ion channels. In fact, we do not expect a one-to-one mapping of fit to real ion channels for the following reasons: i) The fit ion channels could be a combination of several real ion channels. ii) Similar ion channel behavior could have different implementations. iii) The model has to compensate for all the deviations from real cells that are relevant for the voltage response as the morphology, the presence or absence of ion channels, the complexity of the ion channels etc. Nevertheless, there should be some correspondence between fit and real ion channels because of the prescribed structure and the similar functionality that is achieved at the cell level.

A legend of the parameters and the corresponding model equations can be found in Tab. 4.1 and Eq. 4.1-4.9. Comparing the parameters of fit and real ion channels based on their assumed type (Tab. 2.1) shows that V_h (besides V_h of Na_P) and the range of the time constant are similar. V_h deviates on average by 10.2 mV and the time constant by 2.58 ms. These numbers are comparable to variations between different recordings. For instance $V_{h,h}$ was reported to be -59.8 mV by Magistretti and Alonso (1999), but -69.0 mV by Hargus et al. (2011) which is a difference of 9.2 mV. $V_{s,m}$ was stated to be 3.6 ms by Magistretti and Alonso (1999), but 6.6 ms by Hargus et al. (2011) differing by 3.0 ms. It should also be noted that the recorded data was not corrected for the liquid junction potential which means that V_h might be shifted. Furthermore, the recordings were made at a lower temperature, so that the recorded time constants should be considered as a lower bound (Q_{10} values were not estimated so that the time constants could not be corrected). Na_P $V_{h,h}$ might be more negative in the model because of one of the reasons i), ii), iii) stated above. For instance, the Na_P channel might had to compensate for the absence of a Na_R channel (consistent with the Na_P channel having a resurgent component as shown below). The parameter V_s tended to higher values in the fit ion channels. It deviated on

| | Na$_T$ | | K$_{DR}$ |
	m	h	m
V_h (mV)	-32.5 $\pm$ 6.5|-30.94	-59.8 $\pm$ 5.2|-60.44	-74.3 $\pm$ n.a.|-68.29
V_s (mV)	3.6 $\pm$ 0.9|11.99	-4.5 $\pm$ 0.9|-13.17	15.0 $\pm$ n.a.|18.84
$min\ \tau$ (ms)	n.a.|0.00	n.a.|0.19	n.a.|0.714
$max\ \tau$ (ms)	n.a.|0.12	n.a.|4.40	n.a.|12.201

| | Na$_P$ | | HCN |
	m	h	h
V_h (mV)	-44.4|-52.82	-48.8|-82.54	-67.4|-77.9
V_s (mV)	5.2|16.11	-10.0|-19.19	-12.66|-20.54
$min\ \tau$ (ms)	n.a.|1.17	1.53|0.83	2.68|4.342
$max\ \tau$ (ms)	n.a.|7.68	6.48|7.05	74.14|81.523

Tab. 2.1: Parameters of experimentally recorded (left value) and fit ion channels (right value) of MEC layer II stellate cells. A legend of the parameters and corresponding model equations can be found in Tab. 4.1 and Eq. 4.1-4.9. For the recorded values either the mean $\pm$ standard deviation over cells are given or the value obtained from averaged data. Note that the recorded data is not corrected for the liquid junction potential so that V_h might be shifted and that the data was measured at a lower temperature resulting in higher time constants (Q$_{10}$ values were not estimated so that the time constants could not be corrected). For the time constants the global minimum and maximum in the range [-95, 30] (mV) are reported. The references for the different ion channels are: Na$_T$: (Magistretti and Alonso, 1999), Na$_P$: (Magistretti and Alonso, 1999), K$_{DR}$: (Eder and Heinemann, 1996), HCN (fast component): (Dickson et al., 2000).

average by 8.2 mV. The reason might be that V_s not only sets the slope for the steady state curve, but also determines the width of the bell-shaped time constant curve, so that there is a trade-off between the two.

In the following, the type of each ion channel in the model will be analyzed further by virtual voltage clamp experiments (Fig. 2.8, protocols described in Sec. 4.4.6).

Na$_T$

To visualize Na$_T$ currents (Fig. 2.8 E) the ion channel has to be brought into a closed and non-inactivated state by clamping at a sufficiently negative potential. From there different voltages can be tested. Na$_T$ channels would respond to more positive potentials with a transient response, i.e. a negative current that peaks within a few milliseconds and then decays to zero (Magistretti and Alonso, 1999; Hargus et al., 2011; Nigro et al., 2012). This is caused by the fast opening of the sodium channel followed by inactivation.

The Na$_T$ channel in the model exhibited a transient response. However, the current decayed to a constant, non-zero value showing that the Na$_T$ channel also had a persistent component. Persistent activity is not completely avoidable with the Hodgkin-Huxley formalism as it occurs as soon as the activation and inactivation steady state curve overlap. The current caused by this overlap is also called window current. Experiments that isolate the Na$_T$ current by subtracting traces without TTX from traces with TTX applied also displayed a window current

(Magistretti and Alonso, 1999). However, single-channel recordings showed that Na$_T$ channels do not have late opening (Magistretti, Ragsdale, et al., 1999) so that this current has to arise from other ion channels.

In summary, the Na$_T$ channel in the model reflects the recorded Na$_T$ channels (Magistretti and Alonso, 1999). But both are probably a conglomerate of different sodium channel subtypes as indicated by the persistent activity.
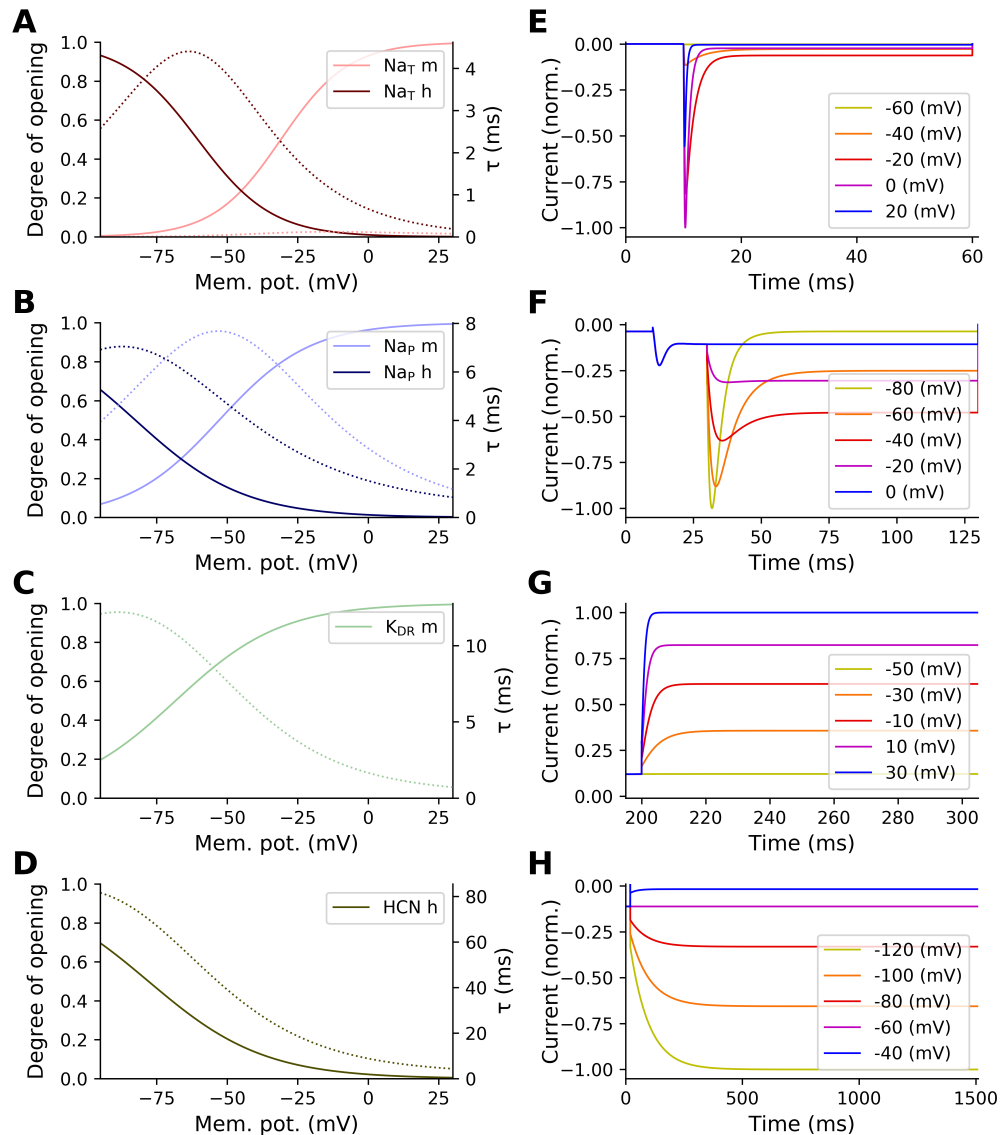
Fig. 2.8: Characterization of the ion channels in the model. Steady state curve (solid lines) and time constants (dotted lines) of the activation and inactivation gate of the Na$_T$ (A), Na$_P$ (B), K$_{DR}$ (C) and HCN channel (D). E, F, G, H: Ionic current flow in response to a standard voltage clamp protocol (described in Sec. 4.4.6) for the same channels as on the left.

Na$_P$

As the Na$_P$ channel is involved in the generation of the DAP (see virtual blocking experiments below) we wanted to examine more closely to which type of sodium channel it corresponds, which was not prescribed by the optimization procedure.

In particular, sodium channels can show transient, persistent and/or resurgent components that can all be visualized by the following voltage clamp protocol (Fig. 2.8 F) (Lewis and Raman, 2014).

The protocol starts with a step hold at -80 mV for 10 ms bringing the sodium channel to a closed, non-inactivated state. Then a step to 0 mV continuing for 20 ms is applied. A negative current during this step indicates the transient component that is caused by fast opening of the sodium channel followed by inactivation. The third step iterates over several voltages and lasts 100 ms. As Na_T channels are inactivated from the previous step, they show no response. However, Na_R channels cause a negative current due to fast de-inactivation (Hargus et al., 2011; Nigro et al., 2012). Subsequently, the current can approach a constant value representing the persistent component.

The Na_P channel in the model showed all three components. The transient response was smaller in the simulated compared to real recordings probably, because in the experiments not only the resurgent current was recorded but all ion channels affected by TTX. Single-channel recordings showed that transient and resurgent activity can occur in the same ion channel (Raman and Bean, 1997), but this was not investigated for persistent activity.

It can be concluded that the Na_P channel in the model shows both, resurgent and persistent components. However, it is not known whether it is one or several sodium channel subtypes causing it.

The resurgent component in the Na_P channel of the model critically depends on $\tau_{max,m}$. This is because stepping from 0 mV to a more negative potential causes ion channel closing and slight release from inactivation. If $\tau_{max,m}$ is large enough, ion channel closing will be slower than de-inactivation so that for a short amount of time current flow is increased creating the resurgent component. The parameter $\tau_{max,m}$ was also shown to correlate significantly with DAP characteristics (see Sec. 2.1.3) indicating that the resurgence is important.

K_{DR}

To investigate the kinetics of the K_{DR} channel (Fig. 2.8 G) it is first brought into a closed, non-inactivated state by clamping the voltage at -110 mV for 150 ms. The fast transient current of A-type potassium channels (K_A) was inactivated by stepping to -50 mV for 50 ms. The current flow of K_{DR} channels was then measured by clamping at different voltages for 150 ms. K_{DR} channels would respond with a sustained positive current with slow inactivation (Eder and Heinemann, 1996).

The K_{DR} channel in the model showed a persistent current similar to experimentally recorded channels (Eder and Heinemann, 1996). However, no slow inactivation was seen as an inactivation gate was not included in the ion channel.

The stellate cell model only needed K_{DR} but not K_A channels. This is consistent with the fact that stellate cells in the MEC layer II exhibit prominent K_{DR} but only small K_A currents (Eder and Heinemann, 1994).

HCN

The voltage protocol for the HCN channel (Fig. 2.8 H) starts with a voltage step to -60 mV for 20 ms so that the HCN channel is in a non-inactivated state. With the second step different voltages can be tested. As the HCN channel has a high time constant it was made to last 1500 ms. For potentials below -60 mV experimentally recorded HCN channels showed an increase in current flow due to release from inactivation and approximated a constant value within a time scale of hundreds of milliseconds (Dickson et al., 2000).

The HCN channel in the model also rose slowly to a constant value. The time constant was similar to the one reported for the fast component of the H-current by Dickson et al. (2000).

Virtual blocking of ion channels

Not all ion channels in the model have to contribute to the generation of the DAP. To find out which ion channels are necessary and therewith which hypothesis for DAP generation holds (Sec. 1.5), we simulated the blocking of ion channels. In these experiments a triangular pulse was injected into the model as it elicits an AP with a prominent DAP.

At first, each ion channel was blocked separately by different degrees during the whole experiment (Fig. 2.9 A, B, C). This was realized in the model by reducing the maximal conductance by a given percentage. However, blocking during the whole experiment also leads to changes of the AP so that it is impossible to distinguish whether the blocking of the ion channel or the changed voltage trace affected the DAP. In the worst case, there is not even an AP elicited as, for instance, with 100% block of the Na_T and Na_P channel (Fig. 2.9 C). Alessi et al. (2016) tried to minimize the effect of the reduced sodium influx on the AP by manually adjusted current injection. This can preserve the AP, but the shape will not be the same. In the model it is possible to apply blocking starting from a specific point in time. In Fig. 2.9 D, E, F ion channel blocking was started after the AP at the fAHP minimum.

Blocking the Na_T channel led to a slight reduction of the DAP, but the DAP was still present under 100% block. Reducing the maximal conductance of the Na_P channel decreased the DAP more strongly. At 100% block the simulated cell even exhibited an afterhyperpolarization. When blocking the K_{DR} channel, the model went into a high-frequency discharge for 50% block and a depolarization block for 100% block. This inability to go down to the resting potential was expected as the K_{DR} channel is responsible for AP repolarization. The HCN channel caused only a minor reduction in the DAP when it was blocked, but the resting potential was greatly reduced. This is because the HCN channel is open for negative potentials but inactivates upon depolarization (Fig. 2.8 D). Removing the leak current also led to a high-frequency discharge when the conductance was decreased as it is responsible for keeping the membrane potential more negative.

These results show that it is possible to remove the HCN or Na_T channel without
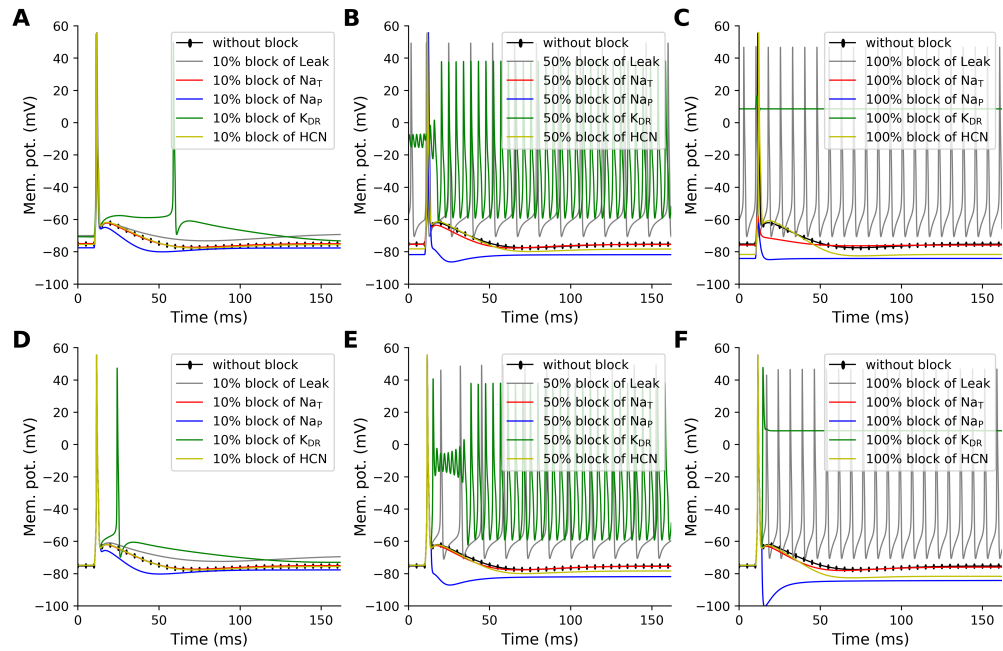
Fig. 2.9: Effect of blocking ion channels on the DAP when stimulating with a triangular pulse. Blocking a certain ion channel (Na_T: red, Na_P: blue, K_{DR}: green, HCN: yellow) by 10%, 50% or 100% during the whole recording (A, B, C) or only after the fAHP minimum (D, E, F).

destroying the DAP. They are therefore not necessary for DAP generation and hypothesis 4 (the window current of the Na_T channel causes the DAP) can be refuted. Instead, the DAP is the effect of balancing Na_P, K_{DR} and leak currents corresponding to hypothesis 5. Furthermore, resurgent and persistent currents were involved caused by the Na_P channel. This means that hypothesis 2 and 3 also could play a role. Hypothesis 1 was excluded from the outset as we did not take the morphology into account showing that in principle a DAP is possible without dendrites.

The results we obtained here are consistent with blocking experiments in real cells. Alessi et al. (2016) showed that the DAP is reduced by blocking with TTX or AEA, a more selective blocker of Na_P and Na_R channels. As TTX blocks several subtypes of sodium channels, it can only be derived from the experiments that some sodium channel was involved. The more selective blocker AEA on the other hand indicates a role for the Na_P and Na_R channel. This concurs with the necessity of the Na_P channel in our model. The DAP was also shown to depend on Kv2 channels that underlie K_{DR} currents (Hönigsperger et al., 2017). This accords with the fact that K_{DR} was necessary in the model to elicit a DAP.

Ionic currents during the DAP

An advantage of the model is that the different ionic currents can easily be visualized. In Fig. 2.10 the flow of ionic currents during the AP and DAP is shown. The AP upstroke is caused by the influx of sodium ions due to the Na_T channel. The downstroke of the AP is driven by the K_{DR} channel. For the DAP only
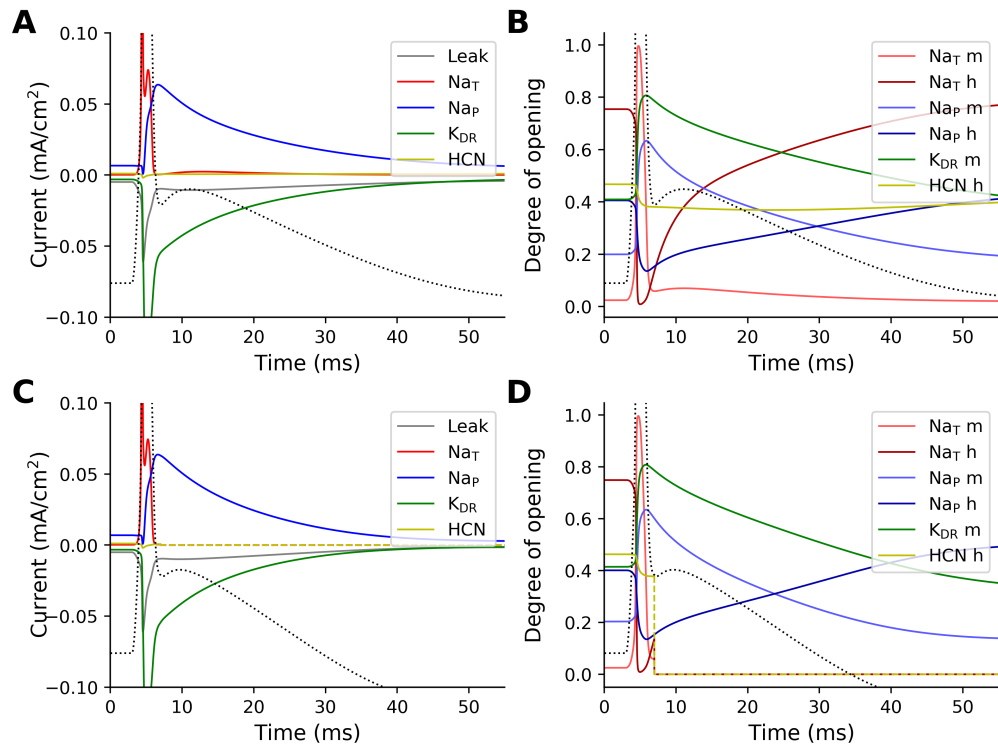
Fig. 2.10: Ionic currents flowing during the DAP. Ionic currents (A, C) and opening of ion channel gates (B, D) during the DAP. In C and D the Na_T and HCN channel were blocked completely after the fAHP minimum (indicated by the dashed lines). The membrane potential is shown as reference by a black, dotted line.

the Na_P channel, the K_{DR} channel and the leak current are necessary, therefore, in Fig. 2.10 C the ionic currents are shown when the Na_T and HCN channel are blocked after the fAHP minimum. The DAP seems to arise from the slight difference in the decay of the Na_P and the K_{DR} channel, so that the currents do not cancel completely. In Fig 2.10 A, B it can be seen that the Na_T channel reopens around the peak of the DAP and so contributes to it.

2.1.3 The effect of model parameters on DAP characteristics

In vitro there is a lot of variation in the shape of the DAP between cells (Fig. 2.2). We were interested how the DAP shape is influenced by the model parameters and therefore conducted a sensitivity analysis.

For the sensitivity analysis one million models were generated by randomly sampling parameters one order of magnitude around the original parameters. The sampled models were simulated given a triangular pulse as input. From their response the AP amplitude, AP width, fAHP amplitude and DAP characteristics (DAP deflection, DAP amplitude, DAP width and Time$_{AP\text{-}DAP}$) were computed. For all models for which the characteristics were available and within the valid ranges defined in Tab. 4.5 (3 587/1 000 000 models) a correlation analysis was performed between each model parameter and DAP characteristic. Correlations

were computed by Kendall's tau, as it is a robust, non-parametric method (Knight, 1966). However, Spearman's and Pearson's correlation coefficient gave similar results (Suppl. Fig. 5.2).

Two analyses were conducted on the models. Firstly, it was tested whether the data set was large enough to estimate correlations. This was done by dividing the data set into 35 subsets with 102 models each. For every subset the correlations between model parameters and DAP characteristics were computed and it was checked whether the standard deviation of the correlations over data sets were low. Secondly, it was investigated whether strong and significant correlations exist in the whole data set. For the significance test the p-values derived from Kendall's tau were adjusted using the Bonferroni correction to account for multiple testing.

The first analysis (Fig. 2.11 A) revealed that the standard deviations of the correlations over data sets were low. The highest standard deviation was 0.1 which, compared to the scale of correlation coefficients $[-1, 1]$, is small. This means that the original data set was large enough to obtain reliable correlations.

The second analysis (Fig. 2.11 B) showed that there were significant correlations between the parameters and the DAP characteristics. The strongest correlations had the parameter $V_{s,m/h}$ of the Na_T, Na_P and K_{DR} channel and $\tau_{max,m/h}$ of the Na_P channel. However, even the strongest correlation, that was between the DAP amplitude and Na_P $V_{s,m}$, amounted only to -0.3 suggesting that it is difficult to shape the DAP by only one parameter. Note that the Na_T channel can influence the DAP although it is not necessary for its generation as parameter

Fig. 2.11: Sensitivity analysis. A: One standard deviation around the mean of the correlations (Kendall's tau) between the model parameters and DAP characteristics when the data set was divided into 35 subsets with 102 candidates each. B: Correlations (Kendall's tau) between the model parameters and DAP characteristics over the whole data set with Bonferroni corrected p-values (p-val. < 0.1, 0.01, 0.001 = *, **, ***).

changes can cause an increase or decrease of current flow during the DAP. The results should be taken with a grain of salt, because even though the models were filtered for showing a reasonable AP and DAP, they could fail to reproduce other stellate cell characteristics.

All in all, the results corroborate the finding that the Na_P and K_{DR} channel are important for the DAP mechanism. The significant correlations with $\tau_{max,m}$ of the Na_P channel (whose role was explained in Sec. 2.1.2) indicates that the resurgent sodium current is necessary for DAP generation. The Na_T channel can influence the DAP shape, probably by increasing or decreasing the current flow during the DAP as seen in Fig. 2.10 A. These findings could be used to guide fitting the model to stellate cells with differently shaped DAPs by concentrating the optimization on the significant and most strongly correlated parameters. Furthermore, they predict causes for the variations in the DAP shape of MEC layer II cells.

2.2 DAPs *in vivo*: Analysis of the data from Domnisoru et al. (2013)

DAPs have been found in the majority of principal cells in the MEC layer II *in vitro* (Canto and Witter, 2012). However, it was not investigated so far whether DAPs occur and if they are relevant for the firing behavior *in vivo*.

To address these questions, we examined the data set from Domnisoru et al. (2013) that contained *in vivo* whole-cell recordings of grid cells (Sec. 4.3.2).

2.2.1 Do DAPs occur *in vivo*?

In Fig. 1e of the paper by Schmidt-Hieber and Häusser (2013) a cell exhibiting a presumable DAP *in vivo* was shown. *In vivo* it is not possible to distinguish unambiguously between the intrinsic subthreshold activity of the cell and any kind of noise based on a single observation. Therefore, to detect whether a cell exhibited a DAP we averaged over all APs in the recording so that the noise was canceled out. We refer to the averaged membrane potential trace around an AP as the spike-triggered average (STA_V) of the cell.

Spike-triggered average of the membrane potential (STA_V)

In the data set from Domnisoru et al. (2013) 5 of 26 cells (s79_0003, s104_0007, s109_0002, s110_0002, s119_0004) showed a DAP in the STA_V (Fig. 2.12). A DAP was said to be present if the DAP deflection exceeded the standard error of the mean (SEM) at the time point of the DAP maximum. A time-resolved histogram over voltages was computed for each cell to check if there were several modes in the distribution. This was not the case (Fig. 2.13).

DAPs occurred in three stellate and two non-identified cells. When only APs from a presumably good part of the recording were included in the STA_V (as shown in the next section), one pyramidal cell (*s73_0004*) and one non-identified
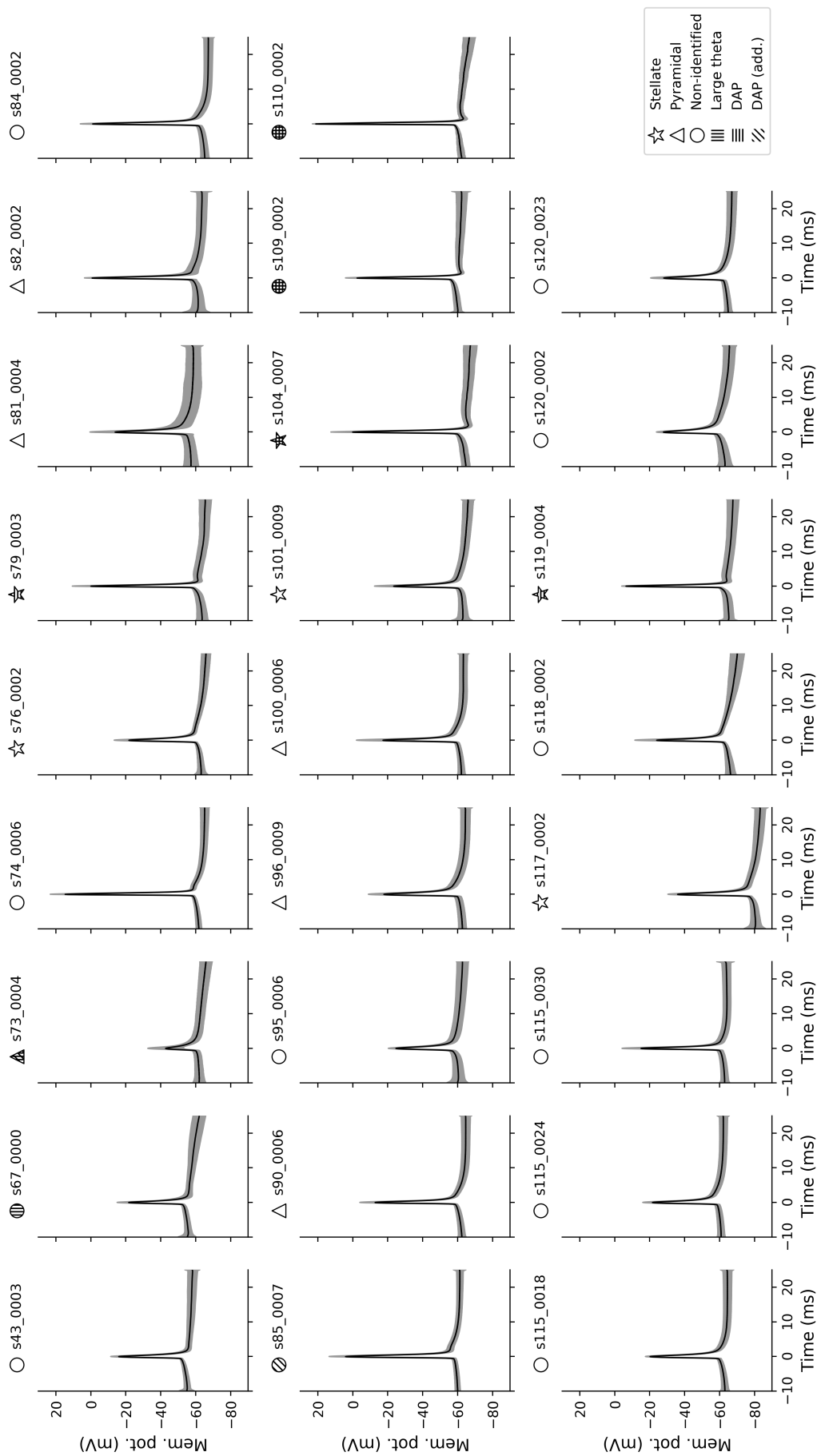
Fig. 2.12: STA$_V$ for all grid cells. For each cell the symbol indicates the cell type (star: stellate cell, triangle: pyramidal cell, circle: cell type not identified), whether the cell exhibited large theta oscillations (vertically striped) and whether the cell had a DAP (horizontally/diagonally striped). Whereas DAPs indicated by horizontal stripes can already be seen in the STA$_V$ shown here, additional DAPs become visible when the APs are filtered by AP amplitude and width before computing the STA$_V$ as explained in Sec. 4.4.8.

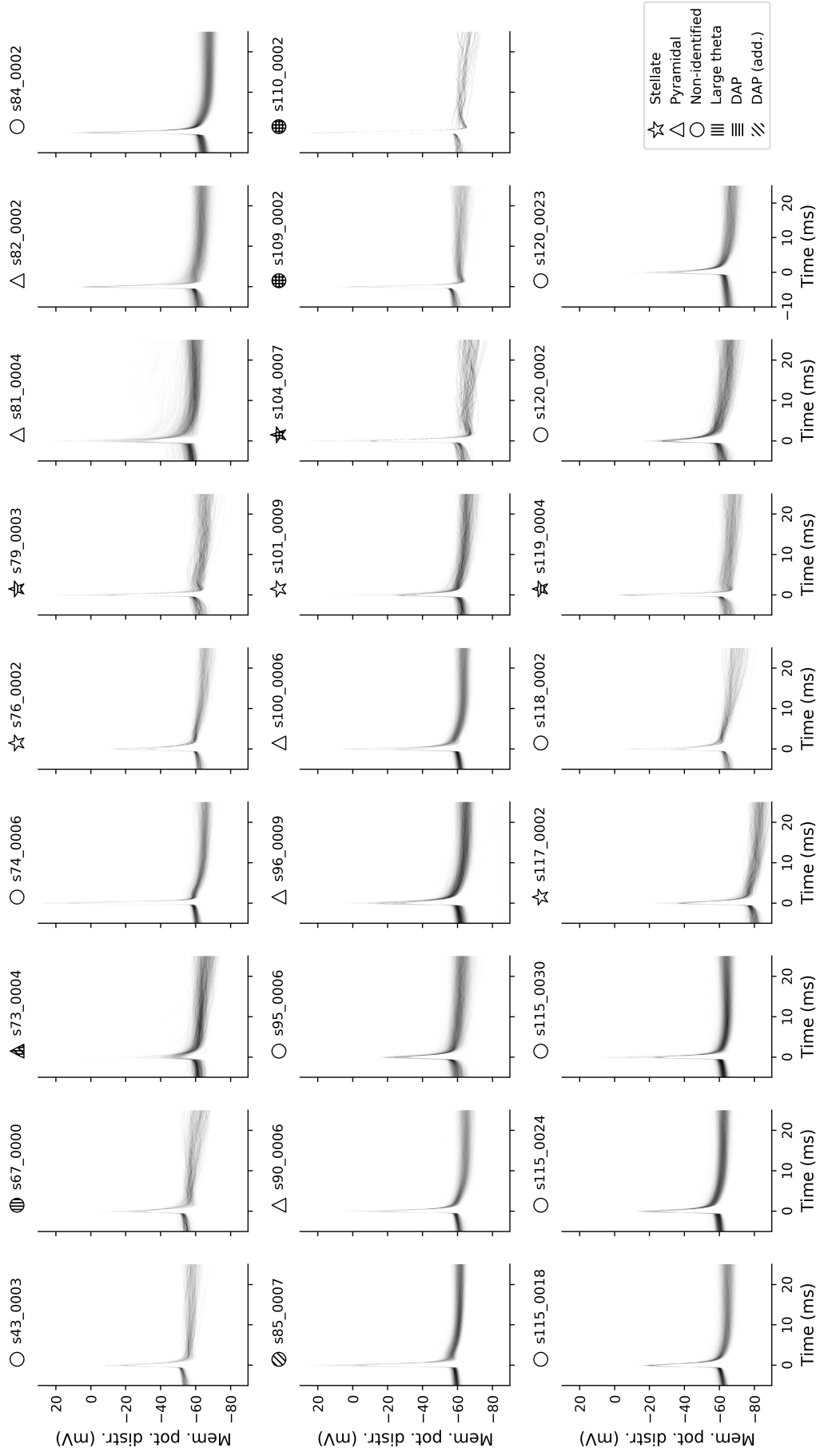**Fig. 2.13:** Time-resolved voltage histogram of all grid cells. For each cell the symbol indicates the cell type (star: stellate cell, triangle: pyramidal cell, circle: cell type not identified), whether the cell exhibited large theta oscillations (vertically striped) and whether the cell had a DAP detectable in the STA_V (horizontally striped) or in the STA_V from selected APs (diagonally striped).

cell (s85_0007) also showed a DAP. However, the pyramidal cell had very few dendrites, so that the classification was not as clear as for the other cells.

For the cells with a DAP the DAP deflection and $\text{Time}_{\text{AP-DAP}}$ were determined (Fig. 2.14). DAP amplitude and DAP width could not be computed because *in vivo* there is no resting potential that could serve as a reference value. Cells with large theta oscillations (large-theta cells) had a higher DAP deflection and $\text{Time}_{\text{AP-DAP}}$ than other cells.
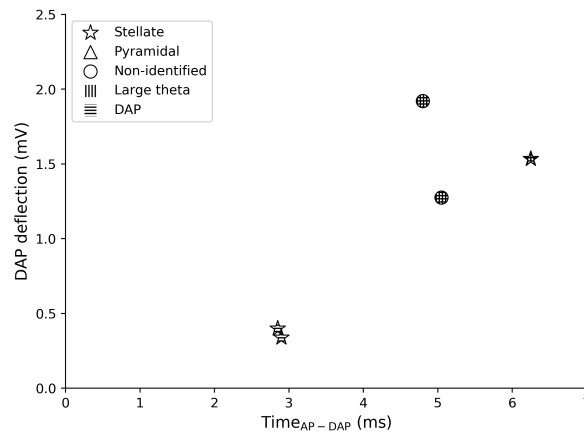

Fig. 2.14: DAP deflection as a function of $\text{Time}_{\text{AP-DAP}}$ for each cell with a DAP in the STA_V. The symbol indicates the cell type (star: stellate cell, triangle: pyramidal cell, circle: cell type not identified), whether the cell exhibited large theta oscillations (vertically striped) and whether the cell had a DAP detectable in the STA_V (horizontally striped).

Why are there so few cells with a DAP?

From *in vitro* recordings we know that around 85% of stellate and 73% of pyramidal cells in the MEC layer II have a DAP (Canto and Witter, 2012). However, by means of the STA_V we found that only 5 of 26 (around 20%) of cells *in vivo* had a DAP regardless of the cell type. Why was the percentage so much lower?

One reason might be that the DAP is suppressed by synaptic input. Another reason could be that the quality of the recording was lower, as recording *in vivo* is more difficult than *in vitro*. Especially the series resistance, i.e. the sum of the pipette resistance and the resistance at the pipette-cell junction, was found to be increased *in vivo* (Wang et al., 2016; Margrie et al., 2002). The series resistance together with the pipette capacitance act as a low pass filter on the voltage signal. An increased series resistance leads to a decrease in the passband of the filter which causes, for instance, APs to be smaller and wider.

To test whether the quality of the recording had an influence on the after-spike dynamics we recomputed the STA_V using only APs that came from a presumably good part of the recording. As both AP width and amplitude are affected by the quality of the recording, they were used to decide whether an AP was accepted or not. The AP width and amplitude were computed from the STA_V for each cell whereby the membrane potential 5 ms before the AP peak was used as a reference value for the AP amplitude (Fig. 2.15).
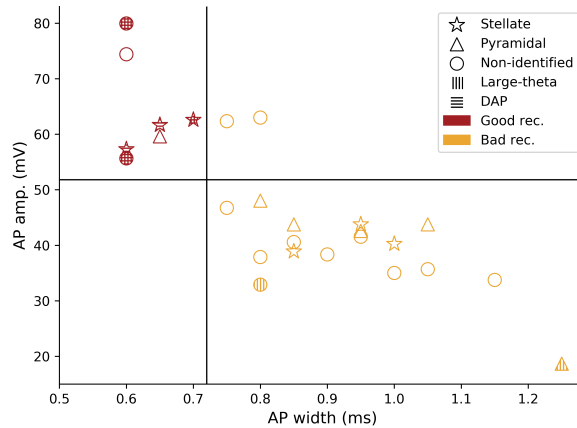
Fig. 2.15: Recognition of good recordings by means of AP amplitude and width computed from the STA_V. Division into good (red symbols) and bad recordings (yellow symbols) by taking the middle between the outermost cell with a DAP (horizontally striped symbols) and the closest cell without DAP for AP width (vertical line at 0.72 ms) and amplitude (horizontal line at 51.8 mV) respectively. The symbol indicates the cell type (star: stellate cell, triangle: pyramidal cell, circle: cell type not identified), whether the cell exhibited large theta oscillations (vertically striped) and whether the cell had a DAP detectable in the STA_V (horizontally striped) or in the STA_V from selected APs (diagonally striped).

All cells that showed a DAP had low AP widths and high AP amplitudes. But, there were also two cells without a DAP that were in the same area. Cell s74_0006 likely had no DAP as will be affirmed below. For cell s82_0002 we suppose that the DAP was suppressed by synaptic input as the cell had the highest firing rate of all bursty cells.

The decision threshold for AP width and amplitude was set to the middle between the outermost cell with a DAP and the closest cell without a DAP, respectively. This means that an AP was accepted if its AP width was smaller than 0.72 ms and its AP amplitude larger than 51.8 mV. These thresholds were only approximate as there are variations in AP width and amplitude between cells. Nevertheless, they can serve to test whether after-spike dynamics become more visible when only presumably well-recorded APs are used for the STA_V.

In Fig. 2.16 the STA_V without and with selection of APs can be seen. A DAP became visible in cell s73_0004 and also a very small DAP in cell s85_0007. In both cases the DAP deflection was larger than the SEM of the voltage at the DAP maximum. For 10 cells no APs meeting the criteria were found. In total 7 out of 16 cells (around 44%) were classified to have a DAP. This is closer to what was measured *in vitro* but still a lower bound estimate.

For most cells it is easier to spot the difference in the after-spike dynamics in the derivative of the STA_V (Fig. 2.17). In particular, the global maximum in the derivative of the STA_V within 3.5 ms after the AP peak will be used to quantify how pronounced a DAP of a cell is for the following reasoning. Case 1: If there is a DAP in the STA_V, the derivative of the STA_V should cross zero at the time point of the fAHP minimum and the DAP maximum. In between the fAHP minimum and the DAP maximum there is an inflection point in the STA_V that is reflected
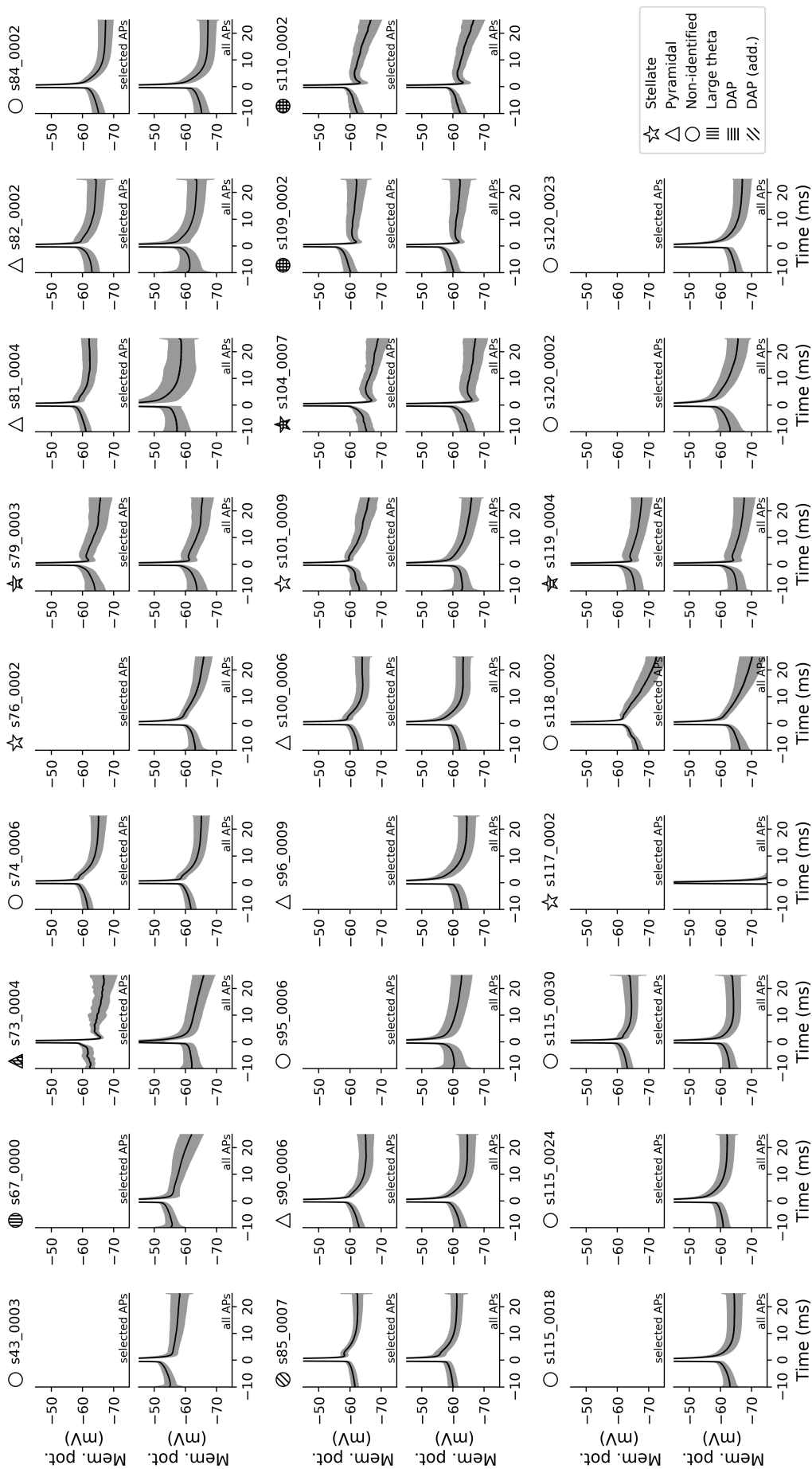
Fig. 2.16: Selection of APs from a presumably good part of the recording by means of AP width (< 0.72 ms) and amplitude (> 51.8 mV). The upper plot shows the STA_V from selected APs. For comparison the lower plot shows the STA_V from all APs in the recording. For each cell the symbol indicates the cell type (star: stellate cell, triangle: pyramidal cell, circle: cell type not identified), whether the cell exhibited large theta oscillations (vertically striped) and whether the cell had a DAP detectable in the STA_V (horizontally striped) or in the STA_V from selected APs (diagonally striped).

Fig. 2.17: Derivative of the STA$_V$ shown in Fig. 2.16. The number in the upper right is the absolute difference of the maximum within 0 to 3.5 ms between selected and all APs. It is positive if the maximum was higher for the selected APs. For each cell the symbol indicates the cell type (star: stellate cell, triangle: pyramidal cell, circle: cell type not identified), whether the cell exhibited large theta oscillations (vertically striped) and whether the cell had a DAP detectable in the STA$_V$ (horizontally striped) or in the STA$_V$ from selected APs (diagonally striped).
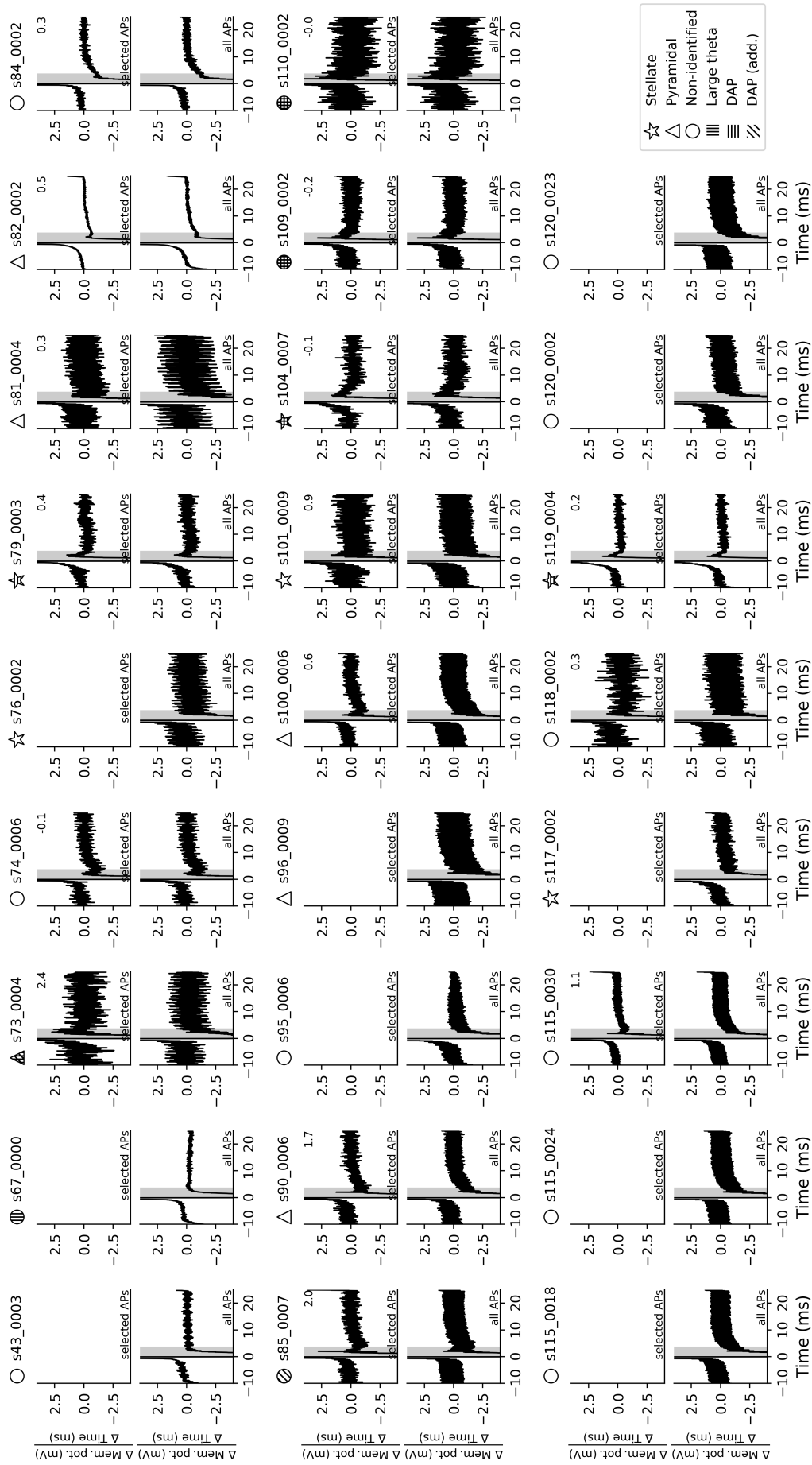
in a local maximum in the derivative of the STA_V. Case 2: If in the STA_V of a cell an inflection point but no DAP is present, there will still be a local maximum in the derivative, but it will be below zero. Case 3: If the STA_V of a cell only declines after the AP peak without change of curvature, there will be no local maximum and the global maximum will be the latest point within the given range. The range was chosen short enough such that the maximum in the case of an inflection point (case 1 and 2) was more prominent than the maximum of a noisy voltage trace of case 3. Therefore, the global maximum in the derivative of the STA_V will be higher the more pronounced the DAP of a cell is. The difference between the maximum in the STA_V from selected and all APs is used as a measure of the improvement in DAP recognizability (upper right value in Fig. 2.17).

For all but four cells the global maximum within 3.5 ms from the AP peak increased when selecting for presumably well-recorded APs. Cell s104_0007, s109_0002 and s110_0002 already had a prominent DAP and therefore did not increase. For cell s74_0006 it was assumed that it had no DAP which was affirmed by the slight decrease in the maximum. The cell with the highest increase, s73_0004, showed a prominent DAP in the STA_V with selection but not in the STA_V without confirming the validity of the quantification.

In Fig. 2.18 the DAP deflection and $Time_{AP\text{-}DAP}$ computed from the STA_V with selection is shown for all cells with a DAP. Both, DAP deflection and $Time_{AP\text{-}DAP}$, increased or stayed the same compared to the values without selection for all cells. Cell s73_0004, as the other large theta cells, also had a high DAP deflection and $Time_{AP\text{-}DAP}$. Cell s85_0007 had very small values for both characteristics.

The influence of the quality of the recording on the visibility of DAPs suggests that better recordings are needed to make reliable statements as to whether a cell has a DAP.

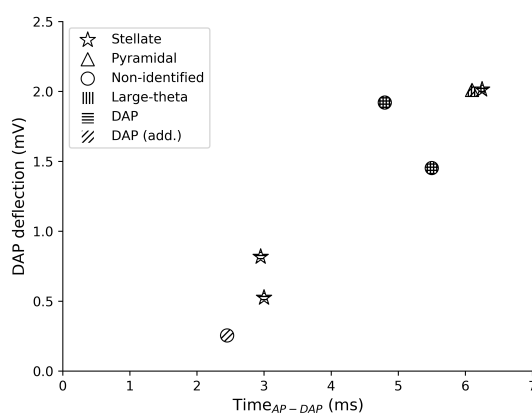**Fig. 2.18:** DAP deflection as a function of $Time_{AP\text{-}DAP}$. The symbol indicates the cell type (star: stellate cell, triangle: pyramidal cell, circle: cell type not identified), whether the cell exhibited large theta oscillations (vertically striped) and whether the cell had a DAP detectable in the STA_V (horizontally striped) or in the STA_V from selected APs (diagonally striped).

2.2.2 DAP function: Burst firing

In Fig. 1.6 it was shown that the DAP reduces the current threshold for eliciting an AP during the DAP and therewith facilitates burst firing. In the following, it was investigated whether cells with a DAP *in vivo* are more likely to fire bursts than cells without.

Cells were first classified into bursty and non-bursty based on the spike-time autocorrelation. The classification was confirmed by testing the consistency with other characterizations of the firing behavior. In the end, the classification was used to study the relationship between DAPs and burst firing.

Classification into bursty and non-bursty

To investigate whether cells with a DAP are more likely to fire bursts, we classified all cells into bursty and non-bursty following the example of Latuske et al. (2015) with adjusted settings (Sec. 4.4.9). To quantify the firing behavior, the spike-time autocorrelation was computed up to 50 ms. Then, a principal component analysis (PCA) was performed on the spike-time autocorrelation from all cells to identify the directions of highest variance. The first two principal components were used for the classification. A k-means cluster algorithm was applied to split cells into bursty and non-bursty.

The outcome of the classification is shown in Fig. 2.19 (see Fig. 2.20 for the spike-time autocorrelations of all cells and Suppl. Fig. 5.10 for the principal components). Bursty and non-bursty cells could be split perfectly along the first principal component (PC1). The cells with the lowest PC1 values had a higher spike-time autocorrelation for long time lags, whereas cell s118_0002
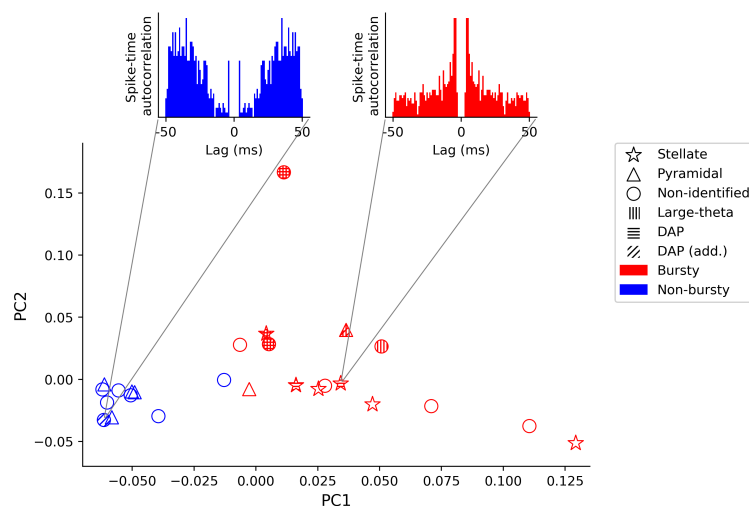
Fig. 2.19: Division of grid cells into bursty (red) and non-bursty (blue) based on the dimensionality reduced spike-time autocorrelation. The axes are the first two principal components obtained by PCA. The symbol indicates the cell type (star: stellate cell, triangle: pyramidal cell, circle: cell type not identified), whether the cell exhibited large theta oscillations (vertically striped) and whether the cell had a DAP detectable in the STA_V (horizontally striped) or in the STA_V from selected APs (diagonally striped).

Fig. 2.20: Spike-time autocorrelation for all grid cells. For each cell the symbol indicates the cell type (star: stellate cell, triangle: pyramidal cell, circle: cell type not identified), whether the cell exhibited large theta oscillations (vertically striped) and whether the cell had a DAP detectable in the STA_V (horizontally striped) or in the STA_V from selected APs (diagonally striped).
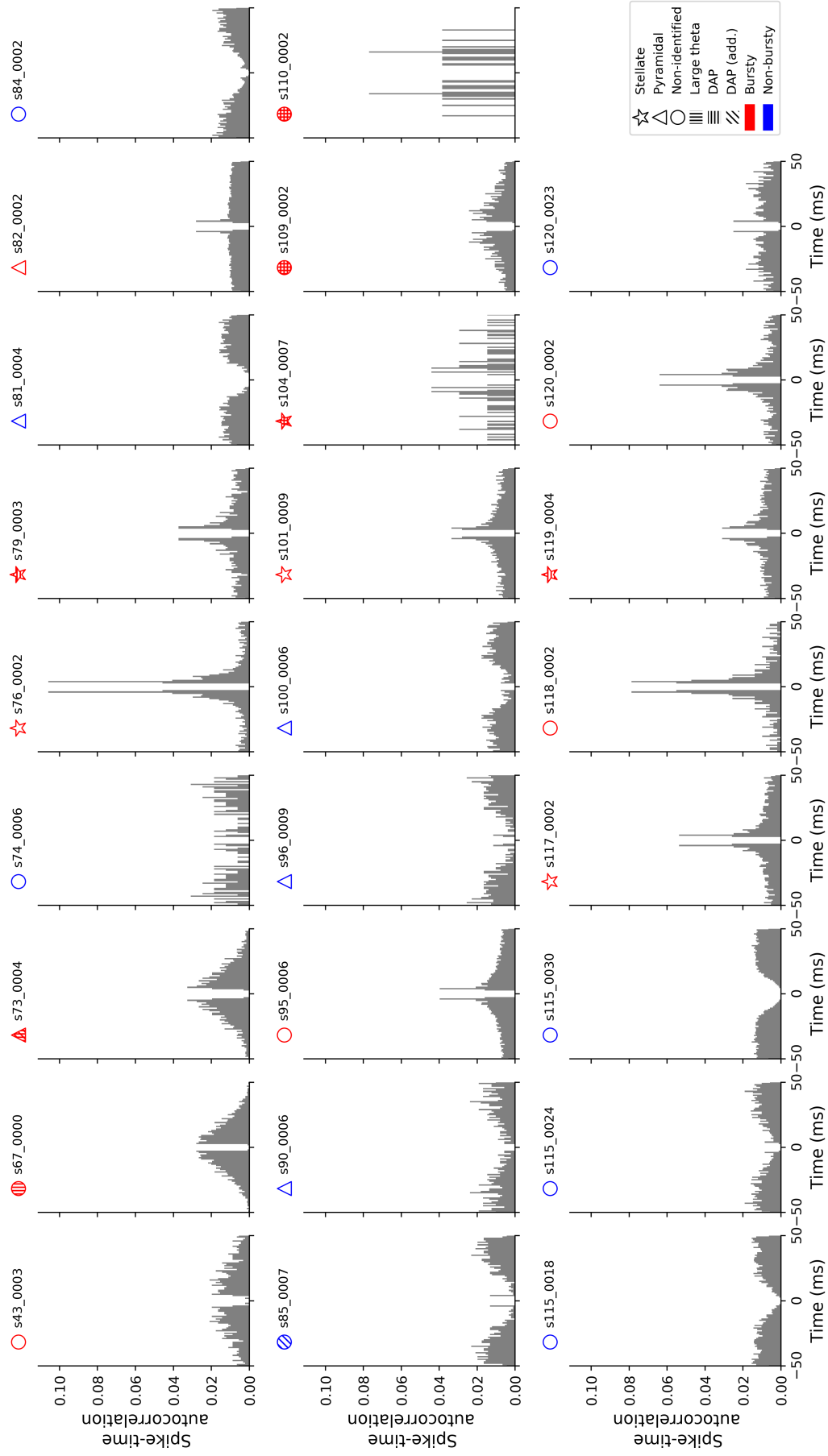
and s76_0002, that had the highest PC1 values, exhibited high peaks for short time lags (≤ 8 ms). Cell s120_0023 that marked the border between bursty and non-bursty cells also showed an intermediate spike-time autocorrelation, but was non-bursty as confirmed later. Thus, the burstiness of a cell was well represented by the PC1.

There were also two cells that stood out from the others. Cell s110_0002, that had the highest second principal component (PC2), was an outlier because it only had few spikes. Cell s82_0002 was considered bursty due to the peak at a short time lag, but it was the only cell with this shape of spike-time autocorrelation. It may had stronger synaptic input, so that the average firing rate was increased.

All stellate cells were labeled bursty. This deviates from the findings of Latuske et al. (2015) who reported that 73% of putative calbindin$^-$ cells (presumable stellate cells) were bursty. The disagreement likely arose from the small sample size (n=6) in the data set by Domnisoru et al. (2013). Additionally, the cell type classification methods, based on morphology (Domnisoru et al., 2013) versus indirect immunohistochemistry following the method by Tang et al. (2014) (Latuske et al., 2015), might have made a difference. Of the pyramidal cells from MEC layer II around 67% were bursty. Given the small sample size (n=3), this is consistent with the 63% of putative calbindin$^+$ cells (presumable pyramidal cells) found by Latuske et al. (2015).

Consistency of the classification with other characterizations of the firing behavior

To investigate the firing behavior of bursty and non-bursty cells in more detail for each cell an ISI histogram, the frequency of spike events and an ISI return map were computed.

An ISI histogram is a specialization of the spike-time autocorrelation. The spike-time autocorrelation is based on the time intervals between all pairs of spikes, whereas the ISI histogram is based only on the time intervals between successive spikes. For short spike intervals the ISI histogram and the spike-time autocorrelation are nearly identical. Hence, it was expected that the classification into bursty and non-bursty is clearly visible for short ISIs. In particular, the fraction of ISIs ≤ 8 ms from all ISIs was compared between bursty and non-bursty cells (Fig. 2.21 A). Both groups did not overlap and the difference was highly significant (t-test: $p < 0.0001$). In the cumulative ISI histogram (Fig. 2.22, for each cell see Fig. 2.23) it can be seen that bursty cells had the highest slope at about 4 ms. Then, the slope decreased to zero, crossing around 30 ms the value 1/200, i.e. the slope corresponding to a uniform ISI distribution. Large-theta cells, part of the bursty cells, showed a renewed increase in the slope at 120 ms (~8 Hz). For non-bursty cells the slope was low for short ISIs, rose until around 30 ms and then declined to zero.

The frequency of spike events depicts how many spike sequences (where ISIs were ≤ 8 ms) with a certain number of spikes occurred. It is useful to determine
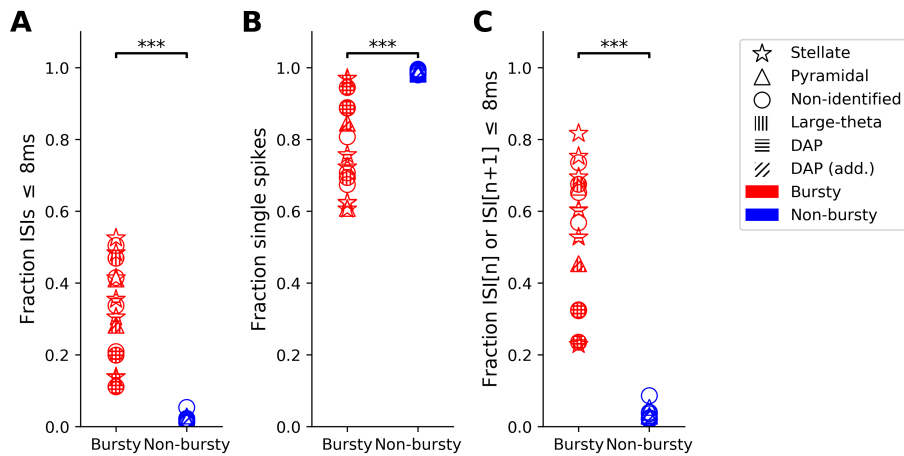
Fig. 2.21: Bursty (red) and non-bursty cells (blue) are significantly different (t-test with p-val. $< 0.01, 0.001, 0.0001 = *, **, ***$) for the following measures. A: The fraction of ISIs ≤ 8 ms from all ISIs. B: The fraction of single spike from all spike events. C: The fraction of ISI[n], ISI[n+1] pairs where ISI[n] or ISI[n+1] is ≤ 8 ms from all pairs. The symbol indicates the cell type (star: stellate cell, triangle: pyramidal cell, circle: cell type not identified), whether the cell exhibited large theta oscillations (vertically striped) and whether the cell had a DAP detectable in the STA_V (horizontally striped) or in the STA_V from selected APs (diagonally striped).

Fig. 2.22: Cumulative ISI histogram for all grid cells. The cells were classified into bursty (red) and non-bursty (blue) according to Fig. 2.19. The thick lines are the cumulative ISI histograms for ISIs from all bursty and non-bursty cells respectively. ISIs longer than 200 ms were taken out as those time scales are irrelevant for distinguishing burst and non-burst behavior.
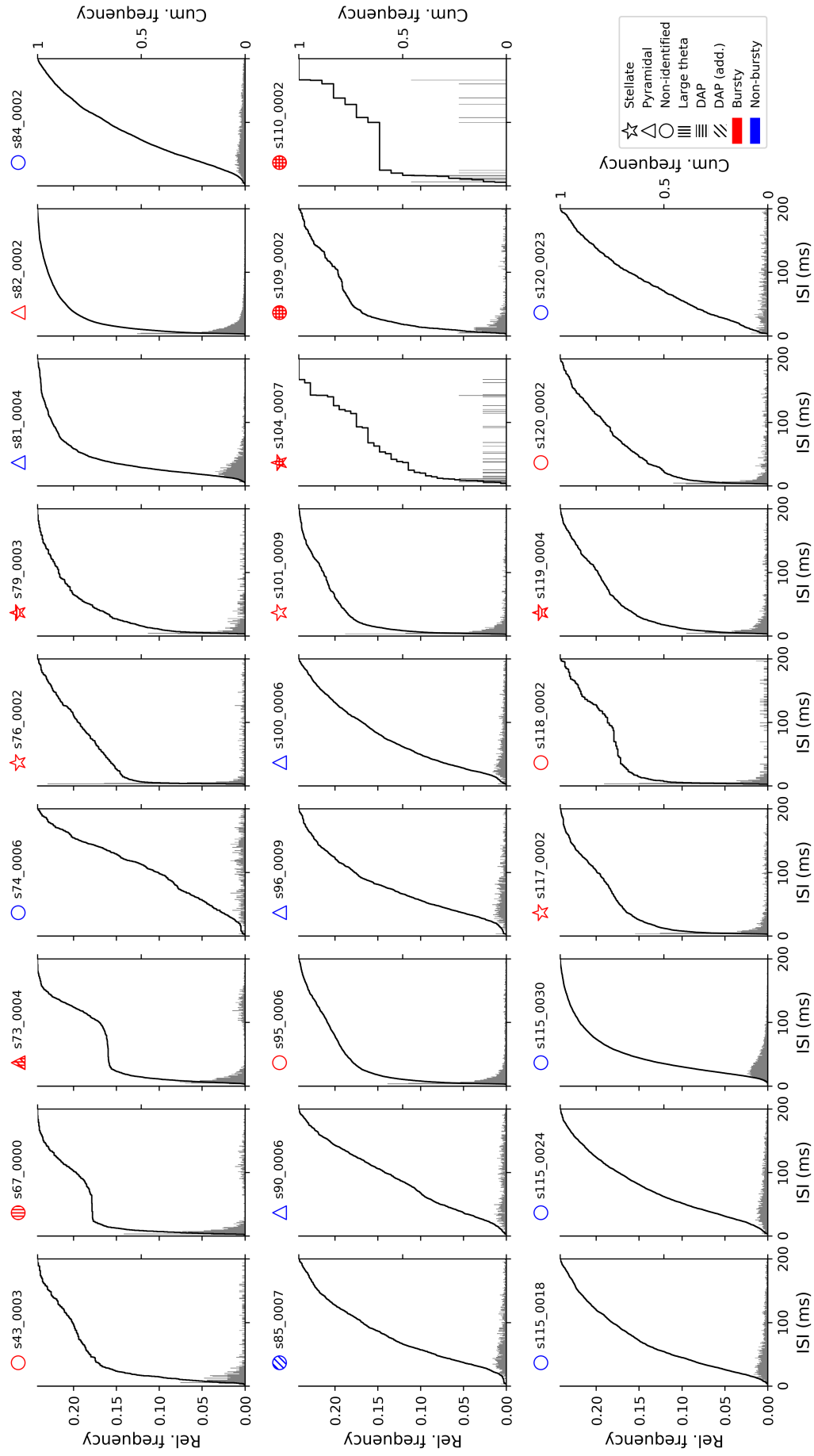
Fig. 2.23: ISI histogram and cumulative ISI histogram for all grid cells for ISIs $\leq$ 200 ms. For each cell the symbol indicates the cell type (star: stellate cell, triangle: pyramidal cell, circle: cell type not identified), whether the cell exhibited large theta oscillations (vertically striped) and whether the cell had a DAP detectable in the STA_V (horizontally striped) or in the STA_V from selected APs (diagonally striped).
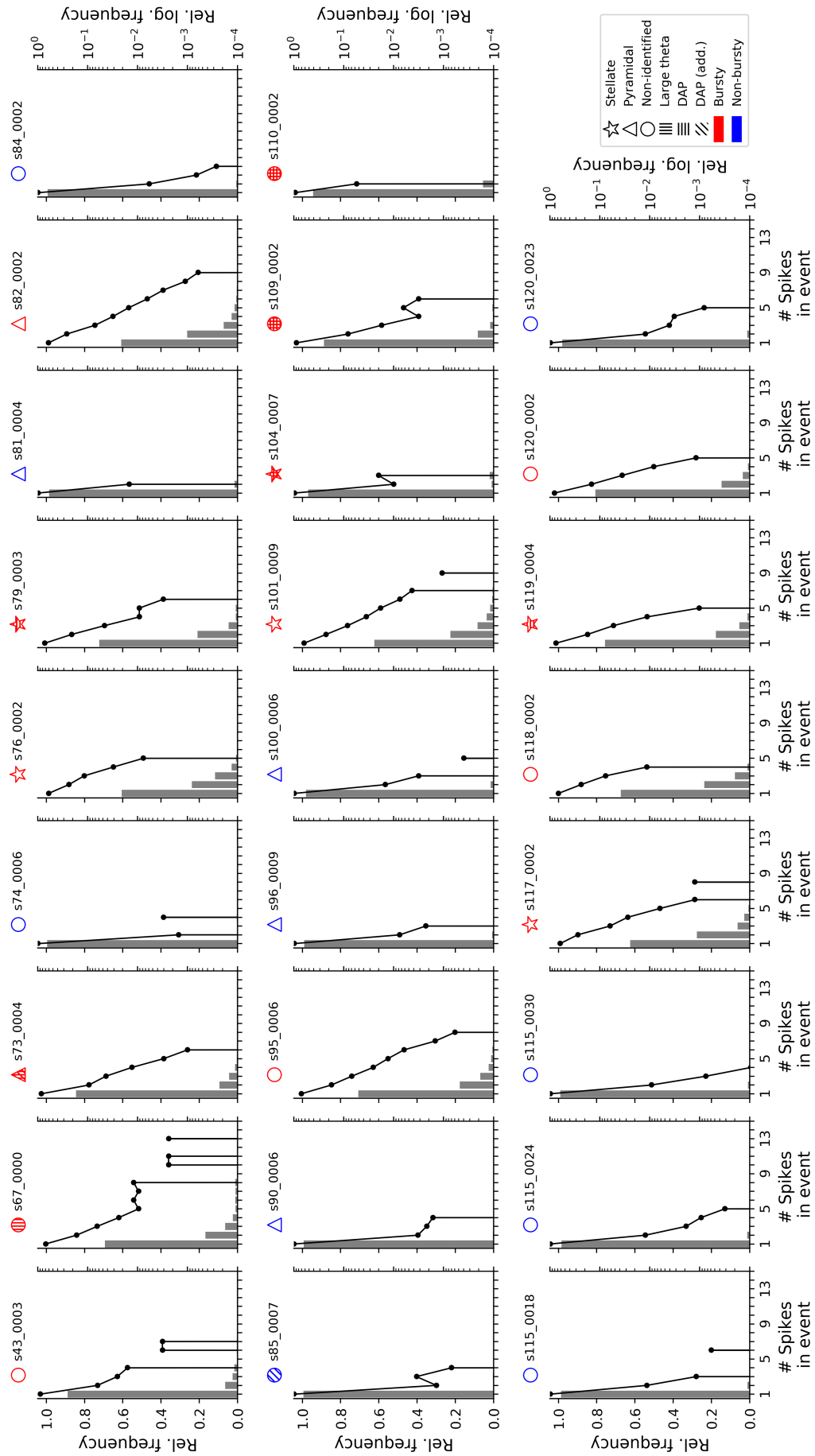
Fig. 2.24: Relative frequency of spike events with a certain number of spikes (1: single spikes, ≥1: bursts) for all grid cells on a linear (histogram) and logarithmic (line with dots) scale. For each cell the symbol indicates the cell type (star: stellate cell, triangle: pyramidal cell, circle: cell type not identified), whether the cell exhibited large theta oscillations (vertically striped) and whether the cell had a DAP detectable in the STA_V (horizontally striped) or in the STA_V from selected APs (diagonally striped).
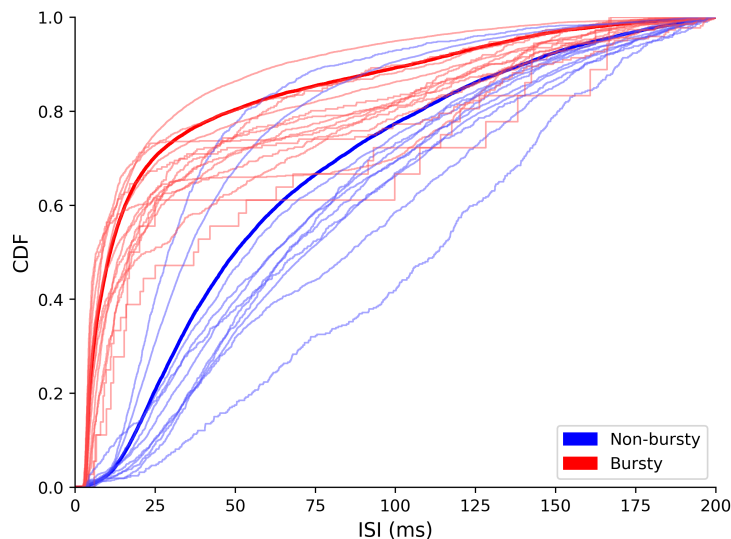
Fig. 2.25: ISI return maps for all grid cells. For each cell the symbol indicates the cell type (star: stellate cell, triangle: pyramidal cell, circle: cell type not identified), whether the cell exhibited large theta oscillations (vertically striped) and whether the cell had a DAP detectable in the STA_V (horizontally striped) or in the STA_V from selected APs (diagonally striped).
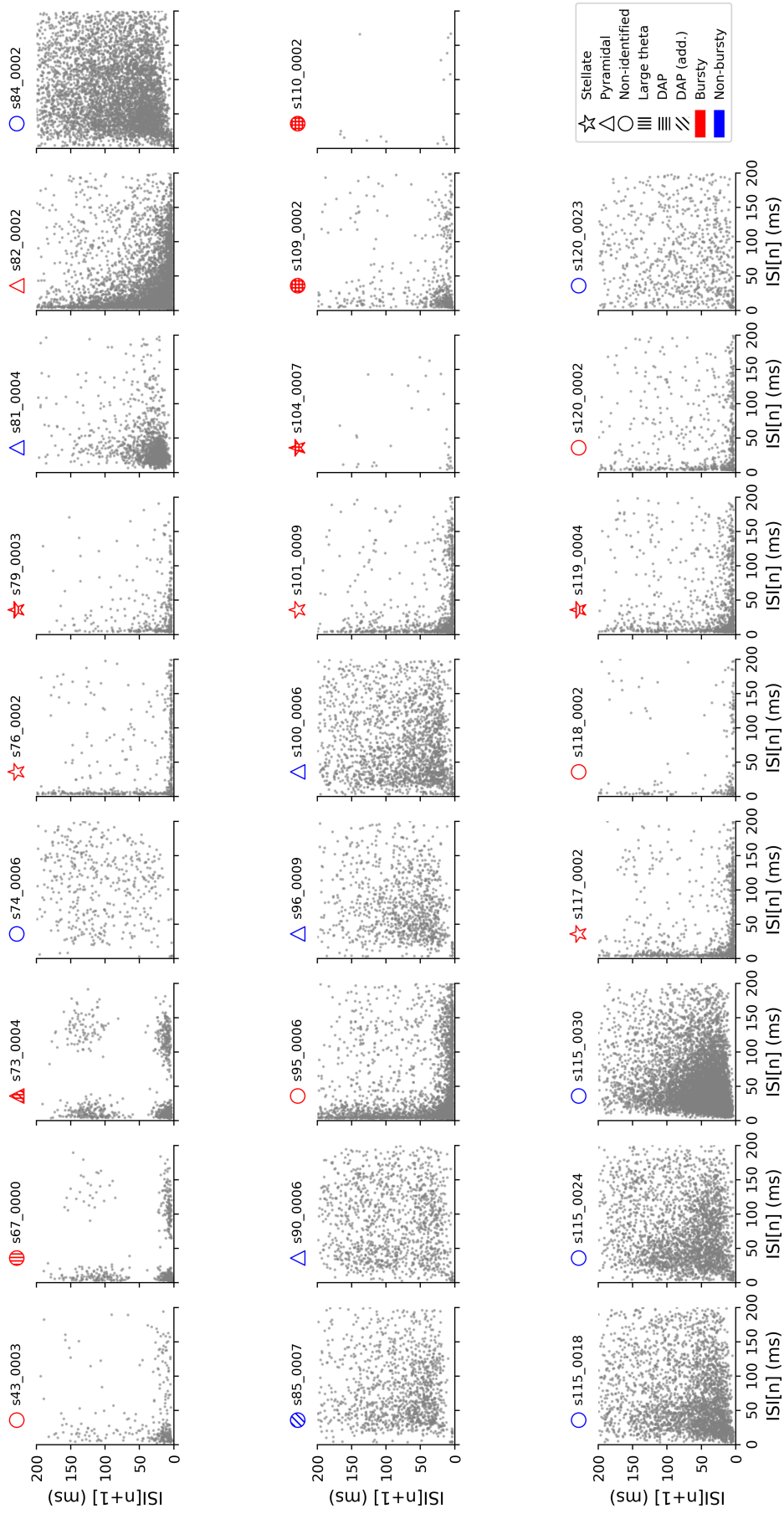
which kind of burst (doublet, triplet, etc.) bursty and non-bursty cells exhibited. Furthermore, it was used to ascertain that bursty cells had a higher proportion of burst events than non-bursty cells and not only a higher number of spikes per burst. In Fig. 2.24 the frequency of spike events for all cells is shown. Bursty cells had spike events with up to six spikes per event and higher. There was an approximately exponential decay in the number of spikes per event until it dropped to zero. Non-bursty cells, on the other hand, had a high number of single spikes and few doublets or triplets. Cell s104_0007 and s110_0002 did not follow the rule as they were bursty but mainly had single spikes. The reason might be that they had too little synaptic input leading to a low average firing rate and less spikes per event. To quantify the difference between bursty and non-bursty cells the fraction of single spikes with respect to all spike events was computed (Fig. 2.21 B). Non-bursty cells had a fraction of single spikes close to 1.0, whereas bursty cells had lower values spread between 0.5 and 1.0. Bursty cells were significantly different (t-test: $p < 0.0001$) from non-bursty cells.

ISI return maps show the relationship between successive ISIs (Fig. 2.25). They are useful to detect patterns in the firing behavior. Bursty cells had many points close to the edges which means that burst-like ISIs (~3-15 ms) were followed by an ISI of any length and that longer ISIs were succeeded by burst-like behavior. Furthermore, there was a high density of points in the lower left corner showing that the cell often stayed inside the burst. Non-bursty cells only infrequently showed points at the edges as they rarely fired bursts. In three of the large-theta cells (s67_0000, s73_0004, s109_0002) spike firing was affected by the theta oscillations as points aggregated around ISIs of 120 ms (~8 Hz). For cell s104_0007 and s110_0002 there were too few points to determine whether they fired at theta frequencies. The difference between the ISI return maps of bursty versus non-bursty cells was quantified by estimating the number of ISIs that fall within the region close to the edges, i.e. when ISI[n] or ISI[n+1] $\leq$ 8 ms with respect to all ISI[n], ISI[n+1] pairs (Fig. 2.21 C). Non-bursty cells had a low fraction of pairs where ISI[n] or ISI[n+1] was $\leq$ 8 ms compared to bursty cells. The difference was highly significant (t-test: $p < 0.0001$).

Relationship of DAPs and burst firing
Having the classification into bursty and non-bursty cells confirmed, the relationship between DAPs and burst firing can be elucidated.

All cells with a DAP besides one were classified as bursty supporting the hypothesis that the DAP enhances burst firing (Fig. 2.19). Cell s85_0007 might be non-bursty because the DAP was too small. Furthermore, burst timing coincided with the time of the DAP maximum (besides for cell s85_0007) consistent with the idea that the subsequent spike is fired on the DAP (Fig. 2.26).

To investigate the other direction, whether being classified as a bursty cell involves having a DAP, we took the mean of the STA_V with selection over all bursty and non-bursty cells, respectively. The mean STA_V of bursty cells showed

a clear DAP, whereas the mean STA_V of non-bursty cells only had an inflection point (Fig. 2.27).

These analyses provide evidence towards a relationship between the DAP and burst firing *in vivo*, but higher sampling sizes and high quality recordings are needed to confirm these results.
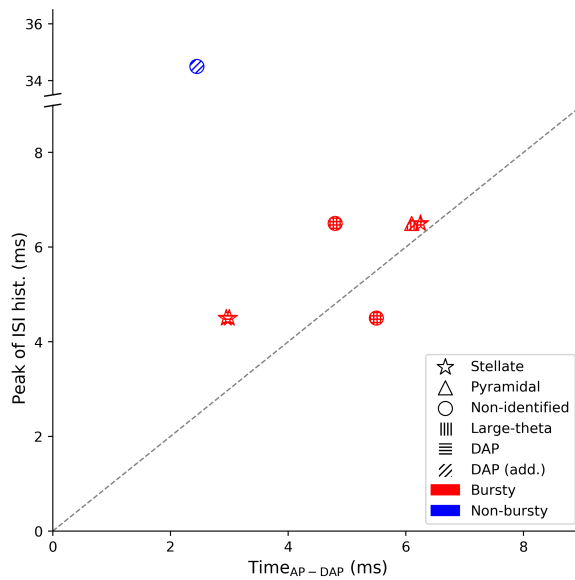
Fig. 2.26: Peak of the ISI histogram (1 ms bins) as a function of $Time_{AP\text{-}DAP}$. The dashed line marks the identity. The symbol indicates the cell type (star: stellate cell, triangle: pyramidal cell, circle: cell type not identified), whether the cell exhibited large theta oscillations (vertically striped) and whether the cell had a DAP detectable in the STA_V (horizontally striped) or in the STA_V from selected APs (diagonally striped).
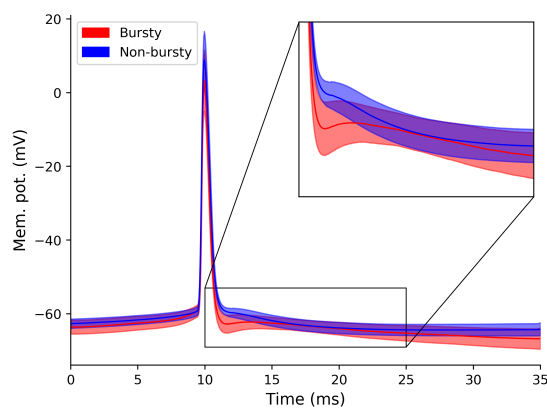
Fig. 2.27: Mean and standard deviation of the STA_V of selected APs over all bursty (red) and non-bursty (blue) cells.

Discussion

<div style="text-align: right; font-size: 2em;">3</div>

In this work we analyzed the phenomenon of the depolarizing afterpotential (DAP) by creating a biophysically realistic cell model and investigated the relationship between DAPs and burst firing *in vivo*.

For the first part, we created a single-compartment model of a typical stellate cell in the MEC layer II that reproduced the main electrophysiological characteristics (DAP, sag, tonic firing and resonance). The mechanism behind the DAP was analyzed using virtual voltage clamp and blocking experiments. In the model a Na_P channel, K_{DR} channel and a leak current were necessary to generate a DAP whereby the Na_P current also exhibited a resurgent component. This suggests that for the generation of a DAP a balance between several currents is needed. In addition, the persistent and resurgent sodium current might play an important role. The effect of model parameters on the DAP shape was examined with a sensitivity analysis. $V_{s,m/h}$ of the Na_T, Na_P, K_{DR} channel and $\tau_{max,m/h}$ of the Na_P channel had significant correlations with DAP characteristics.

For the second part, we tested whether DAPs occur *in vivo*. We found that around 20% of grid cells in the data set from Domnisoru et al. (2013) exhibited a DAP. However, the percentage of cells was much lower than *in vitro*. We showed that this is partly due to the quality of the recording, as selecting APs from presumably good parts of the recording improved the visibility of DAPs. To investigate the relationship between DAPs and burst firing all cells were classified into bursty and non-bursty based on the spike-time autocorrelation. All cells with a DAP were bursty besides the cell with the smallest DAP. Moreover, averaging over the STA_V of all bursty and non-bursty cells respectively, showed a clear DAP for the bursty but not for the non-bursty cells.

3.1 Reproduction of the DAP and other stellate cell characteristics

3.1.1 Model design

The stellate cell model we wanted to create should be simple and easy to understand. Therefore, we chose a single-compartment model. Literature research on ion channels in MEC layer II stellate cells showed that data on ion channels was sparse. Furthermore, existing ion channel models were not able to fit the DAP. This is elaborated in the next two paragraphs.

Sparse experimental data

One reason why we did not use experimental data to model ion channels was that usually not all parameters of an ion channel are estimated. For instance,

Magistretti and Alonso (1999) recorded sodium channels in stellate cells of the MEC layer II but did not measure the time constant for the activation and inactivation of the Na_T channel. Furthermore, the recordings were not corrected for the liquid junction potential, so that for example the half-activation of the steady state curve could be shifted by tens of millivolts. There was also variation between different recordings. For instance, the half-activation values of the steady state inactivation curve of the Na_T channel differed by 9.2 mV between the measurements of Magistretti and Alonso (1999) and Hargus et al. (2011).

Existing ion channel models

To check out existing ion channel models, we searched on ModelDB (`https://senselab.med.yale.edu/modeldb/`), a widely used platform for making computational neuroscience models accessible. When looking for the keyword "Entorhinal cortex stellate cell" and the simulation environment NEURON, three entries showed up: i) (Schmidt-Hieber and Häusser, 2013) (ModelDB 150239) ii) (Justus et al., 2017) (ModelDB 222359) and iii) (Schmidt-Hieber, Toleikyte, et al., 2017) (ModelDB 237326). The ion channel models in those three entries were mostly derived from recordings from different brain areas and cell types. For instance, K_{DR} and K_{AP} were based on recordings from CA1 pyramidal cells.

Furthermore, it can be shown that fitting the DAP is not possible with these ion channels using a linear regression method developed by Huys et al. (2006) (Fig. 3.1).

The unavailability of complete information on the kinetics of ion channels in MEC layer II stellate cells and the impossibility to fit the DAP with existing ion channel models led to the conclusion that the ion channel kinetics should be determined by the optimization algorithm. To keep the model simple only four different types of ion channels were included in the model. They were chosen to test different hypotheses of DAP generation and every channel was known to be present in MEC layer II stellate cells (for details see Sec. 4.1).

3.1.2 Quality of the model

In Sec. 2.1.1 it was shown how well the model reproduces stellate cell characteristics. This was evaluated qualitatively by comparing the behavior of the real and simulated cell and quantitatively by testing how well the model lies within the distribution of the $MECII_{DAP}$ population.

The model was able to reproduce all characteristics qualitatively as it showed a DAP, reduction in current threshold during the DAP, a sag, tonic firing in response to positive step currents, resonance and theta modulated spike firing in the double-sine experiment. But, for some experiments it deviated from the range exhibited by experimentally measured cells.

$Time_{AP-DAP}$ of the model was at the higher end of the distribution of $MECII_{DAP}$ cells which likely caused the current threshold curve to be shifted to the right.
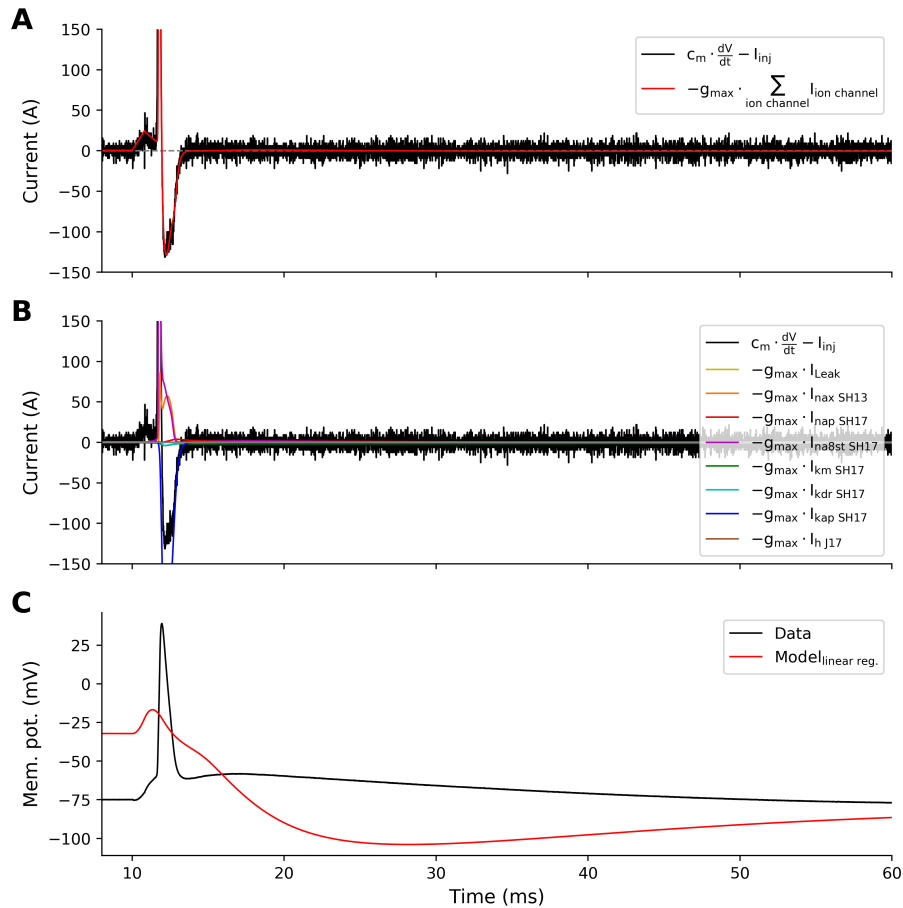
Fig. 3.1: The DAP could not be fit by existing ion channel models. In the method by Huys et al. (2006) the maximal conductance g_{max} of each ion channel is determined by linear regression so that $c_m \frac{dV}{dt} - I_{inj} = -g_{max} \sum_{ion\ channel} I_{ion\ channel}$ whereby $\frac{dV}{dt}$ is the numerical derivative of the recorded voltage trace (black line in C) and $I_{ion\ channel}$ is the current trace obtained by simulating each ion channel given the recorded voltage trace. A: Linear combination of the current traces with maximal conductances set to the best fit (red line) and the trace that should be fit $c_m \frac{dV}{dt} - I_{inj}$ (black line). The gray dashed line marks zero current. B: Current traces of all ion channels used for the fit (colored lines). C: Comparison of the recorded voltage trace (black line) and the fit model (red line). The deviation is stronger than seen in A, because here the ion channels are simulated with the model voltage and not given the recorded voltage trace.

Furthermore, the sag deflection was at the lower range of the MECII$_{DAP}$ population. The F-I curve had a stronger kink, was steeper (high value for a) and ascended more linearly (high value for c) than for most MECII$_{DAP}$ cells.

That the model was unable to fit those characteristics closer to the experimental data, might be, because the model was too inflexible or not complex enough. For instance, the parameter V_s controls both the steady state and time constant equation and thus has to be a trade-off between the two. Furthermore, the Hodgkin-Huxley formalism might be insufficient to model, for example, the resurgent sodium current, so that more complex models as Markov models might be needed. In addition, it cannot be excluded that better models exist in the parameter space that the optimization algorithm did not find. But, as other

48

models found (Sup. 5.1) show similar limitations, new strategies should be tried.

Existing models of stellate cells

Previous models on stellate cells of the MEC layer II concentrate mostly on resonance, sag and subthreshold oscillations leading to spike clustering (Erchova et al., 2004; Fransén et al., 2004; Rotstein et al., 2006; Izhikevich, 2007) or the rebound phenomenon (Hasselmo, 2014; Ferrante et al., 2016). Furthermore, biophysical stellate cell models have been used to explain grid cell firing (Schmidt-Hieber and Häusser, 2013; Schmidt-Hieber, Toleikyte, et al., 2017). However, to our knowledge no model exists so far that reproduces the DAP. Generally, there is no model that reproduces all typical stellate cell characteristics. As the model presented here was thoroughly tested on a diverse set of stimuli and compared to experimentally recorded cells, it could be used as a benchmark case for stellate cell models to come.

3.2 The mechanism behind the DAP

3.2.1 Identifying ion channels in the model

As the ion channels in the model were almost completely determined by the optimization algorithm, the correspondence to real ion channels had to be established. By parameter comparison and voltage clamp experiments it was shown, that the ion channels were similar to experimentally measured ion channels.

The Na_P channel deviated from recorded ion channels as it had a much lower value for $V_{h,h}$ and showed both persistent and resurgent components in the voltage clamp experiment. This suggests that either the Na_P channel in the model was not complex enough to faithfully reproduce both, the persistent and resurgent component, or a further ion channel is needed to fit the resurgent sodium current. In any case, further experiments should be conducted to disentangle the ion channel subtypes responsible for the persistent and resurgent component in real cells.

The parameter V_s was generally higher in the model compared to the experimental recordings. This might be due to the use in the steady state and time constant equation. In the future, different equations for the time constant should be tested that do not depend on V_s.

3.2.2 Virtual blocking of ion channels

Blocking ion channels in the model showed that only three ion channels were necessary for DAP generation: the Na_P channel, the K_{DR} channel and the leak current. The DAP was reduced when the Na_T channel was blocked. Blocking the HCN channel had almost no effect on the DAP.

These results are consistent with blocking experiments in real cells. Alessi et al. (2016)) showed that the DAP is reduced by blocking with TTX or AEA. As

TTX blocks several subtypes of sodium channels, it can only be derived from the experiments that some sodium channel was involved. The reduction by the more selective blocker AEA, on the other hand, indicated a role for the Na_P and Na_R channel. This accords with the necessity of the Na_P channel in our model.

Alessi et al. (2016) also discovered an influence of extracellular calcium removal on the DAP that depended on hyperpolarization. As no calcium currents were present in the model, this could not be shown. However, the effect of calcium channels could be similar to Na_P channels as suggested by hypothesis 2 of DAP generation.

Hönigsperger et al. (2017) showed that the DAP depends on Kv2 channels that are known to underlie K_{DR} currents. This accords with the fact that the K_{DR} channel was necessary in the model to elicit a DAP.

The DAP amplitude was also shown to be significantly increased by blocking the M(Kv7) current with linopirdine (Yoshida and Alonso, 2007). As Kv7 channels were not included in the model, it cannot reproduce the effect. We suggest that, similar to the Na_T channel, Kv7 channels are not essential for DAP generation, but by removing potassium outflow the membrane potential is increased.

3.3 The effect of model parameters on DAP characteristics

Before analyzing the correlations between model parameters and DAP characteristics we ensured that the data set was large enough to obtain reliable correlations. Then, the significance of the correlations over the whole data set was determined. There were significant correlations between $V_{s,m/h}$ of the Na_T, Na_P, K_{DR} channel and $\tau_{max,m/h}$ of the Na_P channel. However, even the strongest correlation amounted only to -0.3 suggesting that it is difficult to shape the DAP by only one parameter. Note also that even though the models were filtered for showing a reasonable AP and DAP, they could fail to reproduce other stellate cell characteristics. Nevertheless, these findings provide a starting point for fitting differently shaped DAPs and hint towards causes for the variations in the DAP shape of MEC layer II cells.

3.4 Future directions of the stellate cell model

There are at least three different possibilities to continue research with the model. The first possibility is the further improvement of the model with the suggestions made above. That are: i) Using a different equation for the time constant where the parameters are independent from the steady state curve; ii) Markov models for (some of) the ion channels; iii) adding a separate Na_R channel; iv) fitting real cells with differently shaped DAPs guided by the results from the sensitivity analysis.

The second possibility is to test predictions of the model experimentally. This would provide further evidence for or against the model and more information

could be gained on MEC layer II stellate cells. For instance, in a dynamic clamp setup specific ion currents could be removed by pharmacological blockers and replaced by ion channels from the model while recording the membrane potential (for examples see Ma and Koester, 1996; Hutcheon et al., 1996). If the membrane potential is similar, when recorded with or without the replacement of the real ionic currents by model currents, it can be concluded that the ion channels in the model are equivalent to the real ion channels for the range tested. Another example concerns bistability in MEC layer II stellate cells. In the model, we observed a kink at the start of the F-I curve indicating that it underwent a subcritical Andronov-Hopf bifurcation. A better test for bistability, i.e. the co-existence of a resting and spiking state, is to perform the following experiment: In one run a current is injected that slowly ramps up and in another run a current that slowly ramps down, so that in both cases a switch between resting and spiking behavior occurs (Izhikevich, 2007). If there is bistability, the switch between resting and spiking behavior occurs at a higher input current when ramping up than when ramping down which was shown to be the case in the model (Suppl. Fig. 5.11).

The third possibility is to use the model, for instance, to analyze the firing behavior of stellate cells under different conditions or to include the model into network models of grid formation as continuous attractor (Burak and Fiete, 2009; Fuhs and Touretzky, 2006; McNaughton et al., 2006) or feed-forward models (Kropff and Treves, 2008; D'Albis and Kempter, 2017; Monsalve-Mercado and Leibold, 2017). In these studies, the effect of electrophysiological characteristics as the DAP on burst firing, phase precession, grid scaling etc. could be investigated.

3.5 Do DAPs occur *in vivo*?

To investigate whether DAPs occur *in vivo* we analyzed 26 grid cells of the data set from Domnisoru et al. (2013). We found that around 20% of the cells exhibited a DAP in the STA_V - a percentage much lower than estimates from *in vitro* recordings. Whole-cell recordings are more difficult to obtain *in vivo*, so that the quality of the recording can be reduced. We found that by selecting APs from presumably good parts of the recording the visibility of DAPs could be improved, however, only a little in most cells. Therefore, we suggest that in future experiments further protocols should be run during the recording, for instance, the triangular pulse protocol that was used *in vitro* to detect DAPs. The visibility of DAPs could also be influenced by synaptic input. In the future, synaptic input of grid cells should be quantified and then could be used as input to the presented stellate cell model in order to test effects on the DAP.

3.6 DAP function: Burst firing

To investigate the relationship between DAPs and burst firing all cells were classified as bursty or non-bursty based on the spike-time autocorrelation. The

classification was confirmed by other measures of spike firing (ISI histogram, frequency of spike events and ISI return map) that showed a significant difference between bursty and non-bursty cells.

The percentage of stellate and pyramidal cells classified as bursty varied between studies. Latuske et al. (2015) classified cells into putative calbindin$^-$ cells (presumable stellate cells) and putative calbindin$^+$ cells (presumable pyramidal cells) based on theta strength and phase angle following the method by Tang et al. (2014). They found that 55% of putative calbindin$^-$ cells and 38% of putative calbindin$^+$ cells were bursty. Ebbesen et al. (2016) used either immuno-histochemistry or the method by Tang et al. (2014) to classify their cells. They reported that 13% of putative calbindin$^-$ and 48% of putative calbindin$^+$ cells were bursty. The difference might be because Latuske et al. (2015) recorded in mice and Ebbesen et al. (2016) in rats or because of the slightly different classification methods used. More evidence is needed to clarify the results.

The data set from Domnisoru et al. (2013) consisted only of grid cells. Therefore, we compared it to the findings from Latuske et al. (2015) confined to grid cells. We found that all stellate cells and 67% of the pyramidal cells from the MEC layer II were bursty (none of the three pyramidal cells from layer III were bursty). The percentage of bursty stellate cells was higher than the 73% found by Latuske et al. (2015). The disagreement likely arose from the small sample size (n=6) in the data set from Domnisoru et al. (2013). Additionally, the cell type classification methods, based on morphology (Domnisoru et al., 2013) versus indirect immunohistochemistry (Latuske et al., 2015), might have also made a difference. The percentage of pyramidal cells, that were classified as bursty, was close to the 63% reported by Latuske et al. (2015) given the small sample size (n=3).

For cells with a DAP we found that all cells besides one were classified as bursty. Furthermore, taking the mean of the STA$_V$ over all bursty and non-bursty cells respectively showed a clear DAP for bursty but not for non-bursty cells. These analyzes provide evidence towards a relationship between the DAP and burst firing *in vivo*.

3.7 Future directions: DAP function

This study gave a first impression of the relationship between DAPs and burst firing, but more experiments are needed to confirm the results.

One approach is to extend the characterization of DAPs *in vitro*, for instance, by applying the double triangular pulse protocol to cells with differently shaped DAPs and also to cells with no DAP. This could be used to analyze the effect of the DAP shape on spike firing and to quantify the difference between cells with and without DAP.

Another approach is to close the gap between *in vitro* and *in vivo* results by applying the triangular pulse and double triangular pulse protocol *in vivo*. The

triangular pulse protocol could improve the identification of cells with DAPs and therewith further the analyzes on the relationship between DAPs and burst firing. The double triangular pulse protocol could help to clarify whether DAPs also facilitate burst firing under *in vivo* conditions.

Materials and methods

<div style="text-align: right; font-size: 3em;">4</div>

4.1 Single-compartment model

A single-compartment model was used to model a typical MEC layer II stellate cell (Eq. 4.1, Fig. 4.1). This keeps the model simple as the distribution of ion channels in the dendrites has not to be taken into account and allows to investigate whether a DAP is possible without dendrites (Hypothesis 1, Sec. 1.5). The ion channels were modeled using the Hodgkin-Huxley formalism (Eq. 4.2, 4.4, 4.7) whereby the functions for the steady state (Eq. 4.5, 4.8) and the time constant (Eq. 4.6, 4.9) were adopted from Vavoulis et al. (2012). The model can be described by the following set of equations:

$$c_m \frac{dV}{dt} = -\sum_{ion\ channel} I_{ion\ channel} - I_{Leak} + I_{inj} \tag{4.1}$$

$$I_{ion\ channel} = g_{max} \cdot m^p \cdot h^q \cdot (V - E_{ion}) \tag{4.2}$$

$$I_{Leak} = g_{Leak} \cdot (V - E_{Leak}) \tag{4.3}$$

$$\frac{dm}{dt} = \frac{m_\infty - m}{\tau_m} \tag{4.4}$$

$$m_\infty(V) = \frac{1}{1 + \exp((V_{h,m} - V)/V_{s,m})} \tag{4.5}$$

$$\tau_m(V) = \tau_{min,m} + (\tau_{max,m} - \tau_{min,m}) \cdot m_\infty(V)$$
$$\cdot \exp(\tau_{delta,m} \cdot (V_{h,m} - V)/V_{s,m}) \tag{4.6}$$

$$\frac{dh}{dt} = \frac{h_\infty - h}{\tau_h} \tag{4.7}$$

$$h_\infty(V) = \frac{1}{1 + \exp((V_{h,h} - V)/V_{s,h})} \tag{4.8}$$

$$\tau_h(V) = \tau_{min,h} + (\tau_{max,h} - \tau_{min,h}) \cdot h_\infty(V)$$
$$\cdot \exp(\tau_{delta,h} \cdot (V_{h,h} - V)/V_{s,h}) \tag{4.9}$$

A legend of all symbols can be found in Tab. 4.1.

Four different types of ion channels were included in the model. Two sodium channels, one potentially for the AP upstroke and to test hypothesis 4 (window current of the Na_T channel) of DAP generation (Sec. 1.5), which will be referred to as Na_T. The other to test hypothesis 2 and 3 (Na_P or Na_R current) of DAP generation that will be called Na_P. Furthermore, a delayed-rectifier potassium channel (K_{DR}) for the AP downstroke is included into the model and a HCN channel (HCN) that is known to influence the sag and resonance behavior (Dickson et al., 2000; Nolan et al., 2007).

The correspondence between the ion channels in the model and real channels before parameter fitting only consists of the number of activation and inactivation

gates and the equilibrium potential. How well the ion channels match the role suggested here, is investigated in Sec. 2.1.2.

The model was fit to experimental data recorded at around 35°C, so that the ion channel parameters correspond to that temperature. The parameters of the model were optimized as described in the next section. The final set of parameters can be seen in Tab. 4.2 and 4.3. Ion channels with their activation and inactivation curves for the steady state and time constant are plotted in Fig. 2.8.
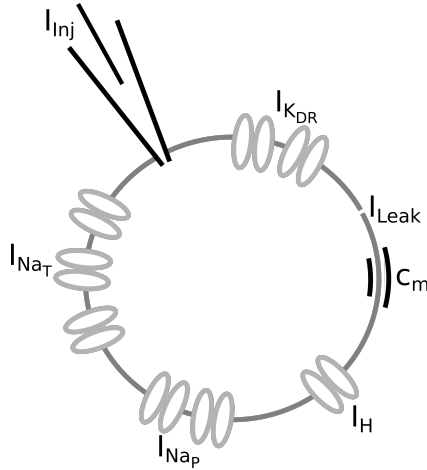

Fig. 4.1: Schematic of the single-compartment model.

Variable (base unit)	Description
c_m (F)	Capacitance
V (V)	Membrane potential
$I_{ion\ channel}$ (A)	Current flowing through the ion channel
I_{Leak} (A)	Leak current
I_{inj} (A)	Injected current
E_{ion} (V)	Equilibrium potential of the ion
E_{Leak} (V)	Equilibrium potential of the leak current
g_{max} (S)	Maximal conductance
g_{Leak} (S)	Maximal conductance of the leak current
m/h (1)	Degree of opening of the activation/inactivation gate of an ion channel
p/q (1)	Number of gates of type m/h
m_∞/h_∞ (1)	Steady state
$\tau_{m/h}$ (s)	Time constant
$V_{h,m/h}$ (V)	Shift of V in m_∞/h_∞ and $\tau_{m/h}$
$V_{s,m/h}$ (V)	Scale of V in m_∞/h_∞ and $\tau_{m/h}$
$\tau_{min,m/h}$ (s)	Smallest possible value of $\tau_{m/h}$
$\tau_{max,m/h}$ (s)	Scale of the maximum value of $\tau_{m/h}$
$\tau_{delta,m/h}$ (1)	Skewness of $\tau_{m/h}$

Tab. 4.1: Description of the variables in the model equations.

	Na$_T$		Na$_P$		K$_{DR}$	HCN
	m	h	m	h	m	h
g_{max} (S/cm^2)		0.14194		0.01527	0.00313	0.00005
p/q (1)	3	1	3	1	4	1
V_h (mV)	-30.94	-60.44	-52.82	-82.54	-68.29	-77.9
V_s (mV)	11.99	-13.17	16.11	-19.19	18.84	-20.54
τ_{min} (ms)	0	0.001	0.036	0.336	0.286	2.206
τ_{max} (ms)	0.193	8.743	15.332	13.659	21.286	137.799
τ_{delta} (1)	0.187	0.44	0.505	0.439	0.746	0.21

Tab. 4.2: Parameters of all ion channels in the model.

	General Parameter
c_m (µF/cm^2)	0.63
$length$ (µm)	100.00
$diameter$ (µm)	50.00
g_{Leak} (S/cm^2)	0.00043
E_{Leak} (mV)	-86.53
E_{HCN} (mV)	-29.46
E_{Na} (mV)	60.00
E_K (mV)	-110.00

Tab. 4.3: General parameters of the model.

4.2 Optimization procedure

4.2.1 Parameters

For the optimization the geometry of the cell body and the equilibrium potentials of sodium and potassium were fixed. The geometry was not fit because changing the length or diameter of the cell body is equivalent to changing the capacitance. The equilibrium potentials can be calculated from the solutions used in the experiment and therefore should not be changed.

The ion channels were modeled as templates of which all parameters besides the number of activation and inactivation gates and the equilibrium potential had to be optimized (see also Sec. 3.1.1). The parameter ranges were based on the order of magnitudes of experimentally measured ion channels, but were not tailored to specific ion channels. All optimized parameters and their range are shown in Tab. 4.4.

4.2.2 Error function

As error function the root mean squared error (RMSE) of the membrane potential between the experimentally recorded cell and the model of the triangular pulse experiment (Fig. 2.1; Sec. 4.3.1) was used, as the DAP is most pronounced there. A feature-based approach was not chosen, because it requires to assign a weight to each feature adding hyper-parameters and because the linear combination of different errors is more likely to introduce local minima.

Parameter	Lower bound	Upper bound
c_m (μF/cm^2)	0.3	2
E_{Leak} (mV)	-100	-75
E_{HCN} (mV)	-30	-10
g_{max} (S/cm^2)	0	0.5
$V_{h,m}$ (mV)	-100	0
$V_{h,h}$ (mV)	-100	0
$V_{s,m}$ (mV)	1	30
$V_{s,h}$ (mV)	-30	-1
$\tau_{min,m}$ (ms)	0	50
$\tau_{min,h}$ (ms)	0	50
$\tau_{max,m}$ (ms)	0	100
$\tau_{max,h}$ (ms)	0	100
HCN $\tau_{max,h}$ (ms)	0	500
$\tau_{delta,m}$ (1)	0	1
$\tau_{delta,h}$ (1)	0	1

Tab. 4.4: Lower and upper bounds for the parameters. The parameter ranges of the ion channel templates were the same for all types of ion channels besides $\tau_{max,h}$ of the HCN channel.

4.2.3 Optimization algorithm

The optimization algorithm was chosen based on a comparison of six different optimization algorithms (differential evolutionary algorithm (DEA), simulated annealing (SA), particle swarm optimization (PSO), limited memory BFGS algorithm for bound constrained optimization (L-BFGS-B), Nelder-Mead and random drawing as control). The optimization algorithms had to fit an increasing number of parameters of the standard Hodgkin-Huxley model (Fig. 4.2) (Hodgkin and Huxley, 1952). L-BFGS-B had the best performance and was thus chosen for the optimization of the stellate cell model. This algorithm belongs to the family of quasi-Newton methods that perform line search using the Newton direction, but utilize an approximation instead of the true Hessian (Nocedal and Wright, 2006).

4.2.4 Model selection

To obtain a model that not only fits the DAP as seen in Fig. 2.1 but also the other characteristics of stellate cells, the optimization algorithm was applied repeatedly whereby the parameter ranges for the generation of the initial candidates was narrowed towards good solutions from the last run. Good solutions were selected by hand based on the performance of the model on the protocols: double triangular pulse, step current and ZAP (Sec. 4.3.1). The double-sine protocol was unseen during the fitting process and therefore could be used as test set.

4.3 Data sets used

Two different experimental data sets were analyzed, one carried out in *vitro* (Kümpfbeck, 2019), one *in vivo* (Domnisoru et al., 2013). I am grateful to the
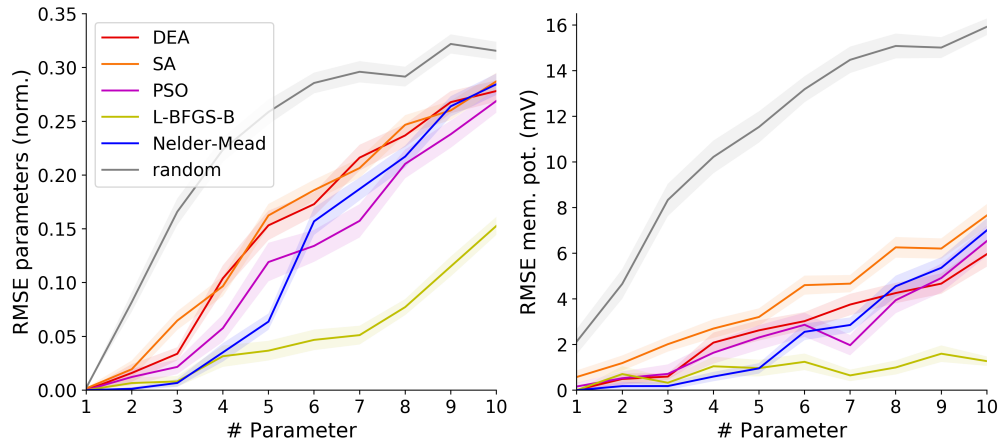
Fig. 4.2: Performance of six different optimization algorithms on fitting parameters of the standard Hodgkin-Huxley model. The algorithms tested are differential evolutionary algorithm (DEA), simulated annealing (SA), particle swarm optimization (PSO), limited memory BFGS algorithm for bound constrained optimization (L-BFGS-B), Nelder-Mead and random drawing as control. All algorithms had the same constraints: # trials: 100, # candidates: 250, # iterations: 250, started from the same initial parameters and had the same parameter bounds (where applicable). For the algorithms DEA and PSO all candidates are optimized simultaneously in one population whereas for all other algorithms candidates are optimized one by one. In the left plot, the error in the parameters computed as the RMSE between the parameters of the best candidate and the true values normalized by the parameter bounds is shown. In the right plot, the RMSE between the membrane potential trace of the best candidate and the true trace is depicted. The lines and shaded regions are the mean and standard error of the mean over trials.

researchers to provide their data to me. In what follows, key information is provided. For details, see the respective publications.

4.3.1 Data set from Kümpfbeck (2019)

Franziska Kümpfbeck obtained whole-cell recordings *in vitro* from the MEC layer II in Long-Evans rats and Mongolian gerbils (Kümpfbeck, 2019). For the present study only the recordings from Long-Evans rats were used. The liquid junction potential (LJP = 16 mV) was corrected for. The behavior of the cells was investigated by applying different sets stimuli that are explained below.

Protocols

Triangular pulse
Injection of a short triangular pulse that started at 10 ms, rose for 0.8 ms and descended for 1.2 ms with a given peak amplitude. A triangular pulse instead of a square-shaped pulse was used for more continuous and therewith natural stimulation of the cell.

Double triangular pulse
As control an AP was elicited in the beginning of the experiment by injection of a triangular pulse at 20 ms. The baseline was set to -0.05 nA to keep the

effect of the baseline and hyperpolarization, no polarization and depolarization apart. At 222 ms a hyper-/no-/depolarizing step current with an amplitude of -0.1/0/0.1 nA respectively was injected that continued for 125 ms (in Fig. 2.3 C) or 250 ms (in Fig. 2.3 A, B). The 1st triangular pulse of the experiment's main part is inserted 12, 15 or 20 ms after the step to elicit a spike followed by a DAP. The 2nd triangular pulse is used to test how much current is needed to elicit a second spike at different time points during the DAP (starting 3, 7, 9, 11, 13, 15, 17, 19, 21 ms after the onset of the 1st triangular pulse). The amplitude of the 2nd triangular pulse was raised in steps of 0.05 nA. All triangular pulses have a rise of 0.8 ms and a descend of 1.2 ms.

Step current

A step current with a duration of 500 ms is injected between 250 and 750 ms. The amplitude starts at -0.15 nA and is increased by increments of 0.05 nA.

ZAP

The ZAP stimulus was an oscillatory current whose frequency linearly increased over time. The formula is as follows:

$$ZAP(t) = a \cdot \sin(2\pi(f_0 \cdot t + \frac{1}{2}\frac{f_1 - f_0}{T} \cdot t^2))$$

(4.10)

The frequency in this case changed from 0 to 20 Hz within 30 s and the amplitude was set to 0.1 nA. There was an offset of 2 s before and after the ZAP stimulus.

Double-sine

The double-sine stimulus consisted of a ramp modeled as the upper half of a sine with a low frequency ($f_1 = 0.1$ Hz) superimposed by a sine with a frequency in the theta range ($f_2 = 5$ Hz):

$$Double\text{-}sine(t) = a_1 \cdot \sin(2\pi \cdot t \cdot f_1) + a_2 \cdot \sin(2\pi \cdot t \cdot f_2)$$

(4.11)

Before and after the double-sine stimulus was an offset of 0.5 s.

4.3.2 Data set from Domnisoru et al. (2013)

Domnisoru et al. (2013) obtained whole-cell recordings from cells in the mouse MEC *in vivo*. During the recording the mice were running on a cylindrical treadmill navigating through a virtual linear track. 27 of the recorded cells were identified as grid cells. 26 of those cells are investigated in this study, as the data for one cell got corrupted.

From the identified grid cells 12 were filled with biocytin. Based on the morphology the cells were classified as stellate or pyramidal and depending on the location of the soma assigned to layer II or III of the MEC.

Another division of the cells could be made based on the theta resonance. Large-theta cells could be distinguished by having a mean theta envelope higher than 4.7 mV.

4.4 Analyses

4.4.1 Identification of cells with a DAP *in vitro*

To determine the quality of the model we examined whether the model lied within the distribution of real MEC layer II cells from the data set recorded by Kümpfbeck (2019). Because the model was specifically designed to fit cells with a DAP, the real cells used for the comparison were filtered for having a DAP. Only those cells where accepted where the AP and DAP characteristics (computed as described in Sec. 4.4.3) lied within the ranges stated in Tab. 4.5. The MEC layer II cells that had a DAP will be referred to as $MECII_{DAP}$ cells. The total number of cells was 385, however, the number of cells varies between plots as only those cells are shown for which the respective protocol was conducted. The $MECII_{DAP}$ population includes both stellate and pyramidal cells.

	Lower bound	Upper bound
AP amplitude (mV)	50	150
AP width (ms)	0.1	2.0
fAHP amplitude (mV)	0	40
DAP amplitude (mV)	0	40
DAP deflection (mV)	0	20
DAP width (ms)	0	70
$Time_{AP\text{-}DAP}$ (ms)	0	20

Tab. 4.5: Valid ranges for AP and DAP characteristics.

4.4.2 Determination of highest density regions (HDR)

To quantify how well the model accords to the distribution of $MECII_{DAP}$ cells, we estimated highest density regions (HDR) with respect to the main stellate cell characteristics (Hyndman, 1996). A HDR measures how many percent of the sample space X have a higher or equal probability density than a specific value x_s. It can be defined as:

$$\text{HDR}(x_s) = \{x \in X : PDF(x) \geq PDF(x_s)\} \tag{4.12}$$

The probability of this region is $p = p[x \in \text{HDR}(x_s)]$, so that x_s has a $p \cdot 100\%$ HDR. For example, if a model characteristic has a 75% HDR with respect to the $MECII_{DAP}$ distribution, on average 25% of newly recorded $MECII_{DAP}$ cells will have lower probability density of that characteristic than the model. HDRs have an advantage over standard deviations, as they can be used for any, also multimodal and asymmetric distributions.

To compute HDRs, firstly, the probability density from the MECII$_{\text{DAP}}$ population has to be estimated. A common method is to use kernel density estimation with a Gaussian kernel. In this method a Gaussian is placed over each data point x_n from the data set X_N. The probability density is obtained by summing all Gaussians and dividing by the number of data points N, so that the probability density is normalized to an area of one (Bishop, 2006):

$$PDF(x) = \frac{1}{N} \sum_{n=1}^{N} \frac{1}{\sqrt{2\pi\sigma^2}} \exp\left(-\frac{(x - x_n)^2}{2\sigma^2}\right) \tag{4.13}$$

where σ was estimated using Scott's rule: $\sigma^2 = \sigma^2_{X_N} \cdot N^{-\frac{2}{5}}$ (Scott, 2015).

Then, the HDR can be estimated by drawing a set of samples X_M from this distribution. The probability of the largest region including x_s is the number of samples x_m that have a higher or equal probability density than x_s divided by the total number of samples M:

$$p[x \in \text{HDR}(x_s)] = \frac{\# \left[x_m \in X_M : PDF(x_m) \geq PDF(x_s)\right]}{M} \tag{4.14}$$

We used 1 000 000 samples to estimate the HDR.

4.4.3 Determination of DAP characteristics

To compute the DAP characteristics as shown in Fig. 2.2 A, Fig. 2.14 and Fig. 2.18 the resting potential as well as the following three points were needed: The AP peak, the fAHP minimum and the DAP maximum.

The AP peak was determined as the maximum of the membrane potential within 2.5 ms after crossing the AP threshold at -10 mV. To detect the fAHP minimum and the DAP maximum in the *in vitro* recordings the membrane potential was interpolated using cubic splines. Interpolation was not done in the case of the model (contained no noise) or *in vivo* recordings (averaged data was sufficiently smooth). The fAHP minimum was then set to the lowest local minimum in the 4 ms following the AP peak. The DAP maximum was determined as the highest local maximum within 0.5 ms to 10 ms after the fAHP minimum. The local minimum/maximum had to fulfill the condition that points within 1 ms to each side had to be higher/lower than the point in the middle. If no minimum/maximum fulfilling the condition could be found, the cell was assumed to have no DAP.

From these reference points, together with the resting potential, the DAP characteristics can be computed. The DAP deflection is the difference of the membrane potential between the DAP maximum and the fAHP minimum. The DAP amplitude is the difference of the DAP maximum to the resting potential. The DAP width is the time interval from the fAHP minimum until the crossing of the membrane potential at half the fAHP height (the voltage at the fAHP minimum minus the resting potential). The Time$_{\text{AP-DAP}}$ is the time period between the AP peak and the DAP maximum.

In vitro and for the model the resting potential was computed as the mean of the membrane potential before current injection. However, *in vivo* no resting potential could be computed, as the membrane potential was constantly fluctuating, and therefore only DAP deflection and Time$_{\text{AP-DAP}}$ were used.

4.4.4 Determination of other characteristics

To compare the model to experimental data in Sec. 2.1.1 some characteristics were introduced that will be defined here.

To quantify the response of a cell to a negative step current the steady state amplitude and sag deflection were computed. The steady state amplitude is the difference between the voltage at steady state and the resting potential whereby the voltage at steady state is determined as the mean of the membrane potential over the last fourth of the step current. The sag deflection is the distance between the voltage at steady state and the minimum of the membrane potential within the first fourth of the step current.

Step currents eliciting superthreshold responses were characterized by the latency of the first spike, ISI$_{1/2}$ and by fitting the F-I curve with a power function. ISI$_{1/2}$ is the ratio between the 1st and 2nd ISI computed from the trace with the lowest step amplitude having at least four APs. Three APs would be enough in principle, however, voltage traces with four APs exhibited more representative firing patterns. The latency of the first spike is the time between the onset of the stimulus and the peak of the first spike. It was determined from the trace with the lowest step amplitude that had at least one AP. The F-I curve was approximated by the following function:

$$f(x) = \begin{cases} a \cdot (x - b)^c & \text{if } x \geq b \\ 0 & \text{else} \end{cases} \tag{4.15}$$

whereby f(x) was given in Hz and x in nA. The parameters a, b, c were fit using non-linear least squares with the initial values: $a_0 = 50$, $b_0 =$ highest current where the F-I curve was still zero, $c_0 = 0.5$.

To quantify the resonance behavior the impedance was computed as:

$$Z = \left| \frac{FFT(V)}{FFT(I)} \right| \tag{4.16}$$

and then smoothed using LOWESS (locally weighted scatterplot smoothing). The resonance frequency is the frequency where the impedance is maximal. The Q-value is defined as the maximal impedance divided by the impedance at frequency 0.

For the evaluation of the sine stimulus the spike phases were determined. The spike phase is the position of the AP peak with respect to the theta oscillation of the input stimulus. From the spike phases the circular mean and standard deviation were computed.

4.4.5 Comparison of the model with an inhomogeneous Poisson process

To quantify the performance of the model on the double-sine protocol, it was compared to an inhomogeneous Poisson process. The probability of a spike train with the ordered spike times t_1, t_2, ..., t_n can be described by an inhomogeneous Poisson process as follows (Dayan and Abbott, 2001):

$$p[t_1, t_2, ..., t_n] = \exp\left(-\int_0^T r(t)dt\right)\prod_{i=1}^{n} r(t_i) \tag{4.17}$$

where $r(t)$ is the time-dependent firing rate that was set to the double-sine input stimulus scaled to the average firing rate of the experimentally measured cell.

Firstly, 1 000 000 spike trains were generated using the inhomogeneous Poisson process (Dayan and Abbott, 2001). For each spike train the phase distribution with respect to the intrinsic theta oscillation was determined. The similarity to the phase distribution of the real cell was computed by the RMSE between both distributions. The distribution of the RMSE from all Poisson-generated spike trains was used to built a test statistic for the model. The p-value for the null hypothesis that the RMSE of the model ($RMSE_{\text{model}}$) is equal or higher than the RMSE of the inhomogeneous Poisson process ($RMSE_{\text{Poisson}}$), i.e. that the model performs worse than the inhomogeneous Poisson process in reproducing the data, can be approximated as

$$p\left[RMSE_{\text{model}} \geq RMSE_{\text{Poisson}}\right] = \frac{\#[RMSE_{\text{model}} \geq RMSE_{\text{Poisson}}]}{\#RMSE_{\text{Poisson}}} \tag{4.18}$$

where $\#[RMSE_{\text{model}} \geq RMSE_{\text{Poisson}}]$ is the number of Poisson-generated spike trains which have smaller or equal RMSE than the model and $\#RMSE_{\text{Poisson}}$ is the total number of Poisson-generated spike trains. The null hypothesis can be rejected if the p-value is small.

4.4.6 Voltage clamp protocols

Na_T

The voltage clamp protocol for investigating Na_T channels consisted of two voltage steps. The first step was hold at -80 mV for 10 ms. This enforces Na_T channels to be closed and non-inactivated. The second step iterates over different voltages and is hold for 50 ms. Na_T channels would respond to more positive potentials with a negative current that peaks within a few milliseconds and then decays to zero (Magistretti and Alonso, 1999, Hargus et al., 2011, Nigro et al., 2012). This is caused by the fast opening of Na_T channels followed by inactivation.

Na_R

The voltage clamp protocol for Na_R channels visualizes not only resurgent, but also transient and persistent activity (Lewis and Raman, 2014). It is therefore

especially suited to investigate the presence of a certain sodium channel. The protocol starts with a step hold at -80 mV for 10 ms bringing sodium channels to a closed, non-inactivated state. Then a step to 0 mV continuing for 20 ms is applied. A negative current during this step indicates the transient component that is caused by fast opening of Na_T channels followed by inactivation. The third step iterates over several voltages and lasts 100 ms. As Na_T channels are inactivated from the previous step, they show no response. However, Na_R channels cause a negative current due to fast de-inactivation (Hargus et al., 2011, Nigro et al., 2012). Subsequently, the current can approach a constant value representing the persistent component.

K_{DR}

To bring potassium channels to a closed, non-inactivated state the cell was clamped to -110 mV for 150 ms. The second step was used to inactivate the fast transient current of K_A channels by stepping to -50 mV for a duration of 50 ms. The current flow of K_{DR} channels was then measured by clamping at different voltages for 150 ms. K_{DR} channels show a sustained positive current with slow inactivation (Eder and Heinemann, 1996).

HCN

The voltage protocol for HCN channels starts with a voltage step to -60 mV for 20 ms so that HCN channels are in a non-inactivated state. The second step lasts 1500 ms and iterates over several voltages. For more negative potentials HCN channels are released from inactivation causing an increase in current flow within a time scale of hundreds of milliseconds that approximates a constant value (Dickson et al., 2000).

4.4.7 Sensitivity analysis

In order to investigate the effect of the model parameters on DAP characteristics a sensitivity analysis was conducted. For this purpose one million models were generated by randomly sampling parameters one order of magnitude around the original parameters (Tab. 4.2, 4.3). The sampled models were simulated given a triangular pulse as input. From their response the AP amplitude, AP width, fAHP amplitude and DAP characteristics (DAP deflection, DAP amplitude, DAP width and $Time_{AP\text{-}DAP}$) were computed. For all models for which the characteristics were available and within the valid ranges defined in Tab. 4.5 (3 587/1 000 000 models) a correlation analysis was performed. Correlations were computed by Kendall's tau, as it is a robust, non-parametric method (Knight, 1966). However, Spearman's and Pearson's correlation coefficient gave similar results (Fig. 5.2).

Two analyses were performed on the models. Firstly, it was tested whether the data set was large enough to estimate correlations. This was done by dividing the data set into 35 subsets with 102 models, respectively. For each subset the correlations between model parameters and DAP characteristics were computed

and it was checked whether the standard deviations of the correlations over subsets were low. Secondly, it was investigated whether strong and significant correlations exist in the whole data set. For the significance test the p-values derived from Kendall's tau were adjusted using the Bonferroni correction to account for multiple testing.

4.4.8 Spike-triggered average of the membrane potential (STA_V)

For the computation of the $STAs_V$ in Sec. 2.2 the AP peak indices provided with the dataset by Domnisoru et al. (2013) were used. For each AP peak a window was drawn around the spike ranging from 10 ms before until 25 ms after the AP peak. The window was discarded if another AP peak lay inside. To compute the STA_V for a cell the mean over all its AP windows was taken.

Selection of APs

In Sec. 2.2 it was reasoned that the quality of the recording determines how well DAPs can be recognized in the STA_V. In order to test that prediction it was necessary to distinguish at which times a recording was good.

In vivo the quality of the recording is reduced due to an increased series resistance (the sum of the pipette resistance and the resistance at the pipette-cell junction) (Wang et al., 2016; Margrie et al., 2002). The series resistance together with the pipette capacitance act as a low pass filter on the voltage signal. An increased series resistance leads to a decrease in the passband of the filter which causes, for instance, APs to be smaller and wider. Therefore, as an approximation for the quality of the recording, the AP amplitude and width were used.

The threshold for the AP amplitude and width was chosen so that all cells for which a DAP could already be recognized in the STA_V lay within the region classified as good recording. In particular, the threshold was set to the middle between the outermost cell with a DAP and the closest cell without a DAP for AP amplitude and width, respectively. The thresholds (AP width < 0.72 ms and AP amplitude > 51.8 mV) were then used to select those APs that enter the computation of the STA_V.

4.4.9 Classification into bursty and non-bursty

Grid cells were classified into bursty and non-bursty cells based on the spike-time autocorrelation (1 ms/bin) up to 50 ms. The spike-time autocorrelation was set to zero for no time lag and normalized to an area of one. A principal component analysis (PCA) (Pearson, 1901) was performed on the spike-time autocorrelations from all cells to identify the directions of highest variance. The first two principal components were used for the classification. A k-means cluster algorithm (MacQueen et al., 1967) with the number of clusters set to two was applied to split the cells into bursty and non-bursty. Inspecting examples from each cluster confirmed that bursty cells had a higher spike-time autocorrelation

for short time lags than non-bursty cells (Fig. 2.19). Accordingly, cumulative ISI histograms had higher slopes for short ISIs for bursty compared to non-bursty cells (Fig. 2.22).

4.4.10 Other characterizations of the firing behavior

For the ISI histogram and ISI return map only ISIs ≤ 200 ms were used as longer time scales are irrelevant for distinguishing burst and non-burst behavior. The ISI histogram had a bin width of 1 ms/bin and was normalized to an area of one.

To compute the frequency of spike events a spike event was defined as a sequence of APs where the time interval between each pair of spikes had to be ≤ 8 ms. The frequency of each spike event was normalized by dividing by the total number of spike events. The relative frequency was then plotted on a linear and logarithmic scale.
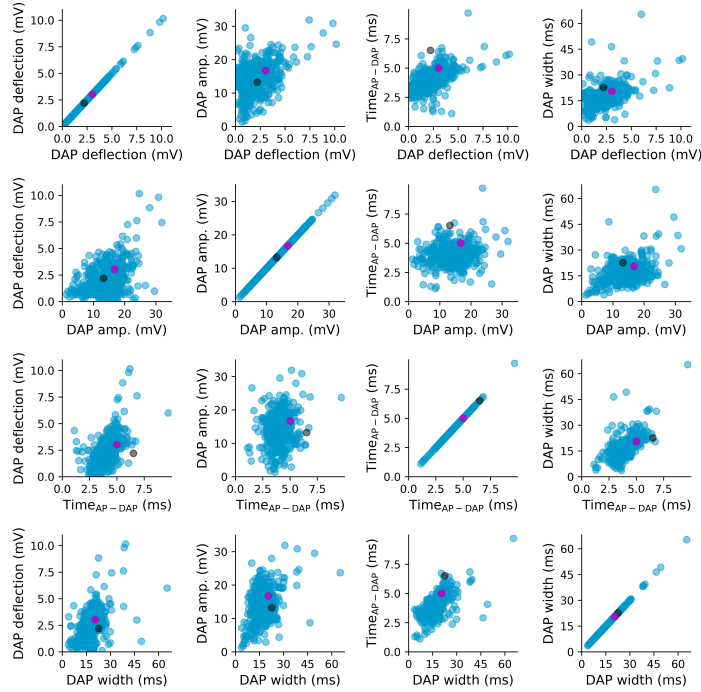
Fig. 5.1: 2D scatter plots of the distribution of DAP characteristics of the model (black) in comparison to the MECII$_{DAP}$ population (blue) and the target cell (magenta).
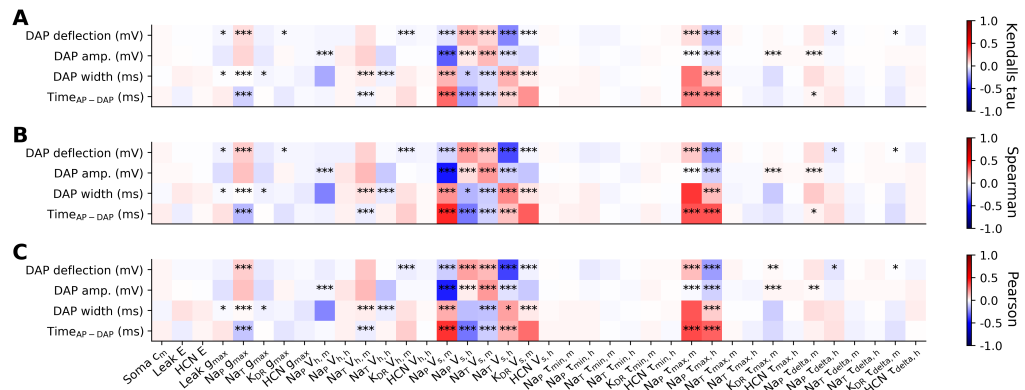

Fig. 5.2: Comparison of different correlation measures for the sensitivity analysis. Kendall's tau (A), Spearman's (B) and Pearson's (C) correlation between the parameters and DAP characteristics of the model with Bonferroni corrected p-values (p-val. < 0.1, 0.01, $0.001 = *, **, ***$).

5.1 Comparison of five different models

In this section the model analyzed in Sec. 2.1 (here model 1) and four other models are shown to visualize the similarities and differences of models built with the same structure and optimization procedure.

Parameter	Model 1	Model 2	Model 3	Model 4	Model 5
c_m (μF/cm^2)	0.627407659	0.673718623	0.507550843	0.691542	0.640349
$length$ (μm)	100	100	100	100	100
$diameter$ (μm)	50	50	50	50	50
E_{Leak} (mV)	-86.531398343	-86.793412589	-88.055860574	-84.3537	-88.2075
E_{HCN} (mV)	-29.456682181	-27.596796283	-29.779735489	-29.307	-26.7741
E_{Na} (mV)	60	60	60	60	60
E_K (mV)	-110	-110	-110	-110	-110
g_{Leak} (S/cm^2)	0.000430117	0.000779596	0.000485971	0.000558033	0.00160234
Na$_P$ g_{max} (S/cm^2)	0.015272213	0.012113085	0.024674905	0.0100557	0.0379042
Na$_T$ g_{max} (S/cm^2)	0.141941547	0.103247371	0.248356679	0.100142	0.222564
K$_{DR}$ g_{max} (S/cm^2)	0.003125397	0.003686712	0.010919816	0.00263726	0.0120953
HCN g_{max} (S/cm^2)	$5.322 \cdot 10^{-5}$	0.0001323	$3.242 \cdot 10^{-5}$	0.000119098	0.000115592
Na$_P$ $V_{h,m}$ (mV)	-52.81768	-55.353542478	-53.77269401	-53.3938	-53.3628
Na$_P$ $V_{h,h}$ (mV)	-82.54144	-79.631236292	-80.612595471	-78.3584	-81.5975
Na$_T$ $V_{h,m}$ (mV)	-30.93933	-32.913369899	-33.055814114	-34.3547	-31.6806
Na$_T$ $V_{h,h}$ (mV)	-60.44199	-72.08832547	-59.17759006	-74.6419	-68.0021
K$_{DR}$ $V_{h,m}$ (mV)	-68.28729	-67.715013369	-67.263599118	-67.0344	-66.2632
HCN $V_{h,h}$ (mV)	-77.90055	-84.54277025	-85.746567678	-78.2075	-80.6636
Nap $V_{s,m}$ (mV)	16.107894681	16.387992168	16.150191811	14.7591	17.1306
Nap $V_{s,h}$ (mV)	-19.193893103	-21.41013122	-22.844222479	-19.3687	-19.1157
Nat $V_{s,m}$ (mV)	11.986102516	14.457205652	12.742500305	13.5563	15.0649
Nat $V_{s,h}$ (mV)	-13.174636462	-14.042680864	-13.631565851	-13.5885	-12.7681
Kdr $V_{s,m}$ (mV)	18.844244474	18.797037815	18.16355694	18.5827	17.9354
HCN $V_{s,h}$ (mV)	-20.535609569	-19.347698213	-20.441746416	-20.3833	-18.2677
Nap $\tau_{min,m}$ (ms)	0.035622452	0.016143355	0.084659847	0.0216391	0.276214
Nap $\tau_{min,h}$ (ms)	0.335862929	0.514528052	0.574603314	0.398175	0.67264
Nat $\tau_{min,m}$ (ms)	$3 \cdot 10^{-9}$	0	$1 \cdot 10^{-9}$	0.0326277	0.0246678
Nat $\tau_{min,h}$ (ms)	0.000919782	$5.717 \cdot 10^{-5}$	0.243969122	0.0296275	0.0890201
Kdr $\tau_{min,m}$ (ms)	0.2857844	0.446112614	0.228334006	0.2552	0.688191
HCN $\tau_{min,h}$ (ms)	2.206156686	4.668802614	4.257724746	3.0777	6.01924
Nap $\tau_{max,m}$ (ms)	15.331610852	17.103786642	17.427725129	17.187	18.1061
Nap $\tau_{max,h}$ (ms)	13.658651289	18.368726696	16.276107748	15.6257	16.3773
Nat $\tau_{max,m}$ (ms)	0.193252151	0.156283577	0	0.186841	0.164704
Nat $\tau_{max,h}$ (ms)	8.743416128	8.413102152	10.574012247	10.1194	8.979
Kdr $\tau_{max,m}$ (ms)	21.285696736	21.116372985	21.457143615	22.5133	22.02
HCN $\tau_{max,h}$ (ms)	137.799112777	135.216196588	137.204896694	133.712	128.051
Nap $\tau_{delta,m}$ (1)	0.505477008	0.434638993	0.57090503	0.469318	0.400833
Nap $\tau_{delta,h}$ (1)	0.439179987	0.722164327	0.380378834	0.422425	0.953268
Nat $\tau_{delta,m}$ (1)	0.187070568	0.24005087	0.146145937	0.313401	0.305363
Nat $\tau_{delta,h}$ (1)	0.439803428	0.330430454	0.359211676	0.43633	0.287004
Kdr $\tau_{delta,m}$ (1)	0.746024007	0.706951349	0.628309909	0.657289	0.611571
HCN $\tau_{delta,h}$ (1)	0.210320088	0.164162369	0.372886626	0.253464	0.0459246

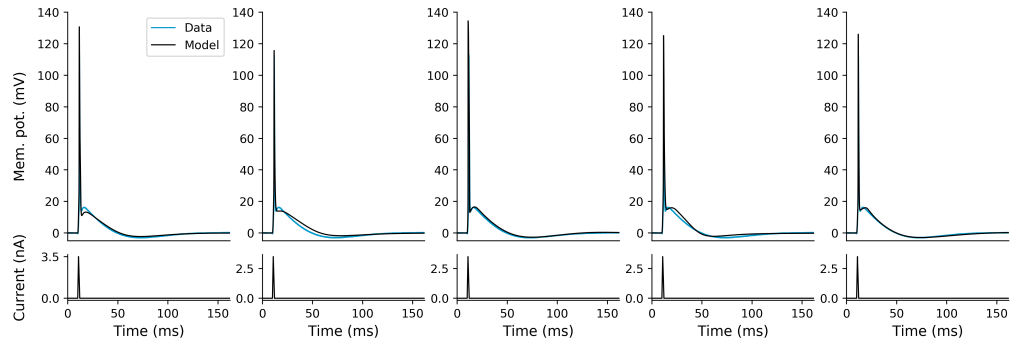**Tab. 5.1:** Parameter values for the five different models.

Fig. 5.3: Membrane potential of the real (blue) and simulated cell (black) in response to a short triangular pulse (bottom plot) for five different models.
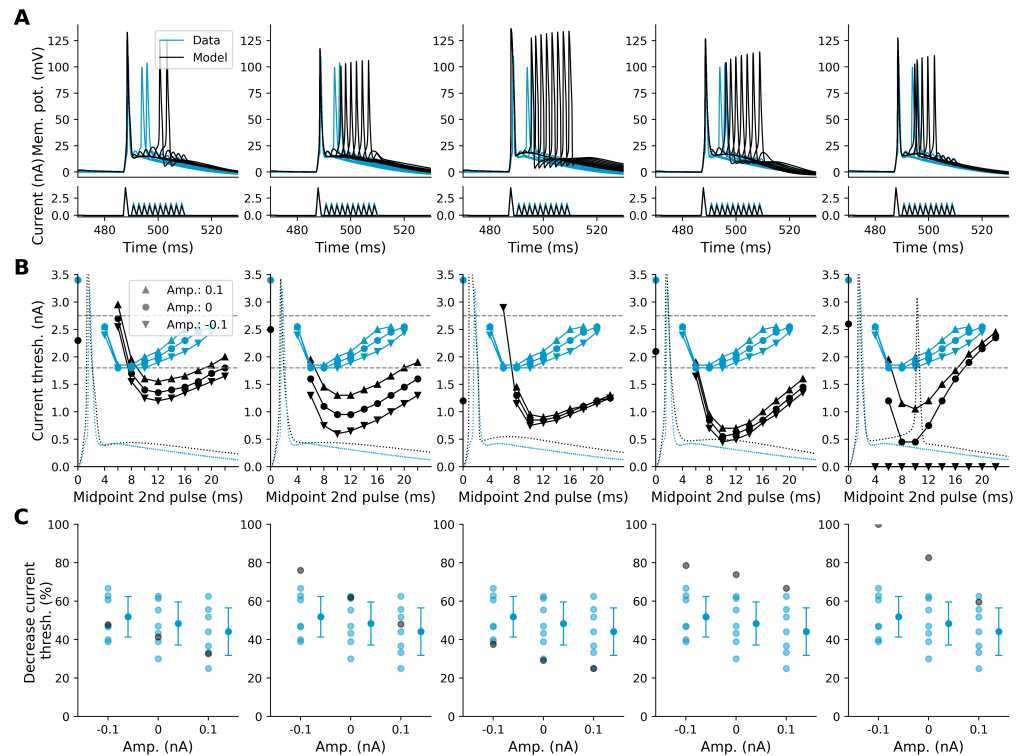

Fig. 5.4: Performance of the five different models for the double ramp protocol. A: Membrane potential of the real (blue) and simulated cell (black) in response to the double triangular pulse (bottom plot). B: Current threshold at rest (black and blue dot at 0 ms) and during the DAP for different amplitudes of the preceding step current (▲: 0.1 nA, ●: 0 nA, ▼: -0.1 nA) applied from 222 to 472 ms. Dotted lines indicate the shape of the AP and DAP for the real and simulated cell, respectively. Dashed lines indicate the range of amplitudes tested in case of the experimental data. C: Percentage of the decrease in current threshold from rest compared to the lowest threshold during the DAP of real cells (blue) and the model (black). Next to it, the mean and standard deviation over real cells.
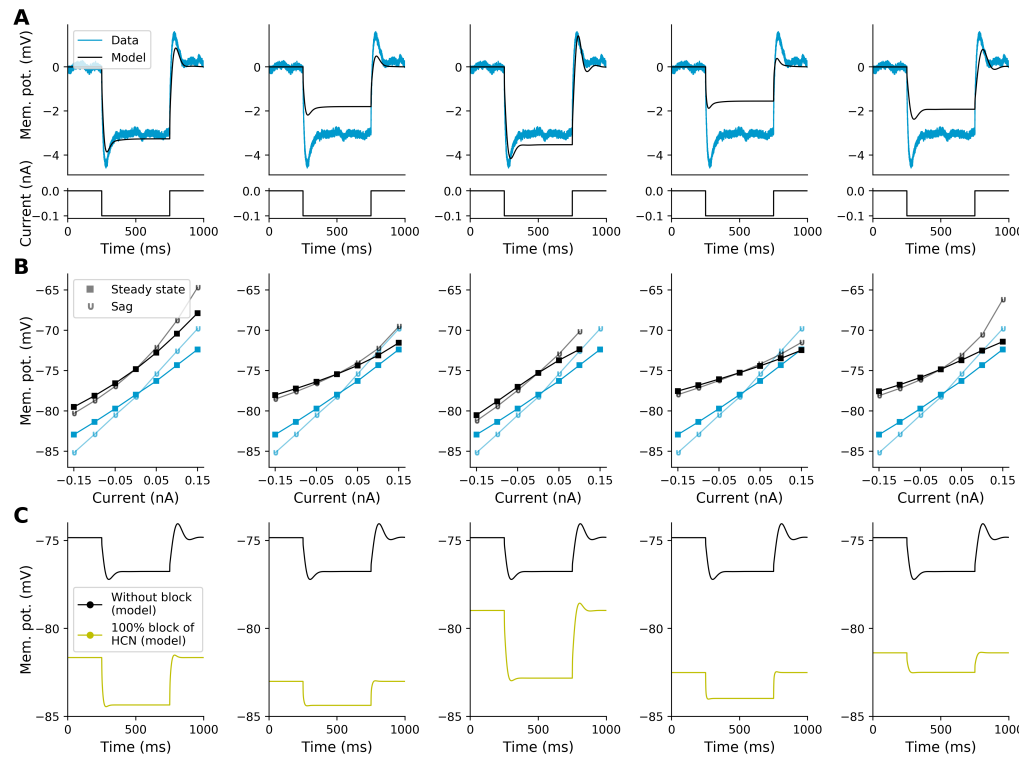
Fig. 5.5: Performance of the five different models for negative step currents. A: Membrane potential of the recorded (blue) and simulated cell (black) in response to a negative step current. B: Comparison of the voltage at steady state versus the sag peak for the experimental data (blue) and the model (black). C: Membrane potential of the model without (black) and with 100% block (yellow) of the HCN channel.
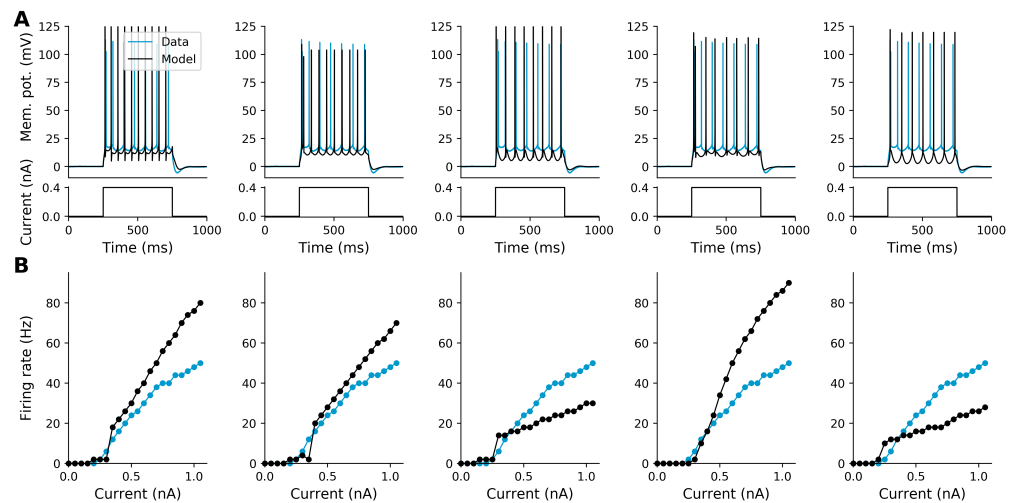

Fig. 5.6: Performance of the five different models for positive step currents. A: Membrane potential of the recorded (blue) and simulated cell (black) in response to a positive step current (bottom plot). B: F-I curve of the recorded (blue) and simulated cell (black).
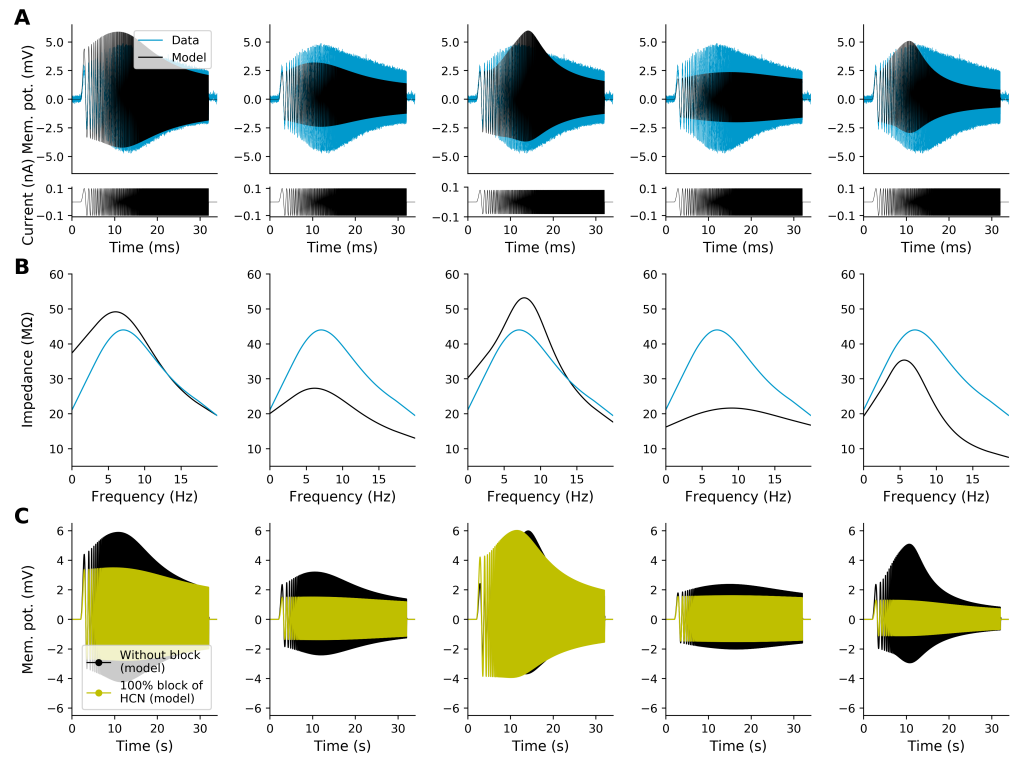
Fig. 5.7: Performance of the five different models for a ZAP current. A: Membrane potential of the recorded (blue) and simulated (black) cell in response to a ZAP current (bottom plot). B: Impedance computed from the traces shown in A. C: Membrane potential of the model without (black) and with 100% block (yellow) of the HCN channel.
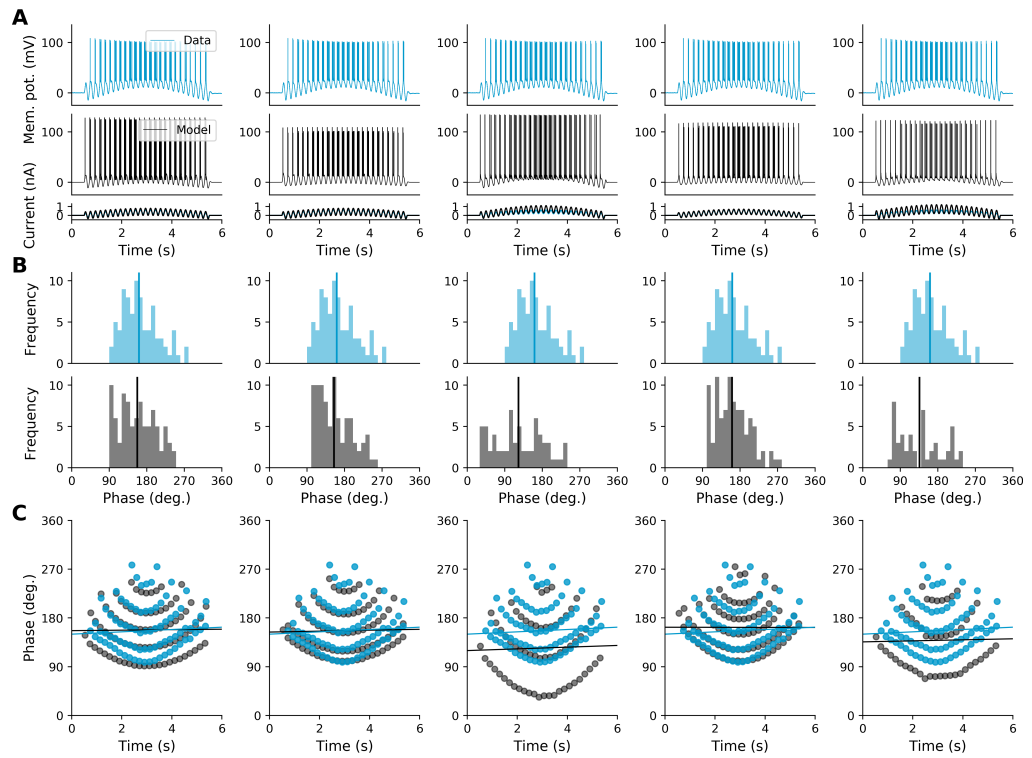
Fig. 5.8: Performance of the five different models for the double-sine stimulus. A: Membrane potential of the recorded (blue) and simulated cell (black) in response to the double-sine stimulus (bottom plot). B: Phase histogram of the APs with respect to the theta oscillation for the traces shown in A. C: Phase of the AP peaks with respect to the theta oscillation as a function of time and the linear regression lines fit to them.
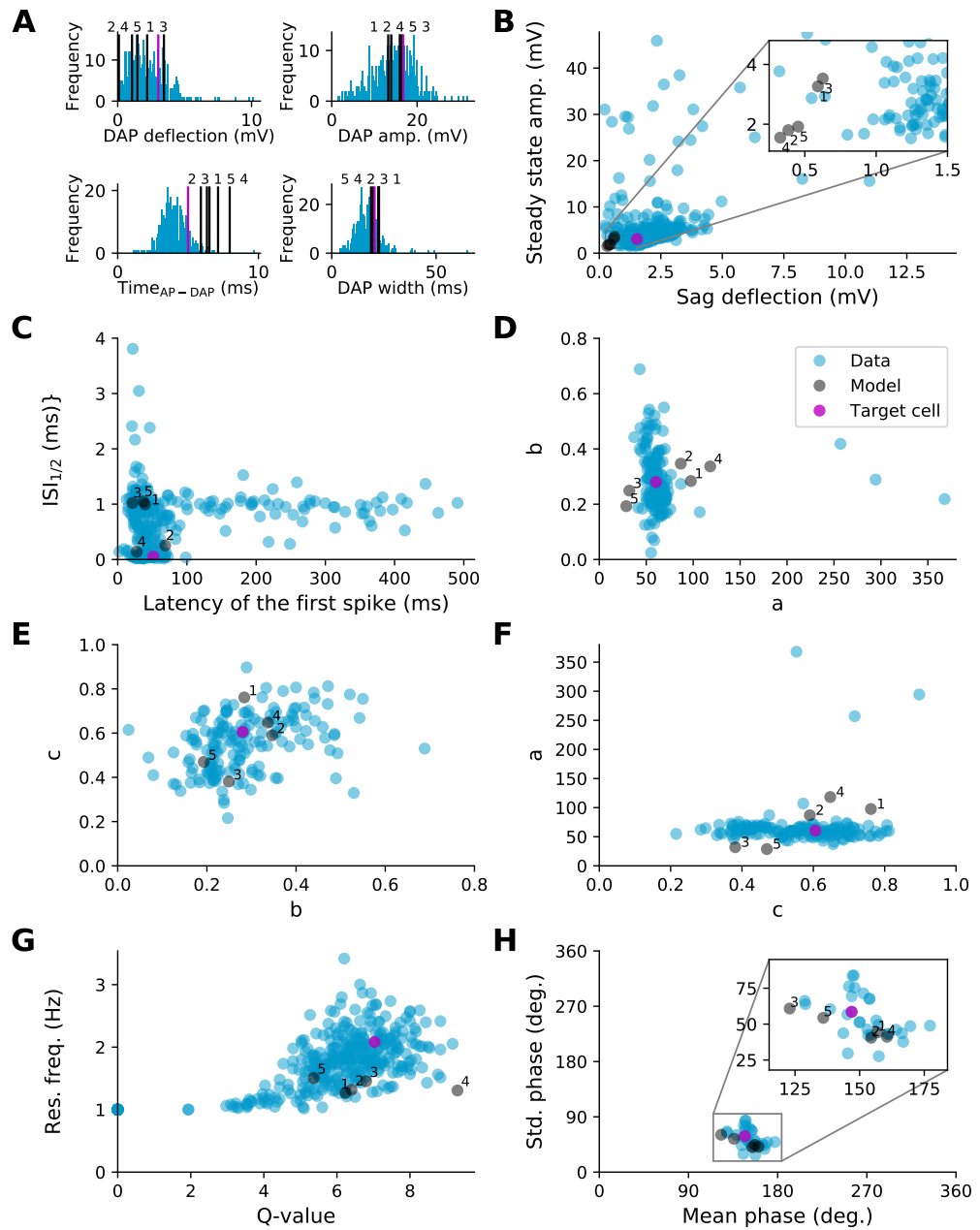
Fig. 5.9: Comparison of the five models (black with model number) to the MECII_DAP population (blue) and the target cell (magenta) to which the model was fit. A: Distribution of DAP deflection, DAP amplitude, Time_AP-DAP and DAP width. The numbers indicate the order in which the values of the models appear. B: Sag deflection and amplitude at steady state. The inset enlarges the region around the models. C: Latency of first spike and ISI$_{1/2}$. D, E, F: 2D plots for a (scaling), b (shift) and c (exponent) obtained by fitting the F-I curve to Eq. 2.1 requiring RMSE≤20 Hz. G: Q-value and resonance frequency. H: Mean and standard deviation of the phase histogram.
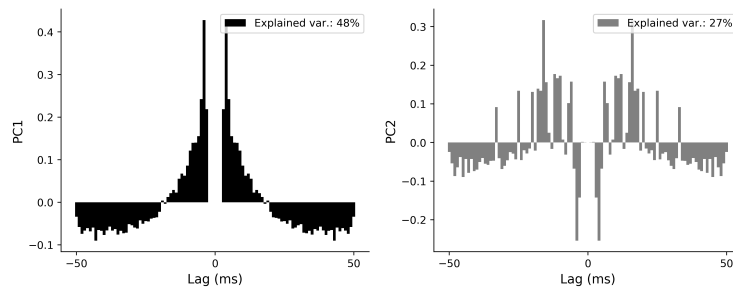
Fig. 5.10: First two principal components of the PCA of the spike-time autocorrelations. The value in the upper right is the percentage of the variance explained by the respective component.

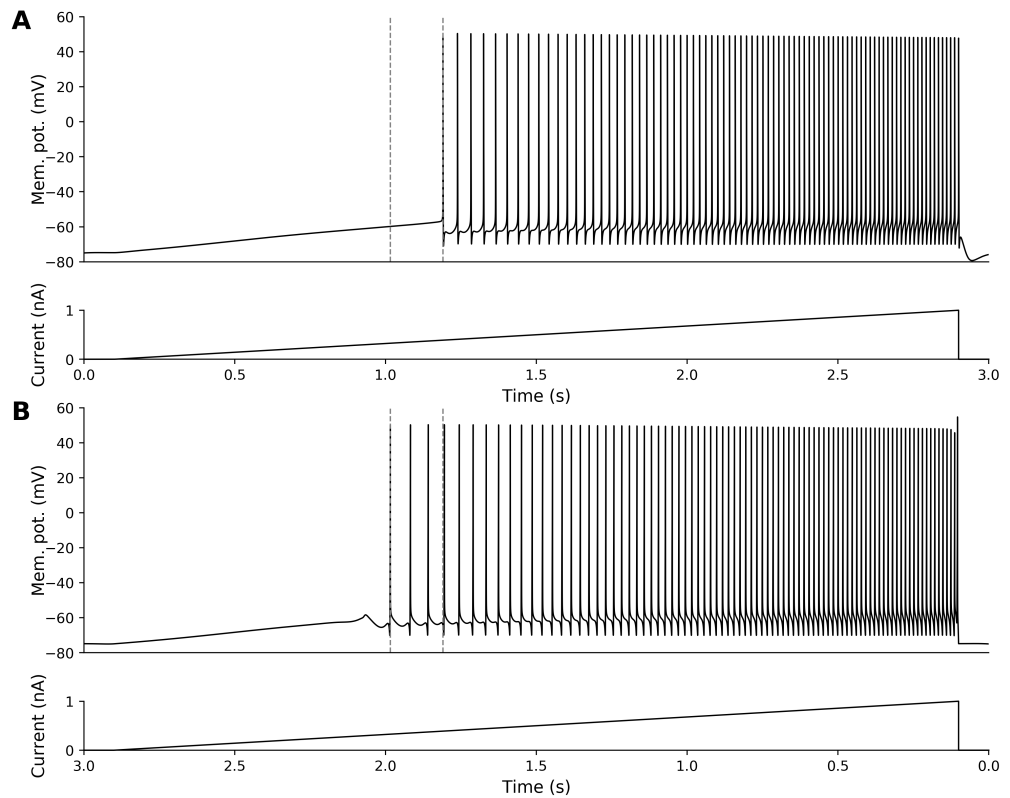**Fig. 5.11:** Bistability in the model when a slow ramp current is injected. A: The membrane potential in response to a slowly upwards ramping current (lower plot) is shown. B: The membrane potential in response to a slowly downwards ramping current (lower plot) is shown. The membrane potential is plotted with reversed time to visualize the difference in the onset of spiking that is indicated by the gray dashed lines in both plots.

Acknowledgement

First of all, I want to thank Andreas Herz for accommodating me in his lab. He was always open for discussions, sparked new ideas and listened to our sorrows. Besides, he has a knack for the important, little details.

I also like to thank Martin Stemmler, Anton Sirota, Christian Wahl-Schott and Stefan Häusler for their constructive suggestions and critique regarding my work. Franziska Kümpfbeck and Christina Domnisoru, I have to thank for making this work possible at all, as they provided me with the data and the knowledge of all the experimental details. I warmly thank all my lab mates (Johannes Nagele, Michaela Pröll, Dora Csordas and Florian Eberhardt) for sharing their thoughts, feelings and ideas. I always found comfort and help in your company.

I am also grateful for the "social" team (Achilleas Koutsou, Michael Rebhan and Diana Amaro) with whom I had a great time trying to bring people from different labs together.

I would love to thank my family for supporting me throughout my whole life and my friends for making my life worth living.

And, at the end, I want to thank Stephan Sahm for being there for me.

References

Alessi, Camilla, Alessandra Raspanti, and Jacopo Magistretti (2016). „Two distinct types of depolarizing afterpotentials are differentially expressed in stellate and pyramidal-like neurons of entorhinal-cortex layer II". In: *Hippocampus* 26.3, pp. 380–404.

Alonso, Angel and Ruby Klink (1993). „Differential electroresponsiveness of stellate and pyramidal-like cells of medial entorhinal cortex layer II". In: *Journal of neurophysiology* 70.1, pp. 128–143.

Amaral, David G, Cynthia Dolorfo, and Pablo Alvarez-Royo (1991). „Organization of CA1 projections to the subiculum: a PHA-L analysis in the rat". In: *Hippocampus* 1.4, pp. 415–435.

Andersen, Per, TVP Bliss, and K Kr Skrede (1971). „Lamellar organization of hippocampal excitatory pathways". In: *Experimental Brain Research* 13.2, pp. 222–238.

Azouz, Rony, Morten S Jensen, and Yoel Yaari (1996). „Ionic basis of spike after-depolarization and burst generation in adult rat hippocampal CA1 pyramidal cells." In: *The Journal of physiology* 492.1, pp. 211–223.

Beckstead, Robert M (1978). „Afferent connections of the entorhinal area in the rat as demonstrated by retrograde cell-labeling with horseradish peroxidase". In: *Brain research* 152.2, pp. 249–264.

Best, Phillip J., Aaron M. White, and Ali. Minai (2001). „Spatial processing in the brain: the activity of hippocampal place cells." In: *Annual review of neuroscience* 24, pp. 459–86.

Bishop, Christopher (2006). *Pattern Recognition and Machine Learning*. Springer-Verlag New York.

Boccara, Charlotte N, Francesca Sargolini, Veslemøy Hult Thoresen, et al. (2010). „Grid cells in pre-and parasubiculum". In: *Nature neuroscience* 13.8, p. 987.

Brandon, Mark, Julie Koenig, and Stefan Leutgeb (2014). „Parallel and convergent processing in grid cell, head-direction cell, boundary cell, and place cell networks". In: 5, pp. 207–219.

Bruehl, Claus and Wytse J Wadman (1999). „Calcium currents in acutely isolated stellate and pyramidal neurons of rat entorhinal cortex". In: *Brain research* 816.2, pp. 554–562.

Brun, Vegard Heimly, Stefan Leutgeb, Hui-Qiu Wu, et al. (2008). „Impaired spatial representation in CA1 after lesion of direct input from entorhinal cortex". In: *Neuron* 57.2, pp. 290–302.

Buckley, Mark J, Michael CA Booth, Edmund T Rolls, and David Gaffan (2001). „Selective perceptual impairments after perirhinal cortex ablation". In: *Journal of Neuroscience* 21.24, pp. 9824–9836.

Burak, Yoram and Ila R Fiete (2009). „Accurate path integration in continuous attractor network models of grid cells". In: *PLoS computational biology* 5.2, e1000291.

Burwell, Rebecca D (2000). „The parahippocampal region: corticocortical connectivity". In: *Annals of the New York Academy of Sciences* 911.1, pp. 25–42.

Bussey, Timothy J, Lisa M Saksida, and Elisabeth A Murray (2002). „Perirhinal cortex resolves feature ambiguity in complex visual discriminations". In: *European Journal of Neuroscience* 15.2, pp. 365–374.

Canto, Cathrin B and Menno P Witter (2012). „Cellular properties of principal neurons in the rat entorhinal cortex. II. The medial entorhinal cortex". In: *Hippocampus* 22.6, pp. 1277–1299.

Canto, Cathrin B, Floris G Wouterlood, and Menno P Witter (2008). „What does the anatomical organization of the entorhinal cortex tell us?" In: *Neural plasticity* 2008.

Castelli, Loretta, Maximiliano J Nigro, and Jacopo Magistretti (2007). „Analysis of resurgent sodium-current expression in rat parahippocampal cortices and hippocampal formation". In: *Brain research* 1163, pp. 44–55.

Couey, Jonathan J, Aree Witoelar, Sheng-Jia Zhang, et al. (2013). „Recurrent inhibitory circuitry as a mechanism for grid formation". In: *Nature neuroscience* 16.3, p. 318.

D'Albis, Tiziano and Richard Kempter (2017). „A single-cell spiking model for the origin of grid-cell patterns". In: *PLoS computational biology* 13.10, e1005782.

Dayan, Peter and Laurence F Abbott (2001). *Theoretical neuroscience*. Vol. 806. Cambridge, MA: MIT Press.

Deshmukh, Sachin S and James J Knierim (2011). „Representation of non-spatial and spatial information in the lateral entorhinal cortex". In: *Frontiers in behavioral neuroscience* 5, p. 69.

Dhillon, A and Roland SG Jones (2000). „Laminar differences in recurrent excitatory transmission in the rat entorhinal cortex in vitro". In: *Neuroscience* 99.3, pp. 413–422.

Dickson, Clayton T, Jacopo Magistretti, Mark H Shalinsky, et al. (2000). „Properties and role of I h in the pacing of subthreshold oscillations in entorhinal cortex layer II neurons". In: *Journal of Neurophysiology* 83.5, pp. 2562–2579.

Domnisoru, Cristina, Amina A Kinkhabwala, and David W Tank (2013). „Membrane potential dynamics of grid cells". In: *Nature* 495.7440, p. 199.

Dorval, Alan D and John A White (2005). „Channel noise is essential for perithreshold oscillations in entorhinal stellate neurons". In: *Journal of neuroscience* 25.43, pp. 10025–10028.

Dudman, Joshua T and Matthew F Nolan (2009). „Stochastically gating ion channels enable patterned spike firing through activity-dependent modulation of spike probability". In: *PLoS computational biology* 5.2, e1000290.

Eacott, MJ, PE Machin, and EA Gaffan (2001). „Elemental and configural visual discrimination learning following lesions to perirhinal cortex in the rat". In: *Behavioural brain research* 124.1, pp. 55–70.

Ebbesen, Christian Laut, Eric Torsten Reifenstein, Qiusong Tang, et al. (2016). „Cell type-specific differences in spike timing and spike shape in the rat parasubiculum and superficial medial entorhinal cortex". In: *Cell reports* 16.4, pp. 1005–1015.

Eder, Claudia and Uwe Heinemann (1994). „Current density analysis of outward currents in acutely isolated rat entorhinal cortex cells". In: *Neuroscience letters* 174.1, pp. 58–60.

Eder, Claudia and Uwe Heinemann (1996). „Potassium currents in acutely isolated neurons from superficial and deep layers of the juvenile rat entorhinal cortex". In: *Pflügers Archiv-European Journal of Physiology* 432.4, pp. 637–643.

Engel, Tatiana A, Lutz Schimansky-Geier, Andreas VM Herz, Susanne Schreiber, and Irina A Erchova (2008). „Subthreshold membrane-potential resonances shape spike-train patterns in the entorhinal cortex". In: *Journal of neurophysiology*.

Erchova, Irina, G Kreck, U Heinemann, and AVM Herz (2004). „Dynamics of rat entorhinal cortex layer II and III cells: characteristics of membrane potential resonance at rest predict oscillation properties near threshold". In: *The Journal of physiology* 560.1, pp. 89–110.

Ferrante, Michele, Christopher F Shay, Yusuke Tsuno, G William Chapman, and Michael E Hasselmo (2016). „Post-inhibitory rebound spikes in rat medial entorhinal layer II/III principal cells: in vivo, in vitro, and computational modeling characterization". In: *Cerebral Cortex* 27.3, pp. 2111–2125.

Fransén, Erik, Angel A Alonso, Clayton T Dickson, Jacopo Magistretti, and Michael E Hasselmo (2004). „Ionic mechanisms in the generation of subthreshold oscillations and action potential clustering in entorhinal layer II stellate neurons". In: *Hippocampus* 14.3, pp. 368–384.

Fuchs, Elke C, Angela Neitz, Roberta Pinna, et al. (2016). „Local and distant input controlling excitation in layer II of the medial entorhinal cortex". In: *Neuron* 89.1, pp. 194–208.

Fuhs, Mark C and David S Touretzky (2006). „A spin glass model of path integration in rat medial entorhinal cortex". In: *Journal of Neuroscience* 26.16, pp. 4266–4276.

Fyhn, Marianne, Sturla Molden, Menno P Witter, Edvard I Moser, and May-Britt Moser (2004). „Spatial representation in the entorhinal cortex". In: *Science* 305.5688, pp. 1258–1264.

Gatome, CW, L Slomianka, HP Lipp, and I Amrein (2010). „Number estimates of neuronal phenotypes in layer II of the medial entorhinal cortex of rat and mouse". In: *Neuroscience* 170.1, pp. 156–165.

Gil, Mariana, Mihai Ancau, Magdalene I Schlesiger, et al. (2018). „Impaired path integration in mice with disrupted grid cell firing". In: *Nature neuroscience* 21.1, p. 81.

Groen, Thomas van and J Michael Wyss (1990). „The connections of presubiculum and parasubiculum in the rat". In: *Brain research* 518.1-2, pp. 227–243.

Haas, Julie S and John A White (2002). „Frequency selectivity of layer II stellate cells in the medial entorhinal cortex". In: *Journal of neurophysiology* 88.5, pp. 2422–2429.

Hafting, Torkel, Marianne Fyhn, Sturla Molden, May-Britt Moser, and Edvard I Moser (2005). „Microstructure of a spatial map in the entorhinal cortex". In: *Nature* 436.7052, p. 801.

Hargreaves, Eric L, Geeta Rao, Inah Lee, and James J Knierim (2005). „Major dissociation between medial and lateral entorhinal input to dorsal hippocampus". In: *science* 308.5729, pp. 1792–1794.

Hargus, Nicholas J, Ellen C Merrick, Aradhya Nigam, et al. (2011). „Temporal lobe epilepsy induces intrinsic alterations in Na channel gating in layer II medial entorhinal cortex neurons". In: *Neurobiology of disease* 41.2, pp. 361–376.

Hasselmo, Michael E (2014). „Neuronal rebound spiking, resonance frequency and theta cycle skipping may contribute to grid cell firing in medial entorhinal cortex". In: *Phil. Trans. R. Soc. B* 369.1635, p. 20120523.

Häusser, Michael, Nelson Spruston, and Greg J Stuart (2000). „Diversity and dynamics of dendritic signaling". In: *Science* 290.5492, pp. 739–744.

Heys, James G, Lisa M Giocomo, and Michael E Hasselmo (2010). „Cholinergic modulation of the resonance properties of stellate cells in layer II of medial entorhinal cortex". In: *Journal of neurophysiology* 104.1, pp. 258–270.

Hodgkin, Alan L and Andrew F Huxley (1952). „A quantitative description of membrane current and its application to conduction and excitation in nerve". In: *The Journal of physiology* 117.4, pp. 500–544.

Hönigsperger, Christoph, Maximiliano J Nigro, and Johan F Storm (2017). „Physiological roles of Kv2 channels in entorhinal cortex layer II stellate cells revealed by Guangxitoxin-1E". In: *The Journal of physiology* 595.3, pp. 739–757.

Hoydal, Oyvind Arne, Emilie Ranheim Skytoen, May-Britt Moser, and Edvard Ingjald Moser (2018). „Object-vector coding in the medial entorhinal cortex". In: *bioRxiv*, p. 286286.

Hutcheon, Bruce, Robert M Miura, and Ernest Puil (1996). „Models of subthreshold membrane resonance in neocortical neurons". In: *Journal of neurophysiology* 76.2, pp. 698–714.

Huys, Quentin JM, Misha B Ahrens, and Liam Paninski (2006). „Efficient estimation of detailed single-neuron models". In: *Journal of neurophysiology* 96.2, pp. 872–890.

Hyndman, Rob J (1996). „Computing and graphing highest density regions". In: *The American Statistician* 50.2, pp. 120–126.

Insausti, R, DG Amaral, and WM Cowan (1987). „The entorhinal cortex of the monkey: III. Subcortical afferents". In: *Journal of Comparative Neurology* 264.3, pp. 396–408.

Izhikevich, Eugene M (2007). *Dynamical systems in neuroscience*. MIT press.

Izhikevich, Eugene M, Niraj S Desai, Elisabeth C Walcott, and Frank C Hoppensteadt (2003). „Bursts as a unit of neural information: selective communication via resonance". In: *Trends in neurosciences* 26.3, pp. 161–167.

Jones, Roland SG (1994). „Synaptic and intrinsic properties of neurons of origin of the perforant path in layer II of the rat entorhinal cortex in vitro". In: *Hippocampus* 4.3, pp. 335–353.

Justus, Daniel, Dennis Dalügge, Stefanie Bothe, et al. (2017). „Glutamatergic synaptic integration of locomotion speed via septoentorhinal projections". In: *Nature neuroscience* 20.1, p. 16.

Kitamura, Takashi, Michele Pignatelli, Junghyup Suh, et al. (2014). „Island cells control temporal association memory". In: *Science* 343.6173, pp. 896–901.

Klink, Ruby and Angel Alonso (1997). „Morphological characteristics of layer II projection neurons in the rat medial entorhinal cortex". In: *Hippocampus* 7.5, pp. 571–583.

Knierim, James J, Joshua P Neunuebel, and Sachin S Deshmukh (2014). „Functional correlates of the lateral and medial entorhinal cortex: objects, path integration and local–global reference frames". In: *Philosophical Transactions of the Royal Society B: Biological Sciences* 369.1635, p. 20130369.

Knight, William R (1966). „A computer method for calculating Kendall's tau with ungrouped data". In: *Journal of the American Statistical Association* 61.314, pp. 436–439.

Kosel, Keith C, Gary W Van Hoesen, and James R West (1981). „Olfactory bulb projections to the parahippocampal area of the rat". In: *Journal of Comparative Neurology* 198.3, pp. 467–482.

Kraus, Benjamin J, Mark P Brandon, Robert J Robinson, et al. (2015). „During running in place, grid cells integrate elapsed time and distance run". In: *Neuron* 88.3, pp. 578–589.

Kraus, Benjamin J, Robert J Robinson II, John A White, Howard Eichenbaum, and Michael E Hasselmo (2013). „Hippocampal "time cells": time versus path integration". In: *Neuron* 78.6, pp. 1090–1101.

Krettek, JE and JL Price (1977). „Projections from the amygdaloid complex and adjacent olfactory structures to the entorhinal cortex and to the subiculum in the rat and cat". In: *Journal of Comparative Neurology* 172.4, pp. 723–752.

Kropff, Emilio, James E Carmichael, May-Britt Moser, and Edvard I Moser (2015). „Speed cells in the medial entorhinal cortex". In: *Nature* 523.7561, p. 419.

Kropff, Emilio and Alessandro Treves (2008). „The emergence of grid cells: Intelligent design or just adaptation?" In: *Hippocampus* 18.12, pp. 1256–1269.

Kümpfbeck, Franziska (2019). „Physiological basis and function of depolarizing afterpotentials in the entorhinal cortex". (Unpublished doctoral dissertation). Ludwig-Maximilians-Universität München, München, Germany.

Latuske, Patrick, Oana Toader, and Kevin Allen (2015). „Interspike intervals reveal functionally distinct cell populations in the medial entorhinal cortex". In: *Journal of Neuroscience* 35.31, pp. 10963–10976.

Lever, Colin, Stephen Burton, Ali Jeewajee, John O'Keefe, and Neil Burgess (2009). „Boundary vector cells in the subiculum of the hippocampal formation". In: *Journal of Neuroscience* 29.31, pp. 9771–9777.

Lewis, Amanda H and Indira M Raman (2014). „Resurgent current of voltage-gated Na+ channels". In: *The Journal of physiology* 592.22, pp. 4825–4838.

Lisman, John E (1997). „Bursts as a unit of neural information: making unreliable synapses reliable". In: *Trends in neurosciences* 20.1, pp. 38–43.

Ma, Minghong and John Koester (1996). „The role of K+ currents in frequency-dependent spike broadening in Aplysia R20 neurons: a dynamic-clamp analysis". In: *Journal of Neuroscience* 16.13, pp. 4089–4101.

MacDonald, Christopher J, Kyle Q Lepage, Uri T Eden, and Howard Eichenbaum (2011). „Hippocampal "time cells" bridge the gap in memory for discontiguous events". In: *Neuron* 71.4, pp. 737–749.

MacQueen, James et al. (1967). „Some methods for classification and analysis of multivariate observations". In: *Proceedings of the fifth Berkeley symposium on mathematical statistics and probability*. Vol. 1. 14. Oakland, CA, USA, pp. 281–297.

Magistretti, Jacopo and Angel Alonso (1999). „Biophysical properties and slow voltage-dependent inactivation of a sustained sodium current in entorhinal cortex layer-II principal neurons: a whole-cell and single-channel study". In: *The Journal of general physiology* 114.4, pp. 491–509.

Magistretti, Jacopo, David S Ragsdale, and Angel Alonso (1999). „High conductance sustained single-channel activity responsible for the low-threshold persistent Na+ current in entorhinal cortex neurons". In: *Journal of Neuroscience* 19.17, pp. 7334–7341.

Margrie, Troy W, Michael Brecht, and Bert Sakmann (2002). „In vivo, low-resistance, whole-cell recordings from neurons in the anaesthetized and awake mammalian brain". In: *Pflügers Archiv* 444.4, pp. 491–498.

McNaughton, Bruce L, Francesco P Battaglia, Ole Jensen, Edvard I Moser, and May-Britt Moser (2006). „Path integration and the neural basis of the 'cognitive map'". In: *Nature Reviews Neuroscience* 7.8, p. 663.

Mishra, Rajiv K, Sooyun Kim, Segundo J Guzman, and Peter Jonas (2016). „Symmetric spike timing-dependent plasticity at CA3–CA3 synapses optimizes storage and recall in autoassociative networks". In: *Nature communications* 7, p. 11552.

Monsalve-Mercado, Mauro M and Christian Leibold (2017). „Hippocampal spike-timing correlations lead to hexagonal grid fields". In: *Physical review letters* 119.3, p. 038101.

Moser, Edvard I, Emilio Kropff, and May-Britt Moser (2008). „Place cells, grid cells, and the brain's spatial representation system". In: *Annual review of neuroscience* 31.

Moser, Edvard I and May-Britt Moser (2008). „A metric for space". In: *Hippocampus* 18.12, pp. 1142–1156.

Müller, Martin and Rüdiger Wehner (1988). „Path integration in desert ants, Cataglyphis fortis". In: *Proceedings of the National Academy of Sciences* 85.14, pp. 5287–5290.

Murray, Elisabeth A, Mark G Baxter, and David Gaffan (1998). „Monkeys with rhinal cortex damage or neurotoxic hippocampal lesions are impaired on spatial scene learning and object reversals." In: *Behavioral neuroscience* 112.6, p. 1291.

Murray, Elisabeth A, TJ Bussey, RR Hampton, and LM Saksida (2000). „The parahippocampal region and object identification". In: *Annals of the New York Academy of Sciences* 911.1, pp. 166–174.

Murray, Elisabeth A and Mortimer Mishkin (1998). „Object recognition and location memory in monkeys with excitotoxic lesions of the amygdala and hippocampus". In: *Journal of Neuroscience* 18.16, pp. 6568–6582.

Navratilova, Zaneta, Lisa M Giocomo, Jean-Marc Fellous, Michael E Hasselmo, and Bruce L McNaughton (2012). „Phase precession and variable spatial scaling in a periodic attractor map model of medial entorhinal grid cells with realistic after-spike dynamics". In: *Hippocampus* 22.4, pp. 772–789.

Nigro, Maximiliano Josè, Giulia Quattrocolo, and Jacopo Magistretti (2012). „Distinct developmental patterns in the expression of transient, persistent, and resurgent Na+ currents in entorhinal cortex layer-II neurons". In: *Brain research* 1463, pp. 30–41.

Nocedal, Jorge and Stephen Wright (2006). *Numerical optimization*. Springer Science & Business Media, pp. 135–163.

Nolan, Matthew F, Joshua T Dudman, Paul D Dodson, and Bina Santoro (2007). „HCN1 channels control resting and active integrative properties of stellate cells from layer II of the entorhinal cortex". In: *Journal of Neuroscience* 27.46, pp. 12440–12451.

Norman, G and MJ Eacott (2005). „Dissociable effects of lesions to the perirhinal cortex and the postrhinal cortex on memory for context and objects in rats." In: *Behavioral neuroscience* 119.2, p. 557.

O'Keefe, John (1976). „Place units in the hippocampus of the freely moving rat". In: *Experimental neurology* 51.1, pp. 78–109.

O'Keefe, John and Jonathan Dostrovsky (1971). „The hippocampus as a spatial map: Preliminary evidence from unit activity in the freely-moving rat." In: *Brain research* 34, pp. 171–175.

Ólafsdóttir, H Freyja, Daniel Bush, and Caswell Barry (2018). „The Role of Hippocampal Replay in Memory and Planning". In: *Current Biology* 28.1, R37–R50.

Parron, Carole and Etienne Save (2004). „Evidence for entorhinal and parietal cortices involvement in path integration in the rat". In: *Experimental Brain Research* 159.3, pp. 349–359.

Pastoll, Hugh, Lukas Solanka, Mark CW van Rossum, and Matthew F Nolan (2013). „Feedback inhibition enables theta-nested gamma oscillations and grid firing fields". In: *Neuron* 77.1, pp. 141–154.

Pearson, Karl (1901). „LIII. On lines and planes of closest fit to systems of points in space". In: *The London, Edinburgh, and Dublin Philosophical Magazine and Journal of Science* 2.11, pp. 559–572.

Pike, Fenella G, Rhiannon M Meredith, Andrew WA Olding, and Ole Paulsen (1999). „Postsynaptic bursting is essential for 'Hebbian' induction of associative long-term potentiation at excitatory synapses in rat hippocampus". In: *The Journal of physiology* 518.2, pp. 571–576.

Raman, Indira M and Bruce P Bean (1997). „Resurgent sodium current and action potential formation in dissociated cerebellar Purkinje neurons". In: *Journal of Neuroscience* 17.12, pp. 4517–4526.

Ramon y Cajal, Santiago (1902). „Sobre un ganglio especial de la corteza esfeno-occipital". In: *Trabajos del Laboratorio de Investigaciones Biologicas de la Universidad de Madrid* 1, pp. 189–206.

Ramon y Cajal, Santiago (1909). *Histologie du Systeme Nerveux de l'Homme et des Vertebres*. Paris: Maloine.

Ray, Saikat, Robert Naumann, Andrea Burgalossi, et al. (2014). „Grid-layout and theta-modulation of layer 2 pyramidal neurons in medial entorhinal cortex". In: *Science* 343.6173, pp. 891–896.

Rotstein, Horacio G, Tim Oppermann, John A White, and Nancy Kopell (2006). „The dynamic structure underlying subthreshold oscillatory activity and the onset of spikes in a model of medial entorhinal cortex stellate cells". In: *Journal of computational neuroscience* 21.3, pp. 271–292.

Sargolini, Francesca, Marianne Fyhn, Torkel Hafting, et al. (2006). „Conjunctive representation of position, direction, and velocity in entorhinal cortex". In: *Science* 312.5774, pp. 758–762.

Schmidt-Hieber, Christoph and Michael Häusser (2013). „Cellular mechanisms of spatial navigation in the medial entorhinal cortex". In: *Nature neuroscience* 16.3, p. 325.

Schmidt-Hieber, Christoph, Gabija Toleikyte, Laurence Aitchison, et al. (2017). „Active dendritic integration as a mechanism for robust and precise grid cell firing". In: *Nature neuroscience* 20.8, p. 1114.

Scott, David W (2015). *Multivariate density estimation: theory, practice, and visualization*. John Wiley & Sons.

Skaggs, William E and Bruce L McNaughton (1996). „Replay of neuronal firing sequences in rat hippocampus during sleep following spatial experience". In: *Science* 271.5257, pp. 1870–1873.

Skaggs, William E, Bruce L McNaughton, Michele Permenter, et al. (2007). „EEG sharp waves and sparse ensemble unit activity in the macaque hippocampus". In: *Journal of neurophysiology* 98.2, pp. 898–910.

Solstad, Trygve, Charlotte N Boccara, Emilio Kropff, May-Britt Moser, and Edvard I Moser (2008). „Representation of geometric borders in the entorhinal cortex". In: *Science* 322.5909, pp. 1865–1868.

Staba, Richard J, Charles L Wilson, Itzhak Fried, and Jerome Engel Jr (2002). „Single neuron burst firing in the human hippocampus during sleep". In: *Hippocampus* 12.6, pp. 724–734.

Steward, Oswald and Sheila A Scoville (1976). „Cells of origin of entorhinal cortical afferents to the hippocampus and fascia dentata of the rat". In: *Journal of Comparative Neurology* 169.3, pp. 347–370.

Stuart, Greg J and Michael Häusser (2001). „Dendritic coincidence detection of EPSPs and action potentials". In: *Nature neuroscience* 4.1, p. 63.

Suzuki, Wendy A and David G Amaral (1994). „Topographic organization of the reciprocal connections between the monkey entorhinal cortex and the perirhinal and parahippocampal cortices". In: *Journal of Neuroscience* 14.3, pp. 1856–1877.

Swanson, LW and C Kohler (1986). „Anatomical evidence for direct projections from the entorhinal area to the entire cortical mantle in the rat". In: *Journal of Neuroscience* 6.10, pp. 3010–3023.

Tamamaki, Nobuaki and Yoshiaki Nojyo (1995). „Preservation of topography in the connections between the subiculum, field CA1, and the entorhinal cortex in rats". In: *Journal of Comparative Neurology* 353.3, pp. 379–390.

Tang, Qiusong, Andrea Burgalossi, Christian Laut Ebbesen, et al. (2014). „Pyramidal and stellate cell specificity of grid and border representations in layer 2 of medial entorhinal cortex". In: *Neuron* 84.6, pp. 1191–1197.

Taube, Jeffrey S (1998). „Head direction cells and the neurophysiological basis for a sense of direction". In: *Progress in neurobiology* 55.3, pp. 225–256.

Taube, Jeffrey S, Robert U Muller, and James B Ranck (1990). „Head-direction cells recorded from the postsubiculum in freely moving rats. I. Description and quantitative analysis". In: *Journal of Neuroscience* 10.2, pp. 420–435.

Tsao, Albert, May-Britt Moser, and Edvard I Moser (2013). „Traces of experience in the lateral entorhinal cortex". In: *Current Biology* 23.5, pp. 399–405.

Tsao, Albert, Jørgen Sugar, Li Lu, et al. (2018). „Integrating time from experience in the lateral entorhinal cortex". In: *Nature* 561.7721, p. 57.

Turner, Ray W, Neal Lemon, Brent Doiron, et al. (2002). „Oscillatory burst discharge generated through conditional backpropagation of dendritic spikes". In: *Journal of Physiology-Paris* 96.5-6, pp. 517–530.

Ungerleider, Leslie G and James V Haxby (1994). „'What'and 'where'in the human brain". In: *Current opinion in neurobiology* 4.2, pp. 157–165.

Van Strien, Niels M, NLM Cappaert, and Menno P Witter (2009). „The anatomy of memory: an interactive overview of the parahippocampal–hippocampal network". In: *Nature Reviews Neuroscience* 10.4, p. 272.

Vavoulis, Dimitrios V, Volko A Straub, John AD Aston, and Jianfeng Feng (2012). „A self-organizing state-space-model approach for parameter estimation in Hodgkin-Huxley-type models of single neurons". In: *PLoS computational biology* 8.3, e1002401.

Wang, Yao, Yu-zhang Liu, Shi-yi Wang, and Zhiru Wang (2016). „In vivo whole-cell recording with high success rate in anaesthetized and awake mammalian brains". In: *Molecular brain* 9.1, p. 86.

Wilson, Matthew A and Bruce L McNaughton (1994). „Reactivation of hippocampal ensemble memories during sleep". In: *Science* 265.5172, pp. 676–679.

Winterer, Jochen, Nikolaus Maier, Christian Wozny, et al. (2017). „Excitatory microcircuits within superficial layers of the medial entorhinal cortex". In: *Cell reports* 19.6, pp. 1110–1116.

Winters, Boyer D, Lisa M Saksida, and Timothy J Bussey (2006). „Paradoxical facilitation of object recognition memory after infusion of scopolamine into perirhinal cortex: implications for cholinergic system function". In: *Journal of Neuroscience* 26.37, pp. 9520–9529.

Witter, Menno P, Floris G Wouterlood, Pieterke A Naber, and Theo Van Haeften (2000). „Anatomical organization of the parahippocampal-hippocampal network". In: *Annals of the New York Academy of Sciences* 911.1, pp. 1–24.

Yeckel, Mark F and Theodore W Berger (1990). „Feedforward excitation of the hippocampus by afferents from the entorhinal cortex: redefinition of the role of the trisynaptic pathway." In: *Proceedings of the National Academy of Sciences* 87.15, pp. 5832–5836.

Yoshida, Motoharu and Angel Alonso (2007). „Cell-type–specific modulation of intrinsic firing properties and subthreshold membrane oscillations by the M (Kv7)-current in neurons of the entorhinal cortex". In: *Journal of neurophysiology* 98.5, pp. 2779–2794.

Yue, Cuiyong, Stefan Remy, Hailing Su, Heinz Beck, and Yoel Yaari (2005). „Proximal persistent Na+ channels drive spike afterdepolarizations and associated bursting in adult CA1 pyramidal cells". In: *Journal of Neuroscience* 25.42, pp. 9704–9720.

Zhang, L, TA Valiante, and PL Carlen (1993). „Contribution of the low-threshold T-type calcium current in generating the post-spike depolarizing afterpotential in dentate granule neurons of immature rats". In: *Journal of neurophysiology* 70.1, pp. 223–231.